Microstructure Analysis and Surface Planarization of Excimer-laser Annealed Si Thin Films

Miao Yu

Submitted in partial fulfillment of the
requirements for the degree of
Doctor of Philosophy
under the Executive Committee
of the Graduate School of Arts and Sciences

COLUMBIA UNIVERSITY

2020

© 2020
Miao Yu
All Rights Reserved

Abstract

Microstructure Analysis and Surface Planarization of Excimer-laser Annealed Si Thin Films

Miao Yu

The excimer-laser annealed (ELA) polycrystalline silicon (p-Si or polysilicon) thin film, which influences more than 100-billion-dollar display market, is *the* backplane material of the modern advanced LCD and OLED products. The microstructure (i.e. ELA microstructure) and surface morphology of an ELA p-Si thin film are the two main factors determining the material properties, and they significantly affect the performance of the subsequently fabricated thin film transistors (TFTs). The microstructure is the result of a rather complex crystallization process during the ELA which is characterized as far-from-equilibrium, multiple-pulse-per-area and processing-parameter dependent. Studies of the ELA microstructure and the surface morphology closely related to the device performance as well as the microstructure evolution during the ELA process are long-termly demanded by both the scientific research and the industrial applications, but unfortunately have not been thoroughly performed in the past.

The main device-performance-related characteristics of the ELA microstructure are generally considered to be the grain size and the presence of the dense grain boundaries. In the work of this thesis, an image-processing-based program (referred to as the GB extraction program) is developed to

extract the grain boundary map (GB map) out of the transmission electron microscope (TEM) images of the ELA microstructure. The grain sizes are straightforwardly calculated from the GB map and statistically analyzed. More importantly, based on the GB maps, we propose and perform a rigorous scheme that we call the local-microstructure analysis (LMA) to quantitatively and systematically analyze the spatial distribution of the grain boundaries. The "local area" is mainly defined by the geometry and the location of a TFT. The successful extraction of the GB map and the subsequent LMA are permitted by our unique TEM skills to produce high-resolution TEM micrographs containing statistically significant number of grains for sensible quantitative analysis. The LMA unprecedentedly enables quantitative and rigorous analysis of spatial characteristics of the microstructure, especially the device geometry- and location-related characteristics. Additionally, we present and highlight the benefits of the LMA approach over the traditional statistical grain-size analysis of the ELA microstructure.

From the grain-size analysis, we find that grain size across a statistically significant number of grains generally follows the same distribution as in the stochastic grain growth scenario at the beginning of the ELA process when the laser pulse (i.e. shot) number is small. As the shot number increases, the overall grain size monotonically increases while the distribution profile becomes broader. When the scan number reaches the ELA threshold (several tens of laser shots), the distribution profile substantially deviates from the stochastic profile and shows two sharp peaks in grain size around 300nm and 450nm, which is consistent with the previously proposed theory of energy coupling and nonuniform energy deposition during ELA. From the LMA, local nonuniformity of grain boundary density (GB density) at the device length scales and regions of high grain boundary periodicity are identified.

More importantly, we find that the local nonuniformity is much more pronounced when p-Si film exhibits some level of spatial ordering, but less pronounced for a random grain arrangement. It is worth noting that the devices of different sizes and orientation have different sensitivity to the local nonuniformity of the ELA-generated p-Si thin film. In addition, based on the analysis results, the connection between the microstructure evolution and the partial melting and resolidification process of the Si film is discussed.

Aside from the microstructure, the surface morphology of the ELA films, featuring pronounced surface protrusions, is characterized via an atomic force microscope (AFM). Attempts to planarize those surface protrusions detrimental to the subsequent device performance are conducted. In the attempts, the as-is (oxide-capped) ELA films and the BHF-treated ELA films are subjected to single shots of excimer irradiation. When the results are compared, an anisotropic melting phenomenon of the p-Si grains is identified, which appears to be strongly affected by the presence of the surface oxide capping layer. Conceptual models are developed and numerical simulations are employed to explain the observation of the anisotropic melting phenomenon and the effect of the surface oxide layer. Eventually, 41.8% reduction of root mean square (RMS) surface roughness is achieved for BHF-treated ELA films.

The results gained in the systematic analysis of the ELA microstructure and the attempt of surface planarization further our understanding about (1) the device performance-related material microstructure of the ELA p-Si thin films, (2) the microstructure evolution occurring during multiple shots of the ELA process, and (3) the fundamental phase transformations in the far-from-equilibrium melt-mediated excimer-laser annealing processing of p-Si thin films. Such understanding could help engineers when designing the

microelectronic devices and the ELA manufacturing process, as well as provide scientific researchers with insights on the melting and solidification of general polycrystalline materials, thus profoundly contributing to both the related scientific society and the technological community. The GB extraction program and the LMA scheme developed and demonstrated in the thesis, as another contribution to the related research filed, could also be generalized to the microstructural study of other polycrystalline materials where grain geometry and arrangement are of concern.

Table of Contents

List of Figures v

List of Tables xiv

Acknowledgments xv

Chapter 1 Introduction 1

1.1 Excimer-Laser Crystallization 2

1.2 Excimer-Laser Annealing Technique 3

1.3 Approaches for the Work 6

1.4 Organization of the Dissertation 8

Chapter 2 Background and Motivation 11

2.1 Fundamental Framework of Laser Crystallization 12

2.1.1 Thermodynamics of Melting and Solidification 13

2.1.2 Kinetics of melting and solidification 14

2.1.3 The Gibbs-Thomson Effect 15

2.2 Related Background Knowledge of ELC Si Thin Films 16

2.2.1 Laser-material Interaction of Si 17

2.2.2 Different Melting Regimes 21

2.2.3 Crystallization of a-Si Thin Films in Partial-melting Regime 24

2.2.4 In-situ probing of Transient Reflectance and Transmittance During Laser-induced Phase Transformation of Si Thin Film 25

2.3 Related Background Knowledge of the ELA Technique 27

2.3.1 Overview of the ELA Technique 28

2.3.2 The ELA Technique in Modern Electronic Display 30

2.3.3 The Microstructure and Surface Morphology of ELA Si Thin Films 32

2.3.4 The Influences of Grain Boundaries and Surface Protrusions on the Device Performance 36
2.4 The Microstructure Nonuniformity and the Local Microstructure Analysis 38
2.5 Motivation and Research Strategy 41
Chapter 3 An Image-processing-based Method for the Grain Boundary Extraction 44
3.1 Necessity and Difficulties in the GB Extraction 45
3.2 The Implementation of the Watershed Segmentation in the GB Extraction 47
3.2.1 The Idea of the Watershed Segmentation 48
3.2.2 Theoretical Framework and Definitions 51
3.2.3 The Algorithm 54
3.2.4 The Pseudocode 57
3.3 The Results 61
3.4 Summary 64
Chapter 4 The Local Microstructure Analysis (LMA) 66
4.1 Grain Size Statistics 67
4.2 Spatial Analysis of the Microstructure 68
4.2.1 The LMA-GB Density Analysis 69
4.2.2 The LMA-Orientation Analysis 73
4.2.3 Periodicity Detection 75
4.3 Discussion 77
4.4 Summary 79
Chapter 5 The ELA Experiments and Comprehensive Microstructure Analysis 80
5.1 ELA Experiments 81

5.1.1 Experimental Plan 81
5.1.2 Sample Configuration of the precursor a-Si 82
5.1.3 Experiment Setup 82
5.2 Grain Imaging by Transmission Electron Microscope 83
5.3 Systematic Microstructure Analysis and Comparison 87
5.3.1 Grain Size Statistics 88
5.3.2 The LMA-GB Density Analysis 90
5.3.3 The LMA-Orientation Analysis 94
5.3.4 Periodicity Analysis 96
5.4 Discussion 99
5.5 Summary 103
Chapter 6 Surface Planarization of As-is ELA Si Thin Films 104
6.1 Characterization of Surface Morphology 105
6.2 The Previous Study of Surface Planarization 106
6.3 Planarization Experiments 107
6.3.1 Experimental Details 107
6.3.2 Results and Analysis 109
6.3.3 Transient Reflectance and Transmittance Analysis 112
6.4 Discussion 115
6.4.1 The Melting and Solidification Scenario 116
6.4.2 The Numerical Simulation 118
6.5 Summary 123
Chapter 7 Surface Planarization of BHF-treated ELA Si Thin Films 124
7.1 Planarization Experiments 125
7.1.1 Results and Analysis 125
7.1.2 Transient Reflectance and Transmittance Analysis 127

7.2 Discussion 129
7.3 Summary 132
Chapter 8 Conclusions 133
8.1 Conclusion 133
8.2 Suggestions for the Future Work 136
Bibliography 138
Appendix A Spot Beam Crystallization Generated Si Thin Films . 149
A.1 Spot-Beam Crystallization Method 151
A.2 Microstructure of the SBC Si Thin Film 152
A.3 Discussion and Summary 153

List of Figures

Fig 2.1: The isobaric Gibbs free energies versus temperature respectively of crystalline (c-Si), amorphous (a-Si) and liquid (l-Si) phase of Si. Tmc and Tma are the equilibrium melting temperatures respectively of c-Si and a-Si.. 13

Fig 2.2: Interface velocity versus temperature respectively of c-Si (Vc(T)) and a-Si (Va(T)). Tmc and Tma denote the equilibrium melting temperature of c-Si and that of a-Si.. 15

Fig 2.3: Reflectivity and absorption coefficient of c-Si at room temperature, which are wavelength dependent. It can be seen that Si is very absorptive for UV light (the range of the excimer laser) and becomes much less absorptive for the light with larger wavelength. 18

Fig 2.4: Time-resolved reflectance change of the probing laser during melting and solidification of Si upon laser irradiation, where Ra, Rl and Rc respectively denote the reflectance of amorphous, liquid and crystalline Si.. 19

Fig 2.5: A schematic illustrating light and material interaction of planar Si surface. When light is incident upon the planar surface of Si, part of the energy is reflected and part of the energy is absorbed....................... 20

Fig 2.6: Schematics of (a) partial melting, (b) near-complete melting, and (c) complete melting regimes. In the partial melting regime, a continuous layer of unmelted solid sustains, while, in complete melting regime, the entire film transforms into liquid phase during laser irradiation.. 22

Fig 2.7: Plane-view bright-field TEM images of the microstructure of the laser crystallized precursor a-Si thin films in partial-melting regime ((a), (b), (c), (f), (g) and (h)), near-complete-melting regime ((d) and (i)) and complete-melting regime ((e) and (j)) [42]. 23
Fig 2.8: Schematic diagram illustrating the explosive crystallization phenomenon of a precursor a-Si thin film during the first laser shot in the ELA process, representing the fundamental phase transformation mechanism involved in the partial melting regime of a-Si films upon excimer laser irradiation... 25
Fig 2.9: (a) Schematic diagram of the melting and solidification process of a Si film, where the front surface of the film first transforms into a continuous liquid layer and the melting or solidification proceeds respectively as the downward extension or the upward shrinkage of the thickness of the liquid layer.. 26
Fig 2.10: (a) The planar-view bright-field TEM image of the microstructure of an ELA-generated p-Si thin film, and (b) diagrams of the average grain size versus excimer-laser energy under different gas-ingredient conditions and (c) the average grain size versus per-area laser-shot numbers under different experimental conditions [57]..................... 30
Fig 2.11: (a) A picture of the state-of-art excimer-laser system used in the current ELA manufacturing, developed by Coherent, Inc., and (b) a schematic diagram illustrating the laser-scan process in the ELA.. .. 32
Fig 2.12: (a) The plane-view bright-field TEM image of the ELA grains, (b) an AFM image of the ELA grains and (c) an AFM image of the boundary-etched p-Si thin film, which was done and reported by other researchers [21]. 33
Fig 2.13: (a1) and (a2) the plane-view bright-field TEM image and AFM

image of p-Si after a small number of laser shots, (b1) and (b2) the plane-view bright-field TEM image and an AFM image of p-Si after a medium number of laser shots, and (c1) and (c2) the plane-view bright-field TEM image and AFM image of p-Si after a large number of laser shots.. 35

Fig 2.14: (a) A schematic diagram showing the structural configuration of an OLED display panel, where the TFT backplane is fabricated by the ELA process, and (b) a schematic diagram illustrating a typical TFT fabricated on an ELA-generated p-Si thin film................................. 37

Fig 2.15: The plane-view bright-field TEM image of an ELA-generated p-Si thin film. The grains generally seem to be regular, while the grains in the circled regions look irregular. 39

Fig 2.16: (a)-(b) Schematic drawing of three situations of artificial grain distribution, where the average grain size of the three situations is the same and the grains in (b) and (c) are exactly identical but with different arrangements. Each square (or rectangle) represents a grain............. 40

Fig 3.1: Plane-view bright-field TEM image ($33\mu m \times 23\mu m$) of the ELA microstructure. Around 9,000 grains are captured in the image, which is a statistically meaningful number for the quantitative analysis of the microstructure.. 46

Fig 3.2: A brief illustration of how a computer displays a greyscale image. Figure (a) is an image in greyscale which displays the matrix (b) with values ranging from 0 to 255.. 48

Fig 3.3: (a) - (c) Schematic diagrams illustrating the conceptual description of the immersion process in the Watershed Segmentation. In the immersion process, water level, elevates monotonically from the lowest altitude (i.e. pixels with the smallest value) to the highest

altitude (i.e. pixels with the largest value). 49

Fig 3.4: Schematic diagram illustrating the three classes that all the pixels need to be sorted into in the immersion process in order to let a computer identify basins and watersheds. 50

Fig 3.5: (a) Schematic diagram illustrating the geodesic distance between two pixels (pi and pj) and the geodesic distance between a pixel (pi) and a subset (Pj) of pixels with in a pixel set P, and (b) schematic diagram illustrating the influence zone (hatched area) of a pixel subset Pi and the skeleton by influence zones (SKIZ) between Pi and Pj as well as between Pj and Pk. 52

Fig 3.6: An example of computing the above recursion (the immersion process), where the numbers are the initial pixel values. 54

Fig 3.7: (a) A cropped plane-view bright-field TEM image of an ELA-generated p-Si thin film, which is the input of our grain boundary segmentation program (GB segmentation program), (b) the beginning of the program when one local minimum at the lowest altitude of the entire image is identified. 62

Fig 3.8: (a) A plane-view bright-field TEM image of the microstructure of the ELA-generated p-Si thin film; (b) the GB map converted from the TEM image (a); (c) the overlapped image of the TEM image (a) and the GB map (b) which verifies the accuracy of our GB segmentation program. 64

Fig 4.1: (a) The plane-view bright-field TEM image of the ELA microstructure, (b) the binary GB map generated from the TEM image (a) using our program, and (c) the statistical grain-size distribution and the normal distribution fitted curve. 68

Fig 4.2: (a) The TEM image of the microstructure of an ELA-generated p-Si, (b) the overlapped image of the GB map and the original TEM image, and (c) the overlapped image of the TEM image, the GB map and the GB density heat map, where hot (reddish) regions indicate higher GB density while the cold (bluish) regions indicate lower defect density. 71
Fig 4.3: (a)-(c) GB density heat maps respectively corresponding to 0.5µm, 1µm and 2µm probing circles, where reddish color means high GB density (consisting of relatively smaller grains) while blueish color means low GB density (consisting of relatively larger grains), and (d) the curve-fitted statistic diagrams of the α values under the three situations, where the blue, orange and yellow curves respectively correspond to 0.5µm, 1µm and 2µm diameter situations. 73
Fig 4.4: (a1)-(c1) The GB density heat maps when the major axes of the testing oval are respectively at the angle of 30°, 75° and 135° with respect to the horizon, and (a2)-(c2) the corresponding statistical histograms of the α values respectively corresponding to (a1)-(c1).. 75
Fig 4.5: (a) The binary GB map generated from the TEM image of the ELA-generated p-Si thin film, (b) the FFT diffraction pattern obtained from the GB map, (c) the filtered FFT image after diminishing the background signal and noise, and (d) the inversed FFT image transformed from (c).. 77
Fig 4.6: A flash photograph of the surface of an ELA-generated panel under oblique angle. The different colors at different angles of view evidence the existence of light diffraction [21]... 78

Fig 5.1: (a) Laser system setup for the ELA experiments and (b) the optical layout schematic of the beam delivery system. 83
Fig 5.2: (a) A photo of JEOL 100CX TEM system used in the microstructure characterization, (b) the electron microscopy film after exposure and development, which captures the microstructure of the p-Si thin film, and (c) the lifted ELA-generated p-Si thin film on a copper TEM grid. 85
Fig 5.3: (a)-(d) The TEM images of the microstructure of the multiple-shot irradiated Si thin films respectively with 5, 10, 15, 20, 25 and 30 shots of laser irradiation. (a) is under 7500x magnification and the rest are under 5000x magnification. 87
Fig 5.4: The GB maps (red) overlapped with their source TEM images resulting from 5 shots (a), 10 shots (b), 15 shots (c), 20 shots (d), 25 shots (e) and 30 shots (f) of laser irradiation. It can be seen that the GB extraction is very precise. 88
Fig 5.5: (a)-(f) The statistical grain-size distributions of the multiple-shot irradiated p-Si thin films respectively under 5-, 10-, 15-, 20-, 25- and 30-shot conditions. The insets in the top right corner show the average and standard deviation. 90
Fig 5.6: (a)-(f) The heat maps of the relative defect density distribution of multiple-shot-irradiated p-Si under 5-, 10-, 15-, 20-, 25- and 30-shot conditions with respect to 0.5μm TFT size, where the ‘hot’ area represents high relative defect density regions, while the ‘cold” area represents low relative defect density regions. 92
Fig 5.7: (a)-(f) The heat maps of the relative defect density distribution of multiple-shot irradiated p-Si under 5-, 10-, 15-, 20-, 25- and 30-shot conditions with respect to 2μm TFT size, where the ‘hot’ area

represents high relative defect density regions, while the 'cold" area represents low relative defect density regions............................... 93
Fig 5.8: (a1) (a2)-(c1)(c2) Figure pairs of the heat maps and statistical histograms of the spatial distribution of the relative defect density, respectively corresponding to 0°, 90° and 165°TFT orientations for the 5-shot condition, and (d1)(d2)-(f1)(f2) same figure pairs respectively corresponding to 30°, 75° and 135° orientations for the 30-shot condition. 96
Fig 5.9: (a1) (a2) (a3) - (f1) (f2) (f3) Figure sets of the overlapped image of TEM image and the GB map, FFTs of the GB map with filtered background signals and noises, and the IFFTs of the filtered FFT image, which highlight the periodic area respectively for the 5-, 10-, 15-, 20-, 25- and 30-shot conditions of laser irradiation.. 98
Fig 5.10: (a) and (b) The fitted curves of the statistical histograms of the α values respectively corresponding to 0.5μm TFT size and 2μm TFT size for the six laser-shot conditions, (c) The comparison of (a) (dashed lines) and (b) (solid lines) in the same plot.................... 101
Fig 6.1: (a) the AFM image of an as-is ELA-generated p-Si thin film, (b) the roughness analysis at one cross-section of (a), and (c) one previously reported high-resolution AFM image of the surface morphology where the grain junctions are selectively etched by a Secco etchant [21]... 106
Fig 6.2: Scanning electron microscope (SEM) images of the patterned c-Si wafer surface, (a) before and (b) after excimer-laser-induced planarization [82].. 107
Fig 6.3: The schematic of the in-situ optical probing system used to measure the transient reflectance from the front surface (FTR), the bottom

side of the p-Si thin film (BTR) and the transient transmittance (TT) of probing lasers. 109
Fig 6.4: (a)-(d) The AFM images of the sample surfaces after irradiation at 70%, 75%, 85% and 90% CMT respectively. (e) The plot of RMS surface roughness after planarization versus laser energy. 112
Fig 6.5: (a1) - (d1) The AFM images of the sample surfaces after irradiation under the energy conditions of 70%, 75%, 85% and 90% of CMT; (a2) - (d2) depict the corresponding transient signals. The black, red and blue colors respectively represent the FTR, BTR and TT signals.. 115
Fig 6.6: (a)-(d) phenomenological picture of the melting process sequence during excimer laser irradiation of ELA-generated polycrystalline thin films. 117
Fig 6.7: the schematic of the simulated structure, where the red and green regions are set to be two different c-Si grains forming a grain boundary in the middle. 120
Fig 6.8: (a)-(f) The selected representative time frames in the phase transformation simulation (a) before laser irradiation, (b) at the beginning of laser irradiation, (c) the starting point of melting, (d) when the formed liquid reaches the bottom, (e) when the melting reaches the maximum, (f) some time before complete resolidification, and (g) time-resolved locations of the left gain edge (black lines) and the right grain edge (red lines) at the surface of the film. 122
Fig 7.1: (a) – (d) AMF images of the surface morphology after planarization respectively under the energy conditions of 70%, 77%, 82% and 88% of the CMT, and (e) the plot of the corresponding RMS surface roughness. 127

Fig 7.2: (a1) – (d1) AFM images of the surface morphology after planarization respectively under the laser-energy conditions of 70%, 77%, 82% and 88% of the CMT, and (a2) – (d2) the corresponding FTR, BTR and TT signals recorded by the in-situ optical probing system. The black color, red color and blue colors respectively represent the FTR, BTR and TT signals. 129
Fig 7.3: (a1) – (a3), (b1) – (b3) and (c1) – (c3) schematic diagrams of the melting and solidification processes during planarization experiments respectively of the reported c-Si condition (free surface), the BHF-treated ELA film (free surface) and the as-is ELA film (oxide-capped). The descriptions of and the reasons causing the different melting and solidification scenarios are discussed in the above paragraph. 132
Fig A.1: (a) The bright-field optical microscope image, (b) the corresponding dark-field optical microscope image and (c) the polarized-light-microscopy optical microscope image of the surface of ELA-generated polysilicon thin film. 150
Fig A.2: Schematic diagrams respectively of (a) main SBC system components, (b) raster-scan process over a large processing area, and (c) overlap scanning of spot beam. 152
Fig A.3: Bright-field plane-view TEM images of multiple-scan SBC crystalized regions; the films were processed with the energy density (lower in (a) than (b)) below the CMT... 153

List of Tables

Table 5. 1: The mean values and standard deviations of the p-Si grain size generated with different shot numbers. 89

Table 5. 2: Standard deviations of the α value at selected orientations in 5- and 30-shot conditions. 94

Acknowledgments

Years have been spent on my doctoral study, beginning from getting in touch with and understanding the topic and the related fields, to proposing a scientifically valuable research target followed by diligent work, and, finally, to obtaining meaningful results that could benefit the research fields. Episodes, interruptive but beautiful and grateful, also have been interluded during the years, which made the experience of my whole period of studying at Radical Research Group (RRG) special and unforgettable. The completion of this thesis doesn't only mean getting a conclusion of my research task, which is valuable to the related fields, but, more importantly, also means having learned a method for general scientific investigations as well as having formed an attitude towards my future career and daily life.

Foremostly, I thank Professor James S. Im for all the scientific discussions, instructions and suggestions. Without his guidance, it would not be possible for me to enter and make some achievement in such a research field that I like very much. I am also grateful for his guidance and mentoring regarding how to get along with people and deal with the world. I would like to treat him as my mentor instead of merely the research advisor. He is polite and gentle when delivering his ideas to us. His thoughts and understandings are deep and insightful, but he always likes to express them in a rather 'careless' and 'informal' way, which leaves the listeners no pressure but room to think and motivation to explore. I think this is a philosophy that I learned

from him and treasure very much. I also appreciate the freedom that he gave to me, otherwise I would not get a chance to finish this work.

Besides, I would like to thank all the RRG members whom I chronically worked or shortly got in touched with, especially my schoolmates Wenkai Pan, Jimmy Wang, Ying Wang, Vernon Wang, Ruobing Song, Bonan Shen and Nikita Lisenko. I specially thank Wenkai Pan (my mate) for countless unforgettable things and moments. I also sincerely thank Nikita for intensive proof reading and editing of my thesis as well as Ruobing Song for providing information and material that are helpful to my work.

In addition, I would like to thank Professor Beibei Li in Carnegie Mellon University for her professional instructions about the programing related work in my thesis and her influence on me. I have known her for quite a long time during which she has given me much valuable suggestions when I am on the way to pursue higher and better education. She is a charming person with sterling characteristics that can always influence and encourage me when I needed to make decisions and was facing difficulties.

Furthermore, I would like to thank another mate, Lei Xu, whom I have made during my study at Columbia University. He just graduated from Civil Engineering Department with a Ph.D degree. Lei Xu, Wenkai Pan and I had a lot of time living together as roommates, and had a lot of happy moments. He is a nice and fun person who helped me a lot in my daily life.

I would also like to thank Mechanical Engineering Department and Columbia University for the teaching and the atmosphere. I really like them. Specially, I thank Professor Y. Lawrence Yao for teaching us with clear and solid knowledge in his Advanced Manufacturing class.

I deeply thank my family members. I thank my parents for nurturing me as well as providing mental and financial support whenever I needed. I

thank my parents in law who nurtured my wife and help on looking after my children. I specially thank my wife Qinwen Zhu who is the most wonderful woman that I ever met in my life and continuously encouraged and comforted me when I was facing difficulties. I also thank my children who cooperated very well when I needed to work on my research.

At last, I thank all the friends and relatives who have helped me during the years. I really appreciate your helps and won't forget them.

Chapter 1

Introduction

Most of the common metals, ceramics and semiconductors are polycrystals, consisting of crystallites (often referred to ‘grains’) that vary in size. Advanced manufacturing technologies like low-temperature polycrystalline silicon (LTPS), selective laser melting (SLM) and 3D printing are based on understanding collective crystallite behavior and microstructure control [1]-[3]. For example, in the LTPS process microelectronic transistors are fabricated on p-Si thin films. The subsequent transistor performance is limited primarily by the presence of grain boundaries (GB) as opposed to intragrain defects such as stacking faults and dislocations. Thus the device developers have to design transistors thousands of times larger than the grains to average out the effects of the underlying grain boundaries.

This thesis rigorously, quantitatively and comprehensively analyzes the microstructure evolution of p-Si thin films during Excimer Laser Annealing (ELA). Our developed innovative image-processing-based GB extraction program and our rigorous local microstructure analysis (LMA) scheme are implemented to characterize the GB density. Surface protrusions located at

grain boundaries may also deteriorate transistor performance, so the excimer laser's ability to planarize the p-Si surface is also investigated. The contents of this work (1) for the first time thoroughly analyze the geometry- and location-specific aspects of the ELA-generated microstructure relevant to device performance, (2) present a systematic investigation of the microstructure evolution occurring during multiple shots of the ELA process and (3) reveal the fundamental phase transformation mechanisms of the thin film in the ELA process. The tools and schemes developed for the LMA in this work can also benefit the research of other polycrystalline materials [4]-[10].

1.1 Excimer-Laser Crystallization

Excimer-laser crystallization (ELC) is massively applied in the modern electronic display manufacturing for its ability to effectively transform amorphous silicon (a-Si) thin film into high-quality p-Si even on low-thermal-budget substrates, such as transparent glass or flexible polymer substrate [11]-[16]. Excimer laser crystallization of Si typically starts with an a-Si thin film (tens to hundreds of nanometers thick) deposited on a substrate. Normally plasma-enhanced chemical vapor deposition (PECVD) is used to achieve uniform a-Si deposition under a relatively low temperature (approximately 300°C) and a high deposition rate. Next, excimer laser is utilized to rapidly heat up and melt the a-Si film. Due to the short laser pulse duration and high absorption coefficient of Si in the ultraviolet range, most of the excimer laser energy is absorbed within tens of nanometers below the film surface, leaving the substrate nearly unaffected by the heating. After the laser irradiation ceases, the significant temperature difference between the Si thin film

(normally above 1400°C) and the substrate (around room temperature) results in a rapid film cooling and crystallization during solidification. Combinations of process parameters (such as energy density and pulse duration) and the initial material configuration lead to the establishment of ELC sub-techniques such as excimer-laser-annealing (ELA) and sequential lateral solidification (SLS), which are critical in modern electronic display manufacturing.

1.2 Excimer-Laser Annealing Technique

The excimer laser annealing technique, as a specific one of various ELC techniques, has recently been the most preferred way to manufacture high quality LTPS display panels. It has advantages over the other ELC techniques in cost, scalability and the rate of production of p-Si thin films of high enough quality [17]-[20]. ELA is characterized as a multiple-pulse-per-area partial-melting-based laser crystallization technique capable of converting precursor a-Si films into polycrystalline material. In practice, a 308 nm excimer laser line beam scans over a pre-deposited UV-absorbing a-Si thin film, partially melts the surface, leading to the formation of p-Si with grain size ranging from several tens of nanometers up to the 300 nm range. Normally, around 20 scans at each location are required to produce a p-Si film suitable for the fabrication of large-scale integrated circuits (ICs). Complex microstructure evolution process happens during each scan, as dictated by the intrinsic material properties, the far-from-equilibrium nature of the phase transformation, the partial melting requirement, and the laser beam quality and configuration of the ELA system. Meanwhile, surface protrusions are formed during solidification as a consequence of mass accumulation resulting from the density change in going from liquid to solid [21]-[23].

The microstructure of the ELA film is advertised as uniform and homogenous over a large scale, which would be beneficial for the performance of devices and ICs built on the film. However, in reality researchers and manufacturers suffer from locally nonuniform microstructure within the device length scale, which in fact greatly degrades ICs performance and stability. The locally nonuniform microstructure can be briefly characterized as 1) highly ordered regions coexisting with the less ordered ones and 2) the grain size having a distribution, meaning that most of the grains have similar size, but there inevitably exist very large or very small grains randomly scattered across the whole film. For a long time, numerous efforts have been unfortunately merely devoted to achieving more ordered and uniform grains over the large scale by varying the fabrication conditions. The researchers and manufacturers have failed to appreciate the importance of analyzing the microstructure of ELA-generated p-Si, especially the local microstructural variation on the device length scale and the microstructure evolution during each scan. We argue that studying those aspects is quite meaningful and useful to understand the correlation between the microstructure, the device and the ICs characteristics, as well as the nature of the crystalline evolution during the ELA process.

Thorough microstructure analysis across a significant number of p-Si grains could significantly benefit both the academic research and the industrial implementation of the ELA technique. Findings of such studies can potentially (1) reveal the intrinsic phase transformation mechanisms involved in the ELA process; (2) facilitate the understanding of the influences of the extrinsic factors, such as laser energy, number of irradiation cycles, ambient atmosphere composition and etc., on the final material; (3) link microstructure properties with the performance of the devices fabricated on it; (4) give clues

on how to deal with the location-dependent performance nonuniformity of transistors that the industry is suffering from [24]. Furthermore, the ever-increasing demand of high-resolution displays fuels a pursuit for denser display pixels and smaller pixel size, highlighting the need for precise microstructure management and assessment tools [25]. Thus the necessity to analyze the spatial variation and microstructure of materials like ELA-generated p-Si continuously intensifies. Aside from the internal microstructure, the surface morphology of the ELA-generated Si also deserves careful analysis and investigation. As-generated ELA films exhibit undesired protrusions at the grain boundary junctions, which has been widely recognized as detrimental to the transistor performance due to lowering of the gate material's breakdown voltage [26].

Despite the fact that the ELA-generated Si thin film has been studied for decades and the ELA technique has been implemented in the electronic display manufacturing for many years, surprisingly the investigations reported so far are unfortunately unsystematic, fragmented and sometimes wildly diverging in conclusions. Some fundamental features of phase transformations in ELA-generated Si grains under transient laser irradiation conditions were recently investigated in our group [27]. However, there is still little research conducted on a comprehensive investigation of the microstructure, the evolution of the microstructure, and the surface morphology of the ELA-generated Si films, which has been argued above as essential and will be comprehensively discussed in the following parts of the thesis.

1.3 Approaches for the Work

In this thesis, we firstly conduct a study of the microstructure and the microstructure evolution of the ELA-generated p-Si thin films and secondly attempt to planarize the protrusions existing on the surface, both of which are undoubtedly essential and meaningful, yet not performed in the past. In the study of the microstructure, a novel image-processing-based grain boundary (GB) extraction program and the rigorous local microstructure analysis (LMA) scheme are developed, enabling both grain-size analysis of a statistically significant number of grains and spatial microstructure analysis over an unusually large area. The p-Si thin films are generated by repeated excimer laser irradiation of the same area of precursor a-Si thin films, which were de-hydrogenated and prepared using industry-level state-of-art equipment and process. Transmission electron microscopy (TEM) is employed, specifically focusing on capturing high-quality images of the microstructure over a large area. In the attempt of surface planarization, the surface morphology is captured by an atomic force microscope (AFM). The attempt is conducted by again irradiating an ELA-generated Si thin film using only one shot of excimer-laser irradiation. Based on the difference in the reflection coefficient of molten and solid Si, the dynamics of laser pulse-induced phase transformations during the irradiation are examined by in-situ transient reflection and transmission analysis. The transparency of the substrate allows us to simultaneously measure transient reflectance of both surface-side and film-substrate-interface side, as well as the transient transmittance throughout the thickness of the entire film. Together, these in-situ signals collectively depict a spatiotemporal picture of a typical laser-induced transformation for the entire duration of an excimer laser pulse. Melting scenarios under different

surface conditions (i.e., passivating oxide layer and free surface) are examined and compared via in-situ reflectance and transmittance analysis. Thereafter, numerical simulation is performed on the software developed previously in our group to link the current study to previous work and leverage our fundamental understanding. The results provide clues about the rapid heat flow and first-order phase transformations in the thin-film system under far-from-equilibrium conditions. It is worth noting that (1) the innovatively developed image-processing-based GB extraction program and the LMA scheme, (2) high-quality samples, (3) unique sample preparation and TEM characterization skills, (4) the availability of the simultaneous measurement of transient reflectance and transmittance and (5) the numerical simulation put together is what gave us the fortuitous opportunity to comprehensively analyze and obtain a thorough understanding of the microstructure and the surface morphology of the ELA-generated p-Si thin film material.

The main achievements of this thesis include: (1) the development and the demonstration of the GB extraction program and the LMA scheme for the first time enabling precise grain-size analysis of a statistically significant number of grains and spatial microstructure analysis over a sufficiently large area; (2) the unprecedentedly comprehensive and systematic microstructure analysis of the ELA-generated p-Si thin films; (3) the demonstration of a successful surface planarization of the BHF-treated ELA films; and (4) identification of the unusual anisotropic scenario of melting and subsequent solidification during the planarization. This work contributes to the related technological community by advancing the understanding of the ELA process, in particular by the drawing the link between the process conditions, the resulting material microstructure and the subsequent transistor performance. Scientific society generally interested in the study of phase transformations in

polycrystalline materials can also benefit from the insights of this thorough study of melting and solidification of Si thin films.

1.4 Organization of the Dissertation

The remainder of this dissertation is organized into the following chapters:

Chapter 2 "Background and Motivation" provides the fundamental knowledge required to understand the ELA process and gives an overview of the previous studies. The concept of the LMA is presented.

Chapter 3 "An Image-processing-based Method for Grain Boundary Extraction" introduces and describes the development of the GB extraction program to distill a grain boundary map (GB map) from TEM images. The chapter includes fundamental theories, definitions, formulation, the algorithm and the pseudocode.

Chapter 4 "Comprehensive Microstructure Analysis of the ELA Si Thin Film" demonstrates the local microstructure analysis (LMA) scheme to quantitatively and systematically analyze the transistor performance-related microstructure of ELA films. Grain-size statistics, local variation of the GB density, preferential transistor orientation and periodic grain arrangement are analyzed. The relative GB density and the area fraction of periodicity are defined in order to quantitatively describe the local variation of the GB density and the extent of the periodic grain arrangement. According to our analysis, the impact of the GB density variation depends on the transistor size and orientation.

Chapter 5 "Excimer-laser Annealing Experiments and Comprehensive Microstructure Analysis" first describes the experiment details to generate the ELA thin films and the unique skills to acquire high-quality TEM images.

Then we systematically analyze the microstructure of the samples generated after a number of laser irradiation cycles (5, 10, 15, 20, 25 and 30 shots) by adopting the LMA scheme. The analysis reveals valuable information about the microstructure evolution and the phase transformation mechanisms of the Si thin film during the ELA process.

Chapter 6 “The Surface Morphology of the ELA Si thin film and the Attempt of Planarization” first presents the atomic force microscopy (AFM) work to capture the characteristics of the surface protrusions that are detrimental to the performance of TFTs. Then the attempts of minimizing the surface protrusions are conducted, which are inspired by a previous work done to planarize the rough surface of single crystalline Si (referred to as c-Si). The results of our first unsuccessful planarization attempt, along with the transient reflectance and transmittance signals, imply a different melting and solidification scenario in our poly-Si compared to c-Si. Based on the observations and a logical deduction the numerical simulation is performed to more comprehensively present the scenario. Finally, the melting and solidification process is proposed as (1) melting initiating at the grain boundaries and (2) the melting and solidification proceeding through a lateral movement of vertically formed liquid/solid interface.

Chapter 7 “Surface Melting of the Treated ELA Si thin film” conducts planarization again after removing the surface oxide from the sample while keeping the other conditions the same in Chapter 6. Maximum surface planarization is successfully achieved at 41.8%. The melting and solidification scenario which is different from that in Chapter 6 is identified by comparing the AFM images and the transient reflectance signals with those in Chapter 6. We argue that the surface oxide passivates the oxide/Si interface and results in the lower excess free energy at the oxide/Si interface compared

with that at the grain boundaries. We conclude that melting under the excimer laser irradiation prefers to happen at the high excess-free energy cites such as the free-surface and the grain boundaries, and can hardly be triggered at low excess-free energy cites such as the inert oxide/Si interface.

Chapter 8 “Conclusions” summarizes the work done in this dissertation and suggests a direction of the future research.

Chapter 2

Background and Motivation

The excimer-laser annealing (ELA) technique has been widely applied in the manufacturing of modern electronic displays due to its high applicability to the fabrication of thin film transistors on low-thermal-budget substrates. The first demonstration of applying ELA to p-Si TFT fabrication can be traced back to 1986 and, since then, intensive studies has been conducted in this field [28]. Due to the application-driven nature of this topic, the previous investigations of the ELA process and the generated Si thin film have mostly been focused on studying the correlations among the processing parameters (such as the laser energy, ambient temperature, shot number and etc.), material properties (mostly electrical and mechanical properties), the device performance and the final product performance [29]-[33]. However, the microstructure of the ELA-generated p-Si thin film, which is the centerpiece connecting all the above concerns, unfortunately lacks sufficient investigation. The microstructure of an ELA-generated p-Si thin film is the result of a complex far-from-equilibrium multiple-pulse-per-area process-parameter-dependent melt-mediated laser-crystallization process. It couples

non-trivial mechanisms, including laser-material interaction, rapid thermal evolution, laser crystallization of precursor a-Si thin film and phase transition of p-Si thin film, and is heavily influenced by various processing parameters such as laser energy, shot number, ambient gas ingredients and etc. In this chapter, we first provide the related theoretical background of the melt-mediated phase transformations of Si and the excimer laser crystallization (ELC) of Si thin films to provide the foundation and facilitate the understanding of the specific ELA technique. Then, we overview the previous research and the current state of the ELA technique, followed by the introduction of the device performance-related microstructure and surface morphology of ELA films. Furthermore, we demonstrate the existence of the microstructure nonuniformity and propose the concept of the local microstructure analysis (LMA) scheme. At last, we present our research motivation and strategy.

2.1 Fundamental Framework of Laser Crystallization

The excimer-laser annealing of a Si thin film is, in nature, all about melting and solidification of an elemental material, which is fundamentally governed by the principles of thermodynamics and kinetics of the phase transformation of the material, even though various melting and solidification details may also come from different sample configurations, processing methods and conditions. In this section, we introduce the necessary knowledge of thermodynamics and kinetics involved in the work of this thesis.

2.1.1 Thermodynamics of Melting and Solidification

The thermodynamics of a system dictate the possible phase transitions under given conditions. The phase transition of a system is driven by the minimization of the overall Gibbs free energy of the system. The relation between Gibbs free energies of liquid, amorphous and crystalline Si as a function of temperature under one atmosphere is schematically shown in Figure 2.1. This provides the thermodynamic basis for identifying the various possible phase transformations that can occur in Si [34]. The a-Si phase is metastable with melting temperature around 1460K, which is lower than that (around 1685K) of c-Si [34]. The phase transformation between liquid and solid Si is a first order phase transition involving creation and movement of solid/liquid interface [35].

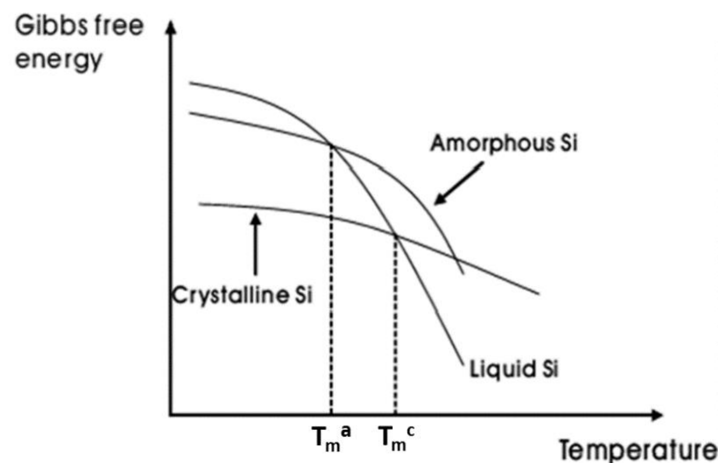

Figure 2.1: The isobaric Gibbs free energies versus temperature respectively of crystalline (c-Si), amorphous (a-Si) and liquid (l-Si) phase of Si. Tmc and Tma are the equilibrium melting temperatures respectively of c-Si and a-Si. In general, when the temperature is above the equilibrium melting temperature, solid Si (amorphous or crystalline phase) melts into liquid. When the temperature drops below the equilibrium melting temperature, liquid Si solidifies. The solid phase (amorphous, crystalline or polycrystalline) and the degree of

crystallinity (defective or not defective) after solidification are affected by various factors during solidification such as the intrinsic material properties, unmelted residues, the cooling rate and etc.

2.1.2 Kinetics of melting and solidification

Upon the formation of solid/liquid interface the rate at which the interface moves is governed by the interface response function (IRF) (Equation 2.1) given as [36]:

$$v(T) = v_0 \exp\left(-\frac{Q}{kT}\right)\left[1 - \exp\left(-\frac{\Delta G_{ls}(T)}{kT}\right)\right] \quad (2.1)$$

where T is the solid/liquid-interfacial temperature, v_0 is a kinetic prefactor in the same unit of velocity, Q is the activation energy for the self-diffusion of atoms near the interface, k is the Boltzmann constant, and ΔG_{ls} is the difference of Gibbs free energy per atom between the liquid and solid. As k is a constant and Q, ΔG_{ls} and v_0 depend on the intrinsic material properties, the velocity of the interface motion largely depends on the temperature at the solid/liquid interface. The IRF describes the kinetics of melting and solidification under far-from-equilibrium conditions (which are typically encountered in the laser crystallization of Si thin films). At the temperature near the melting point where ΔG_{ls} is sufficiently small, the IRF can be approximately rewritten as (Equation 2.2):

$$v(T) = c * \Delta T \quad (2.2)$$

where c is a constant and $\Delta T = T_m - T$ (T_m is the equilibrium melting temperature of the crystalline or amorphous phase), meaning melting when $v(T)$ is negative and solidification when it is positive.

IRF of Si is reproduced and shown in Figure 2.2 by taking the experiment data into consideration [37]. It can be seen that the melting-solidification of a-Si and c-Si respectively follows two separate curves showing that (1) the equilibrium melting temperature of a-Si is lower than that of c-Si, and (2) amorphous solidification (i.e., amorphization) can happen if a large degree of supercooling is achieved during solidification.

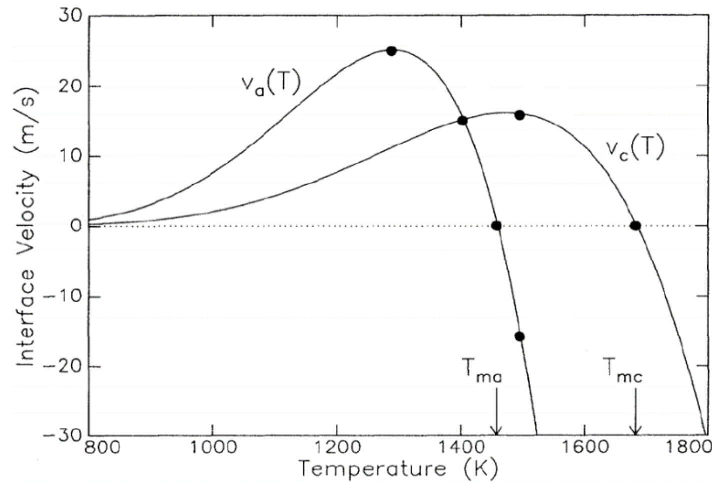

Figure 2.2: Interface velocity versus temperature respectively of c-Si ($V_c(T)$) and a-Si ($V_a(T)$). T_{mc} and T_{ma} denote the equilibrium melting temperature of c-Si and that of a-Si. The interface velocity describes the rate at which solid/liquid interface moves during melting or solidification in a microscopic view. The temperature here refers to as the temperature at the local solid/liquid interface.

2.1.3 The Gibbs-Thomson Effect

Although the solid to liquid phase transition theoretically happens when the temperature reaches the equilibrium melting point, in reality various factors including crystal defects, local curvatures, passive or active interfaces

and surfaces can also largely affect the melting temperature of a specific location, making the local melting temperature differ from the bulk melting temperature. The curvature effect is also called the Gibbs-Thomson effect as formulated by (Equation 2.3) [38][39]:

$$T_m^{local} = T_{mp}(1 - \frac{2\sigma_{sl}}{\Delta H_f}\rho_{local}) \quad (2.3)$$

where T_m^{local} is the local equilibrium melting temperature, T_{mp} is the bulk equilibrium melting point, σ_{sl} is the solid/liquid interfacial energy, ΔH_f is the enthalpy of fusion, and ρ_{local} is the local curvature of the solid phase. Depending on the sign of the local curvature, the local equilibrium melting temperature may be either elevated or depressed.

2.2 Related Background Knowledge of ELC Si Thin Films

The excimer-laser induced crystallization process, such as the ELA, can be majorly divided into to two physical processes. One is the laser-material interaction, where various optical phenomena happen, including reflection, transmission and absorption, resulting in the coupling of a certain amount of laser energy into the material that is subsequently converted into heat [40]. It should be noted that, in reality, the spatial distribution of laser intensity may not be uniform, which leads to nonuniform heat generation on the being-irradiated area [41]. The second one is the phase transformation, which is triggered by the input heat and determined collectively by intrinsic as well as extrinsic factors, such as the phase-transformation-related material properties, microstructure details, the thermal evolution, the temperature distribution and etc [42][43]. The microstructure generated after phase transformation records

valuable information of the history of the above two processes and dictates material's electrical and mechanical properties. In this section, we introduce the laser-material interaction of Si and present the critical melting regimes. Those are classified based on the maximum melting depth achieved by excimer-laser induced melting and lead to distinguishable microstructures after solidification. We also describe an effective time-resolved method, which is also adopted in our work, to trace the phase evolution during the melting and solidification process via recording transient reflectance and transmittance variations from in-situ probing lasers.

2.2.1 Laser-material Interaction of Si

The way the electromagnetic waves comprising laser irradiation (or laser beam), interact with material can be effectively described by the traditional optics concepts, such as diffraction, reflection, absorption, transmission, scattering and etc. The reflection and absorption of elementary Si can be quantified by the refractive index and absorption coefficient which are shown in the diagram of Figure 2.5, while the transmission is the fraction of energy which is neither reflected nor absorbed. Scattering and diffraction, which depend not only on the optical properties of a material but also on the geometric factors, should also be taken into consideration if the irradiated area is planar. In general, the energy deposition profile that describes the amount of laser energy penetrated into the absorbing material as a function of depth (i.e. the distance that the electromagnetic wave can reach below the surface) is formulated as (Equation 2.4) [40]:

$$I(x) = I_s \exp(-\alpha x)\,, \text{where } I_s = I_0 * (1 - R) \qquad (2.4)$$

where $I(x)$ denotes the laser energy as a function of depth, I_s is the amount of laser energy that enters the material, α is the absorption coefficient, x is the distance under the irradiated surface, I_0 is the total laser energy reaching the surface of the material and R is the reflectivity of the material.

From the above equation, it can be seen that 1) the laser energy decays exponentially after entering the material and 2) most of the absorption of laser energy happens within a depth of α^{-1} (referred to as the absorption depth or skin depth). It should be noted that the reflectivity and the absorption coefficient of Si are wavelength-dependent and also significantly affected by the phase and temperature of the material. When applied to the case of c-Si and 308nm wavelength laser beam used in the ELA, Figure 2.3 and Equation 2.4 predict that most of the laser energy would be absorbed within the first 10nm below the irradiated surface [40].

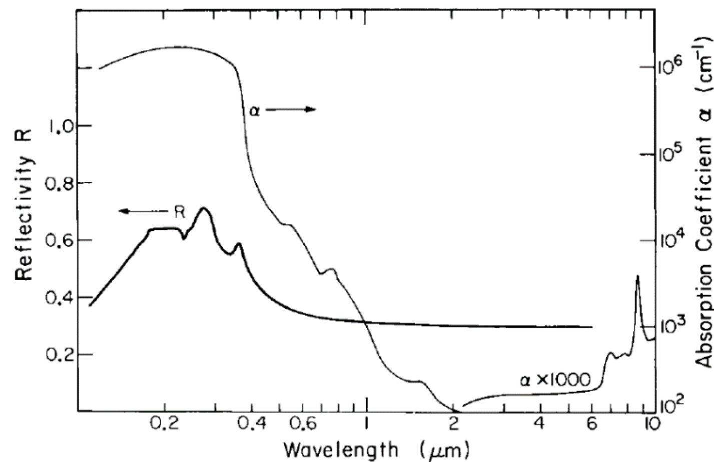

Figure 2.3: Reflectivity and absorption coefficient of c-Si at room temperature, which are wavelength dependent. It can be seen that Si is very absorptive for UV light (the range of the excimer laser) and becomes much less absorptive for the light with larger wavelength.

In the ELA process of Si, where the pulse duration is roughly several tens of nanoseconds, the Si surface melts while the laser is still on. The molten Si has metallic characteristics and is much more reflective compared to the solid phase, resulting in an abrupt increase of the reflectivity especially for the long-wavelength light. Thus long-wavelength probing laser that cannot be effectively absorbed by Si thin films can be used as a very effective indicator of the phase change of the film. Figure 2.4 shows the previously reported abrupt increase of the transient reflectance upon melting and later decrease during resolidification of Si [36].

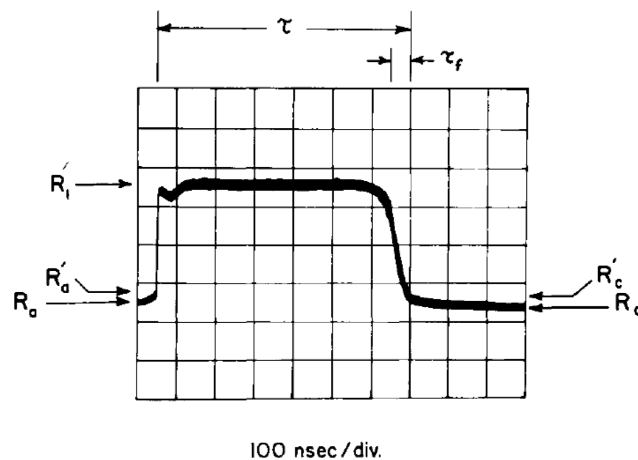

Figure 2.4: Time-resolved reflectance change of the probing laser during melting and solidification of Si upon laser irradiation, where R_a, R_l and R_c respectively denote the reflectance of amorphous, liquid and crystalline Si. Red laser (with wavelength around 0.7 μm) is normally used as the probing laser, which does not affect phase transformation. The reflectivity of the liquid phase is much higher than that of the solid phase (amorphous or crystalline). Thus, the reflectance increases dramatically when the solid phase transits into the liquid phase and vice versa. The plateau within the time range of τ shown in the figure indicates that a continuously liquid layer appears at the surface and sustains for a period of τ. τ_f is the period of solidification.

It should be noted that the reasons why ELA of Si thin film is a far-from equilibrium process are (1) the rapid heating (in tens of nanoseconds) as a result of a sudden input of a large amount of energy via an excimer-laser pulse, (2) the very limited absorption depth below the surface (in the order around 10nm) that converts most of the absorbed energy into heat, (3) the high cooling rate due to the much larger heat diffusion length (in the order of several micrometers) than the absorption depth, as schematically shown in Figure 2.5 [36], (4) the excellent thermal conductivity at the Si/substrate (normally Si oxide) interface and (5) the large heat capacity of the thick substrate (in the thickness of millimeters).

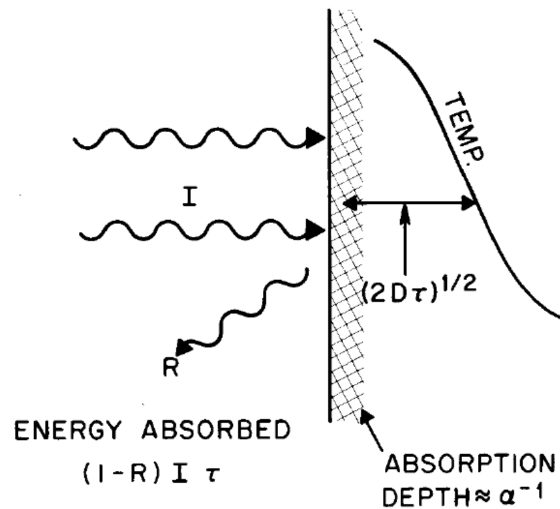

Figure 2.5: A schematic illustrating light and material interaction of planar Si surface. When light is incident upon the planar surface of Si, part of the energy is reflected and part of the energy is absorbed. Most of the absorption happens within the absorption depth, which is the inverse of the absorption coefficient. The absorbed energy is converted into heat with heat diffusion length defined as $\sqrt{2D\tau}$ where D is the diffusivity and τ is the characteristic time. In ELA, where the wavelength of the excimer laser is 308nm and the pulse duration is around 30ns, the absorption depth and the heat diffusion length are respectively calculated to be around 10nm and 1.6μm. Thus, the cooling rate is extremely high in ELA due to the fact that the thickness of the film is only 50nm and the pulse duration is only 30ns.

2.2.2 Different Melting Regimes

The crystallization of Si thin film during the ELA process is characterized as laser-induced and melt-mediated. Melting is important in the ELA process since solidification is a consequence of melting. The laser-induced melting can be categorized into three regimes, namely partial melting, complete melting and near-complete melting [42]. They are distinguished by the maximum depth of melting achieved during laser irradiation, as schematically illustrated in Figure 2.6. The maximum melting depth is mostly determined by the energy density of the incident laser beam, while also being affected by several other factors including film thickness, the microstructure and surface morphology. Partial melting happens when the energy density of the incident laser beam is low, which results in a continuous layer of unmelted solid underneath the molten (liquid) layer (Fig. 2.6 (a)). Under such condition, solidification initiates from the molten/unmelted interface when the temperature of interface drops to the equilibrium point, and proceeds into the liquid region. If the energy density of the incident laser beam is sufficiently high, the entire film transforms into liquid upon irradiation and no solid sustains (Fig. 2.6 (c)). In this case, the solidification is triggered via nucleation and proceeds as the growth of the nucleus. The energy density of the laser beam required for complete melting is defined as the complete melting threshold (CMT) of the thin film. There exists a narrow sub-regime of energy density (near-complete melting regime) just below the CMT that leaves discontinuous unmelted solid islands where solidification can initiate.

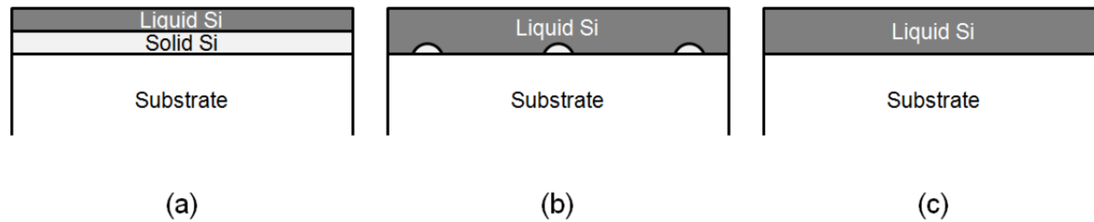

Figure 2.6: Schematics of (a) partial melting, (b) near-complete melting, and (c) complete melting regimes. In the partial melting regime, a continuous layer of unmelted solid sustains, while, in complete melting regime, the entire film transforms into liquid phase during laser irradiation. The near complete melting regime lies between partial melting and complete regimes, where sparsely distributed unmelted islands persist during laser irradiation.

The three melting regimes result in different microstructures of the resolidified films after laser irradiation. The grains generated after partial melting and complete melting are, in common, all very fine and defective, but still with substantially different characteristics. In contrast, distinctly large grains can be found in the near-complete-melting regime due to the so-called super-lateral growth (SLG) of the solid seeded on the sparsely distributed unmelted solid residual during melting. Thus the near-complete-melting regime is also called SLG regime. The differences of the microstructures generated under the three melting regimes are presented in Figure 2.7 [42]. In the ELA process laser energy is frequently tuned to meet with different demands of the products. Therefore, by grasping the three melting regimes, researchers and engineers can better understand the influence of the laser energy on the microstructure of the generated films.

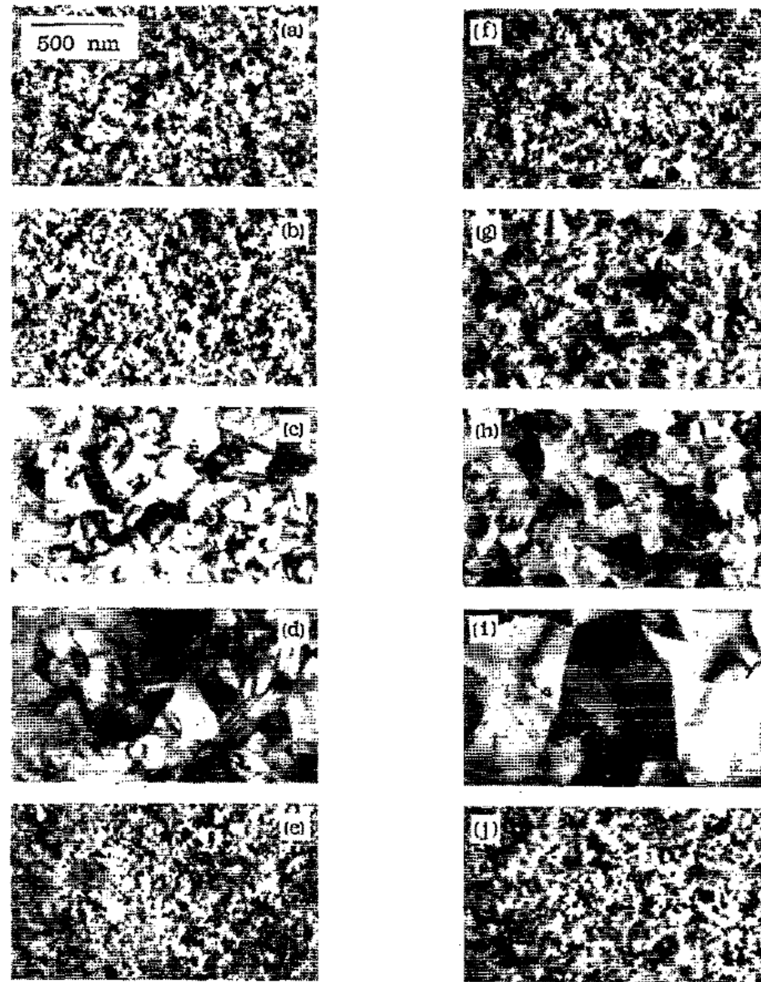

Figure 2.7: Plane-view bright-field TEM images of the microstructure of the laser crystallized precursor a-Si thin films in partial-melting regime ((a), (b), (c), (f), (g) and (h)), near-complete-melting regime ((d) and (i)) and complete-melting regime ((e) and (j)) [42]. The only difference between the sequences of (a)-(e) and (f)-(j) is the ambient temperature, which are respectively room temperature and 550°C. Here the only influence of the lifted temperature is the enlargement of the generated grains before the onset of complete melting. In ELA technique, the laser energy that is often tuned to meet the product demands is an important processing parameter, which could largely affect the final microstructure of the generated films. Thus, the causal relationship between the generated microstructure and the laser energy needs to be grasped.

2.2.3 Crystallization of a-Si Thin Films in Partial-melting Regime

As mentioned previously, the ELA process necessarily requires multiple irradiation cycles in a partial-melting regime. The first laser pulse transforms the a-Si into p-Si, leaving a very defective and fine-grain material as shown in (a), (b) and (c) in Figure 2.7. The definition of the partial melting regime only describes the maximum extent of melting that the film can achieve during laser irradiation. The complex phase transformation occurring at this initial stage of ELA is termed explosive crystallization (EC) [44]. Upon irradiation of the first laser pulse, the very surface layer of a-Si promptly melts into liquid that becomes highly reflective and thermally dissipative, which considerably slows down the heating rate of the film. The temperature at the interface between the liquid and the unmelted amorphous solid drops as a result of the slowing heating rate and the substantial heat conduction below the liquid/solid interface. When the interface temperature reaches the equilibrium point, heterogeneous nucleation occurs followed by subsequent solidification at the interface. The latent heat released right after the heterogeneous nucleation, together with the heat converted from the still-on laser irradiation increase the local temperature around the heterogeneous nucleus. Then the amorphous solid underneath the dense heterogeneous nucleation cites melts, forming a buried liquid layer between the newly formed solid and the unmelted amorphous solid. Here, we need to keep in mind that the equilibrium temperature of a-Si is about 200K below that of c-Si. Solidification proceeds from the crystallized solid into the buried liquid layer and continuously releases latent heat, which maintains the temperature at the liquid/amorphous interface above the equilibrium temperature of the a-

Si and sustains the melting throughout the entire thickness of the thin film. Figure 2.8 schematically illustrates the explosive crystallization process, which was carefully investigated in the past comprehensive work done in our group [45].

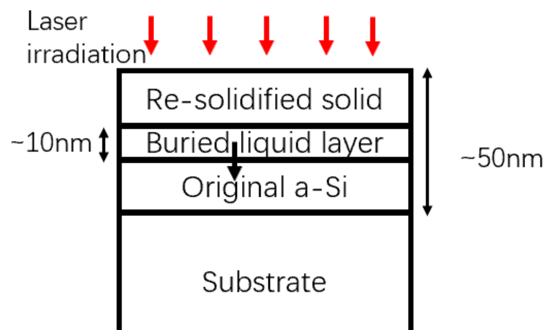

Figure 2.8: Schematic diagram illustrating the explosive crystallization phenomenon of a precursor a-Si thin film during the first laser shot in the ELA process, representing the fundamental phase transformation mechanism involved in the partial melting regime of a-Si films upon excimer laser irradiation. The melting and solidification in the explosive crystallization process happens through a moving buried liquid layer. The material in front of the moving liquid layer continuously melts upon the arrival of the liquid layer, while the material behind the liquid layer resolidifies. The definition of partial melting regime in the above subsection only describes the extent of melting that a film can achieve but has nothing to do with the phase transformation mechanisms.

2.2.4 In-situ probing of Transient Reflectance and Transmittance During Laser-induced Phase Transformation of Si Thin Film

It has been introduced above that the liquid phase of Si is metallic and thus much more reflective compared with solid phase. This allows in-*situ* and time-resolved recording of the transient reflectance and transmittance of probing lasers (not significantly absorbed by Si) during ELA process, which

can provide spatiotemporal information about the melting and solidification process. Three types of transient signals are mostly used which are respectively front-side transient reflectance (FTR), back-side transient reflectance (BTR) and transient transmittance (TT). The FTR and BTR signals measure the transient reflectance changes respectively at the front surface and bottom surface of the Si film while TT signal measures the transient transmittance change through the entire thickness of the film. The schematics shown in Figure 2.9 give an ideal and simplest example of the evolution of FTR, BTR and TT signals during melting and solidification of a Si thin film. The FTR signal increases with the formation of liquid Si at the front surface and reaches a plateau when a continuous liquid layer forms [27]. The TT signal behaves just inversely to the FTR signal. The BTR signal oscillates, which is caused by the optical interference due to the thickness variation of the solid during the melting and solidification process.

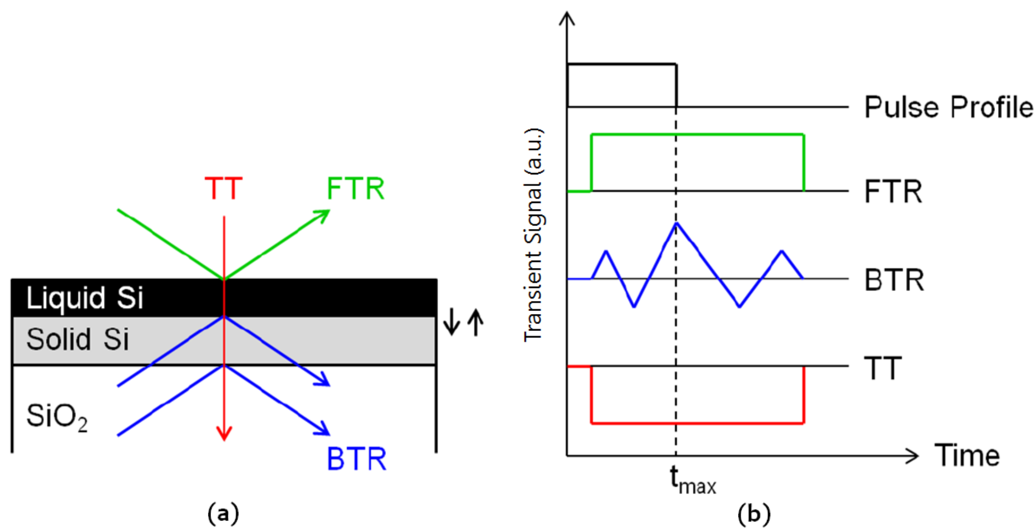

Figure 2.9: (a) Schematic diagram of the melting and solidification process of a Si film, where the front surface of the film first transforms into a continuous liquid layer and the melting or solidification proceeds respectively as the downward extension or the upward shrinkage of the thickness of the liquid layer. (b) Schematic diagram of the corresponding time-resolved transient signals of probing lasers. The black, green, blue and red colors

respectively represent the transient signal of one excimer laser pulse, the transient reflectance signal of a probing laser at front side (FTR), the transient reflectance signal of a probing laser at bottom side (BTR) and the transient transmittance signal of a probing laser throughout the entire film (TT). These schematics give an idea of how the signals would respond to the phase transition.

2.3 Related Background Knowledge of the ELA Technique

As mentioned above, the excimer-laser annealing of Si thin films is widely applied in the manufacturing of low-thermal-budget substrate-compatible backplanes for modern electronic displays, making it a valuable application-driven research topic. A closer examination of the method reveals that this rather complex crystallization method involves (1) explosive crystallization of the deposited material at the leading edge of the nominally top-hat shaped beam, and (2) heterogeneous melting-and-solidification cycles of the first shot crystallized polycrystalline film that gradually leads (with increasing shot number) to grain size increase and overall uniformity improvement. As can be imagined from the very nature of the process (i.e., it involves explosive crystallization at the non-uniform portion of the beam, as well as history-, local-energy-deposition-, and local-microstructure-dependent changes that take place during the subsequent melting and solidification cycles), there is a number of extrinsic/intrinsic variables and parameters that affect the spatial uniformity of the microstructure at various length scales (including and especially at small scales). This is in contrast to “classical” polycrystalline microstructures that may be obtained via globally uniform stochastic processes (e.g., those formed through constant nucleation and growth rates, grain growth, etc.).

The microstructure of the generated p-Si film dictates the electrical material properties such as the field-effect carrier mobility and I-V characteristics, which determine the application of the material [46-48]. In this section we first overview the previous research of the ELA technique and the current status of its application in modern display manufacturing. Then, we describe the microstructure and surface morphology of ELA films as well as disclose their influences on the electrical properties of the material and on the device performance. In the end, we conceptually present our local microstructure analysis (LMA) scheme designed to comprehensive analyze the device performance-related aspects of the ELA microstructure. We note that the comprehensive analysis and the surface planarization constitute the major focus of this thesis.

2.3.1 Overview of the ELA Technique

The research and application of the ELA technique bloomed due to the huge demand of high-quality and cost-effective p-Si thin films for the fabrication of high-performance thin film transistors. Among various potential technologies including both laser and non-laser crystallization of Si that have been intensively studied, the ELA technology was selected and became *the* technology for the manufacturing of TFT backplane in modern electronic displays. Ever since the first report of the demonstration using ELA to increase the performance of TFTs in 1986 [28], the study of this technology became application-driven. The study of its fundamental aspects was intensively conducted during the late 1980s, the period of 1990s and the early 2000s, while the development of its industrial application started around 2010 [29][49]-[52]. *T. Sameshima et al*, who was the pioneer and firstly reported

using ELA to improve the performance of TFTs, along with other researchers performed intensive studies mainly focusing on testing various processing parameters and conditions, such as laser energy, shot numbers, ambient-gas ingredients, ambient temperature, precursor material and preexisting surface roughness [53]-[55]. They attempted to improve the electrical properties of the annealed Si film and the performance of TFTs, but unfortunately missed an essential bridging part standing in between of ELA process and the electrical properties of the material, which is the microstructure. Only a few researches investigated the microstructure [42][43][56], and the knowledge in this field is still severely insufficient. Typically, only one parameter, namely the average grain size, has been unfairly identified and used to capture the characteristics of the microstructure [57][58]. The result of such investigation of the microstructure is shown in Figure 2.10 [57]. Besides, it took years for researchers to debate about the phase transformation mechanism taking place in the ELA process, until the clear experimental observation and the definition of the three melting regimes (i.e. partial melting, near-complete melting and complete melting regimes) was reported from *Im et al* [42]. Over the decades, surprisingly researchers omitted the importance of systematically analyzing the microstructure of ELA generated p-Si, especially the spatial microstructural variation within device scale and the microstructure evolution during each irradiation cycle, that could be very useful to understand the correlation between the microstructure, the device performance and the nature of grain evolution during the ELA process. In fact, the microstructure serves as the hub linking the miscellaneous process parameters, the fundamental phase transformation and the device performance-related material properties. Upon reviewing the previous studies, we conclude and emphasize that the comprehensive and systematic investigation of the microstructure, as an

essential but missing aspect in the study of ELA process and the generated material, would benefit both the scientific research and the industrial implementation.

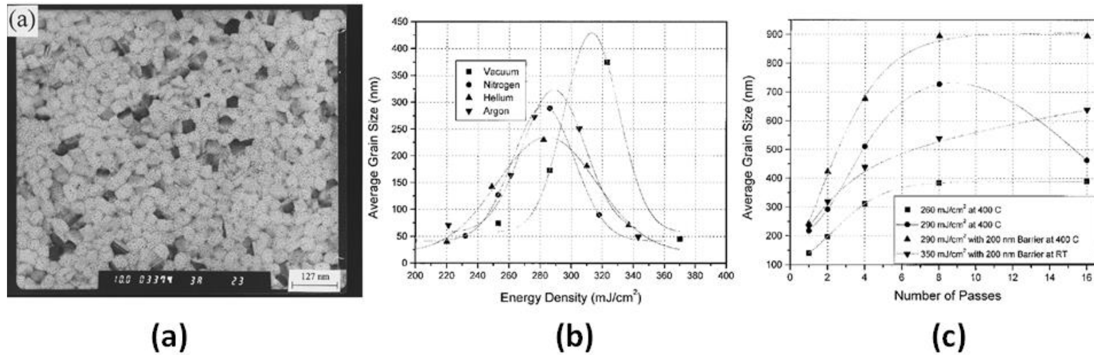

Figure 2.10: (a) The planar-view bright-field TEM image of the microstructure of an ELA-generated p-Si thin film, and (b) diagrams of the average grain size versus excimer-laser energy under different gas-ingredient conditions and (c) the average grain size versus per-area laser-shot numbers under different experimental conditions [57]. In the previous studies of ELA, researches used average grain size as the only one parameter to capture the overall microstructure of the generated film, which unfortunately omits many valuable characteristics that could largely affect the material properties of the generated films, such as the statistical distribution of the grain sizes and the spatial grain-size distribution.

2.3.2 The ELA Technique in Modern Electronic Display

The demand for high definition display devices, starting from HD (high definition), full-HD to the recent UHD (ultra-HD), has been continuously increasing for decades, requiring progressively higher pixel density, higher color saturation, wider viewing angles, shorter response times and higher brightness [60][61]. The requirements of the advanced displays inevitably lead to the replacement of a-Si by p-Si material for fabricating the TFT backplane of the display panels, mainly due to the much higher carrier

mobility of the p-Si thin film (~200cm^2/Vs) compared with that of the a-Si thin film (~1 cm^2/Vs) [62][63].

The ELA technology, as a specific type of the LTPS technology that is compatible with low-thermal budget substrate such as glass, has become the only preferred method to massively manufacture the LTPS films of the TFT backplane in the current electronic display industry due to its balance of functionality, yield, cost and scalability to large substrates. Therefore, the ELA technology is influencing a substantial amount of the global industrial market of display panels, which was valued at USD 128.73 billion in the year of 2018 and is expected to reach USD 165 billion by 2024 [64]. Among those is the global market of UHD display panels that reached more than USD 60 billion with an expected CAGR (compound annual growth rate) of 25% in the next 5 years [65]. The high definition primarily relies on the pixel density, normally defined in the unit of pixel per inch (PPI), of a flat panel. The highest PPI of the recent 8K UHD display panel has reached 1835, meaning one pixel in 138µm, with the TFT size of several tens of square micrometers.

The equipment used in the ELA involves an assortment of tunable processing parameters and conditions such as the laser energy, beam shape, shot numbers, ambient-gas ingredients, ambient temperature, precursor material, preexisting surface roughness. Figure 2.11 (a) shows a currently used excimer laser system and the Figure 2.11 (b) schematically illustrates the laser scanning method in the ELA process. High-power excimer laser pulses, with 308nm wavelength and short pulse duration (in the order of several tens of nanoseconds), are sequentially generated in the oscillation chamber and configured into a long and narrow beam with around 1500mm in length and 0.4mm in width through a set of optical lenses, to sequentially irradiate the surface of precursor de-hydrogenated a-Si thin film pre-deposited on a glass

substrate. The substrate translates at a certain speed to ensure each location experiences around 20 shots of laser irradiation, meaning that each area of the Si film repeatedly melts and resolidifies around 20 times during the entire process [17]. It should be noted that the energy distribution in the longitudinal and transverse directions of the laser beam may not be perfectly uniform, and some pulse-to-pulse energy fluctuation is also possible. These two factors lead to spatiotemporal nonuniformity of laser energy deposition and contribute to the spatial nonuniformity of the microstructure over the processed area.

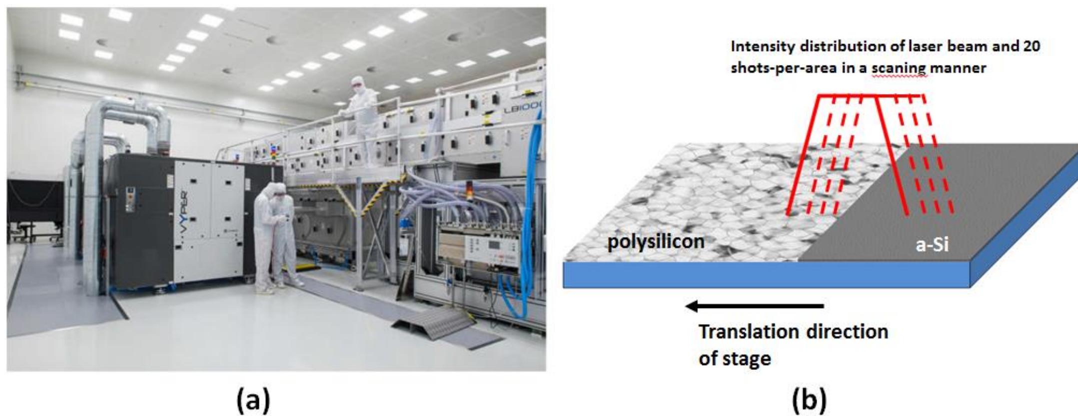

Figure 2.11: (a) A picture of the state-of-art excimer-laser system used in the current ELA manufacturing, developed by Coherent, Inc., and (b) a schematic diagram illustrating the laser-scan process in the ELA. The excimer laser beam is configured into long (1500mm) and narrow (0.4mm) shape. As the backplane panel translates, each location receives around 20 shots of laser pulses. There are inevitable energy slopes at the two edges in the transverse direction of the beam, leading to nonuniform energy distribution in this direction, which could contribute to the spatial nonuniformity of the microstructure of the ELA films.

2.3.3 The Microstructure and Surface Morphology of ELA Si Thin Films

The ELA microstructure consists of numerous small uniformly and regularly distributed grains, typically exhibiting square-like geometry. The

surface of ELA film is rough and protrusion-rich. Figure 2.12 shows the microstructure and surface morphology of a typical ELA-generated p-Si thin film captured by transmission electron microscope (TEM) and atomic force microscope (AFM). When ELA is done correctly, (1) the grains are generally free from intra-grain defects; (2) the grains take on a square-like shape and uniform in size; (3) grains seem to be arranged periodically; (4) the thickness of the film abruptly increases at the grain boundaries (referred to as protrusions), as identified in Figure 2.11 (b). Besides, it should also be noted that the grains are columnar in vertical direction with a thickness around 50nm. For the remainder of this thesis the AFM images are presented with deflection error contrast (original units are Newtons), where the brightness is related to the slope of the protrusions. This creates an effect as if the relief was illuminated by a light source on its side (light coming from the right in Figure 2.12(b)) and shows the protrusion shape more vividly than a direct height plot. TEM image contrast is attributed to the thickness differences between the grain bodies and interiors, as well as to local stress fields inside the grains.

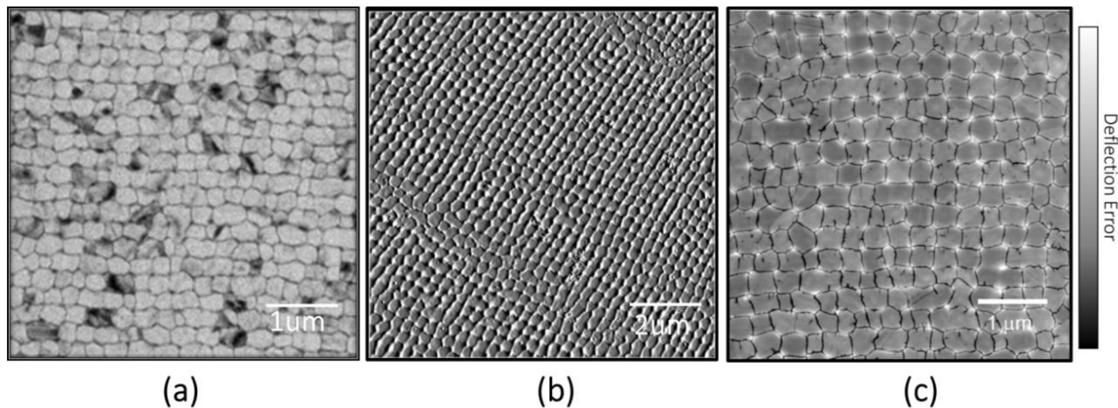

Figure 2.12: (a) The plane-view bright-field TEM image of the ELA grains, (b) an AFM image of the ELA grains and (c) an AFM image of the boundary-etched p-Si thin film, which was done and reported by other researchers [21]. The grains are intragrain defect-free (identified from the clean grain interior shown in the image (a)) and the protrusions

are formed at grain boundaries (by comparison of image (b) and (c). Thus, we claim that the microstructure is mainly concerned with the grain boundaries and the surface morphology is mainly about the protrusions. <I still think image (b) and (c) should be swapped, because the deflection error scale bar refers to image (b), not the other two. (c) is actually plotting height.>

During the 20 repetitions of laser-induced melting and resolidification, the microstructure and the surface of the p-Si thin film evolves. Figure 2.13 captures the microstructure and the surface morphology of p-Si films after being irradiated respectively with a smaller number ((a1) and (a2)), a medium number ((b1) and (b2)) and a large number ((c1) and (c2)) of laser shots. It can be seen that, in general, the size of the grains enlarges and the periodicity improves as the shot number increases.

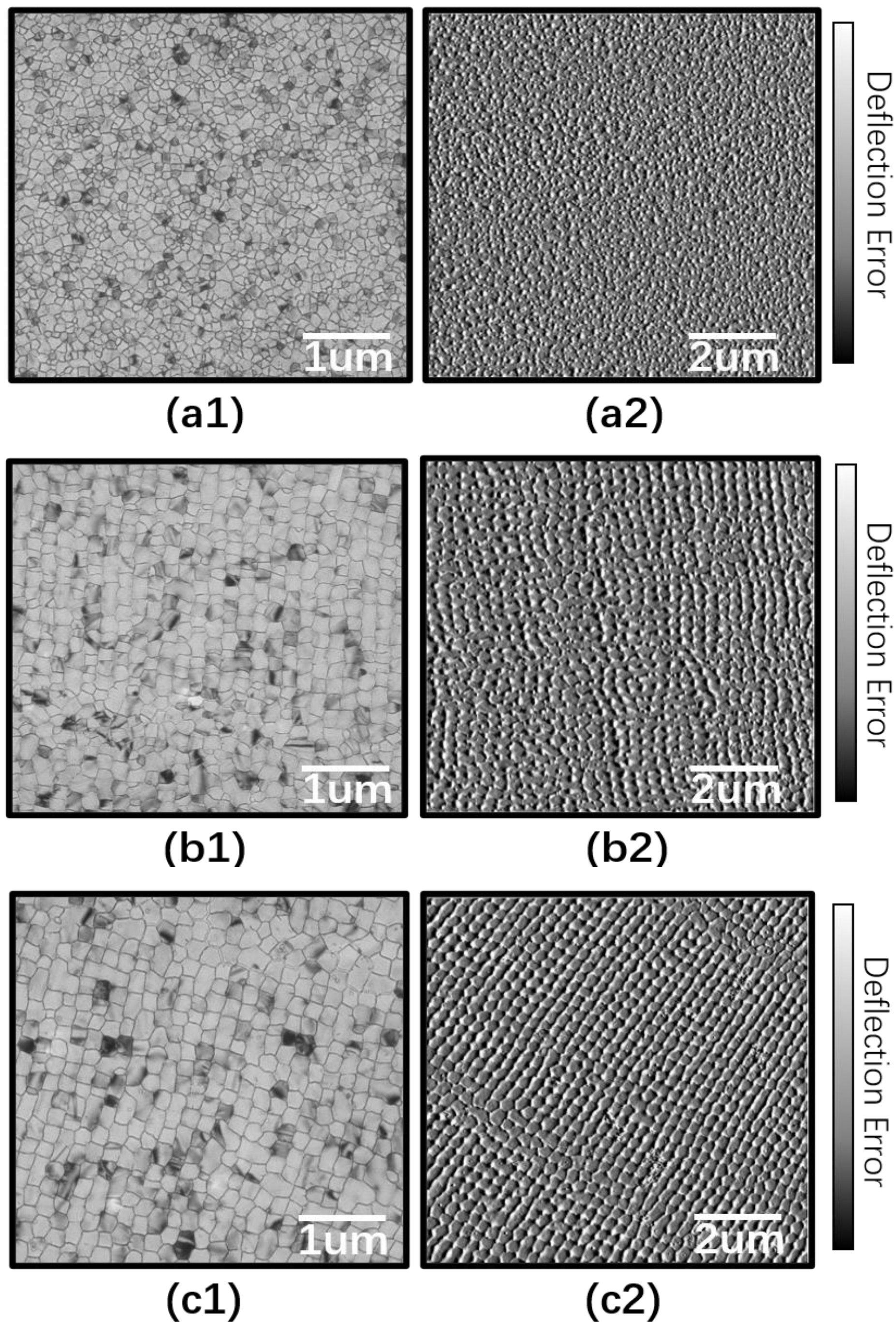

Figure 2.13: (a1) and (a2) the plane-view bright-field TEM image and AFM image of p-Si after a small number of laser shots, (b1) and (b2) the plane-view bright-field TEM image and an AFM image of p-Si after a medium number of laser shots, and (c1) and (c2) the plane-view bright-field TEM image and AFM image of p-Si after a large number of laser shots. The grains generally enlarge and become regular as the shot number increases. The protrusions develop and become more prominent as the shot number increases.

As mentioned before, the microstructure acts as the hub that links the processing parameters, the intrinsic phase transformation and the material properties. More specifically, the microstructure is the result of the ELA process and records valuable information of the phase transformations and determines the material properties. Therefore, studying the microstructure and its evolution benefits both the related scientific society and the technological community by furthering the understanding about the fundamental phase transformations going on under the far-from-equilibrium excimer-laser-induced-melting conditions, as well as providing the understanding about the ELA process and the generated material.

2.3.4 The Influences of Grain Boundaries and Surface Protrusions on the Device Performance

The TFTs fabricated on ELA-generated p-Si thin film are one of the essential elements in the advanced modern displays. Performance of the TFTs largely depends on the electrical properties of the thin film. Unlike in liquid crystal display (LCD), in advanced electronic displays such as active matrix organic light emitting diode (AMOLED) display, TFTs are used not only as switching transistors, but also for the driver circuits to drive large electrical current. Thus, high effective carrier mobility of the p-Si thin film is preferred. The merits of the electrical properties of the ELA-generated p-Si thin film include the high carrier mobility (~200m^2/sV), but the downsides also exist, such as the existence of leakage current between drain and source in the off state, the unstable gate-to-channel capacitance and a considerable decrease of the break-down voltage of the TFTs fabricated with the generated p-Si thin films [66]-[68].All the above four aspects (carrier mobility, leakage current,

stability of gate-to-channel capacitance and break-down voltage) significantly affect the performance and stability of the TFTs. Figure 2.14 shows the structural configurations of an OLED display panel and a typical TFT fabricated on an ELA-generated p-Si thin film. The magnitude of leakage current and the instability of gate-to-channel capacitance are majorly attributed to the grain boundaries that contain a high density of trapping states [66][67], while the decrease of the break-down voltage of the dielectric gate is caused by the abrupt thickness increase at the protrusions, which are formed at the grain boundary locations [68]. Therefore, grain boundaries and surface protrusions are generally identified as the most device-performance-related material characteristics of the ELA films.

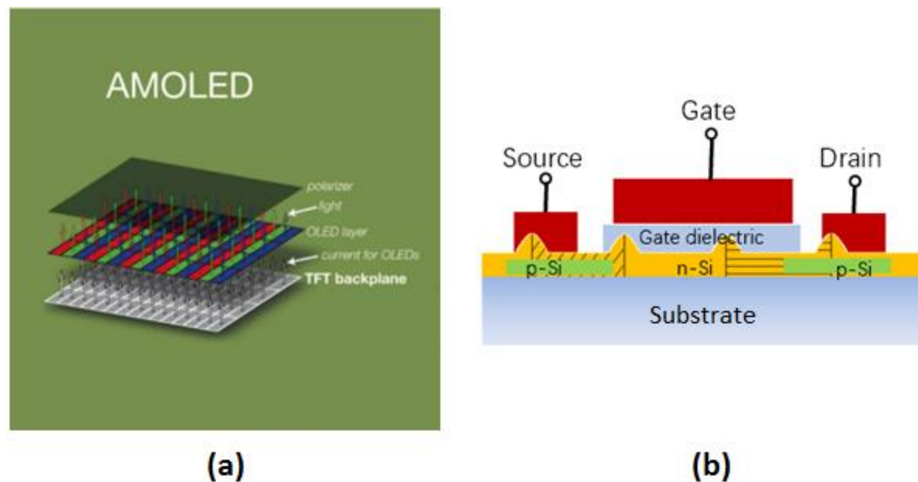

Figure 2.14: (a) A schematic diagram showing the structural configuration of an OLED display panel, where the TFT backplane is fabricated by the ELA process, and (b) a schematic diagram illustrating a typical TFT fabricated on an ELA-generated p-Si thin film. The grain boundaries lower the field-effect carrier mobility and the protrusions (located at the grain boundaries) decrease the effective thickness of the gate dielectric material, which are all detrimental to the performance and stability of TFTs.

2.4 The Microstructure Nonuniformity and the Local Microstructure Analysis

So far the ELA microstructure has been considered as uniform and homogenous over a large length scale, which is supposed to benefit the performance of devices and integrated circuits (ICs) built on the film. However, in reality, the performances of TFTs fabricated at different locations of one film are often found to vary considerably, leading to the awareness of the microstructure nonuniformity within the device scale. In fact, the display manufacturers suffer from performance nonuniformity among different pixels, such as nonuniform brightness and response time, which is primarily attributed to the nonuniform spatial distribution of grain boundary density. This nonuniformity issue is in practice overcome by implementing compensation circuitries. For now, it increases the manufacturing cost acceptably, but is being magnified and would become more difficult to address when the pixel size continuously shrinks as an avoidable result of the ever-increasing display resolution. Performance of small TFTs will get increasingly more sensitive to the nonuniform grain boundary distribution.

In Figure 2.15 and area of relatively uniform-sized and regularly-shaped grains, and areas of nonuniform and irregular-shape grains can be distinguished. The GB densities of these two kinds of areas are different, leading to the different field-effect carrier mobility and density of trapping states, which could eventually result in the inconsistent performances of TFTs fabricated on these two different kinds of areas. For example, the brightness of pixels fabricated on high GB density would be higher than for those fabricated on low GB density locations. This is because the luminance of an OLED pixel primarily depends on the current density, which is significantly

affected by the mobility of the field-effect carriers flowing through it [69][70].

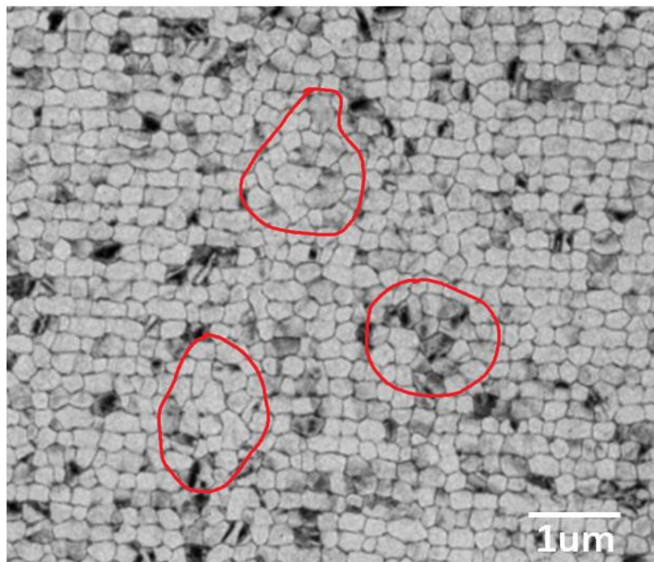

Figure 2.15: The plane-view bright-field TEM image of an ELA-generated p-Si thin film. The grains generally seem to be regular, while the grains in the circled regions look irregular. The microstructure nonuniformity within device scale, such as the area highlighted here, substantially affects the performance consistency among devices fabricated at different locations, which is very detrimental to the ICs and the final products.

In the work of this thesis we approach the abovementioned microstructure nonuniformity and the subsequent inconsistency of the device performance by introducing a scheme for thorough local microstructure analysis (LMA). Figure 2.16 provides three different situations of size distribution of artificial grains to schematically illustrate the importance of the device-geometry and -location dependent analysis regarding the device-performance related microstructure. The average grain size of the three situations in Figure 2.16 is the same and the grains in Figure 2.16 (b) and (c) are exactly identical but with different arrangements. However, it can imagined that (1) devices fabricated on the top left corner of Figure 2.16 (b)

would have the lowest field-effect carrier mobility among all the devices fabricated on the three ‘films’; (2) if we tilt the orientation of a device, the total grain boundaries underneath it would change; (3) if multiple devices are randomly fabricated at different locations on each of the three ‘films’ (Figure 2.16 (a), (b) and (c)), Figure 2.16 (a) must have the best performance consistency, while Figure 2.16(b) must have the worst; (4) the performance consistency of the identical devices fabricated on different locations of the same film must be device size-dependent.

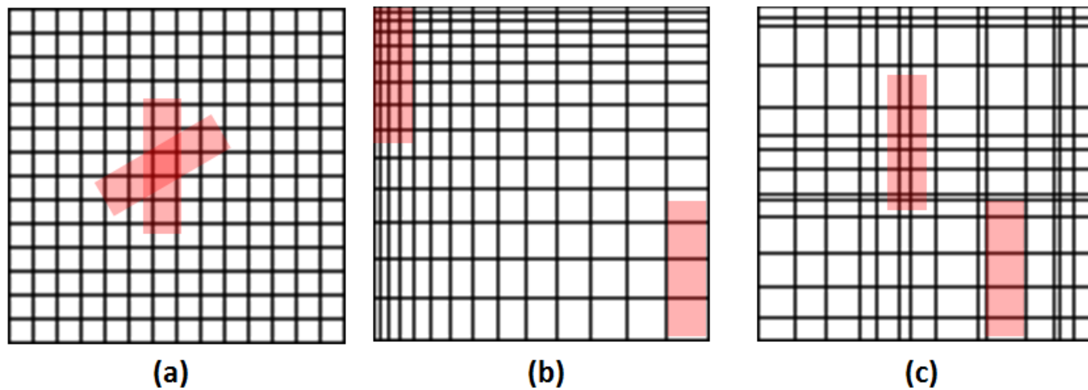

Figure 2.16: (a)-(b) Schematic drawing of three situations of artificial grain distribution, where the average grain size of the three situations is the same and the grains in (b) and (c) are exactly identical but with different arrangements. Each square (or rectangle) represents a grain. The red semi-transparent rectangles represent devices fabricated on the ‘films’. The same device with different orientation or fabricated on different locations would have different total grain boundary length underneath it. The total grain boundary length underneath a device determines the effective carrier mobility of the device, which could result in different device performances. The performance consistency of identical devices fabricated on different locations of one ‘film’ should be different among the three situations, which is determined by the uniformity of the ‘microstructure’ of the three situations.

Based on the above concepts, we propose a local microstructure analysis (LMA) scheme that could simultaneously capture the device-geometry- and device-location- dependent microstructure characteristics as

well as the average grain size. It should be noted that the LMA is performed by analyzing grain boundaries, thus the successful extraction of grain boundaries out of the TEM images is important for realizing LMA. The innovative method we developed to effectively generate GB maps from the TEM images will be presented in the next chapter.

2.5 Motivation and Research Strategy

The microstructure of the ELA-generated p-Si thin films determines the electrical properties of the generated films and hence significantly affects the performance of the final display products, as well as provides copious information for studying the phase transformation involved in such a far-from-equilibrium excimer-laser-induced-melting condition. Due to such technological importance and scientific meaning, the microstructure of ELA-generated p-Si thin films deserve comprehensive and systematic investigation. Improved understanding gained from the investigation would certainly lead to profound implications for both the study of the development of the ELA technology and general polycrystalline materials. That being said, we recognize that both the related scientific society and engineering community can stand to benefit greatly from the work presented in this thesis.

In this thesis, we systematically and comprehensively investigate the device-performance related microstructure of the ELA-generated p-Si thin films. A novel computer-assisted image-processing-based GB extraction program is developed to effectively extract the grain boundaries, in the form of a binary grain boundary map (GB map), out of the TEM images of ELA films. With the GB map, the rigorous LMA scheme is proposed and performed on different ELA samples that are generated using different laser

shot numbers and energies. Characteristics of the ELA microstructure and the microstructural evolution are captured and discussed. The ELA experiments are performed on precursor a-Si thin films of industry-sourced device-grade quality, which ensures the elimination of disturbances such as contamination and residual hydrogen. Unique TEM and sample preparation skills are employed to capture the microstructure of the generated p-Si films over sufficiently large scale with high resolution and low image noise. The surface morphology of the generated films is also studied. The surface morphology of the ELA-generated p-Si thin film is characterized by AFM, where periodic high-aspect-ratio protrusions are identified at the grain junctions. The attempts to planarize the distinct surface protrusions using one shot of excimer laser irradiation are conducted, revealing profound implications about the melting and solidification of the p-Si grains in the ELA process. The surface morphologies before and after planarization are compared by AFM. An in-situ optical probing system is setup to record FTR, BTR and TT signals in nanosecond time resolution in order to depict the spatiotemporal scenario of the melting and solidification process during the planarization experiments. A melting-solidification model is proposed based on the observations of the planarization experiments and numerical simulations are then performed to more comprehensively understand the proposed model. In addition, planarization experiments are also performed on the buffered hydrofluoric acid (BHF) pretreated ELA samples, where a maximum 41.8% of planarization is finally achieved. The different planarization results between as-is ELA sample and BHF-treated sample unveil the influence of the surface oxide layer upon melting, which experimentally demonstrates the theory that melting prefers to happen at the excess-free-energy-rich cites.

The motivation of this work is four-fold: (1) to analyze the ELA

microstructure aspects that are closely related to the device performance and improve the understanding of the microstructure, (2) to develop a sensible scheme and an effective approach for the analysis, which is achieved by the LMA scheme associated with the image-processing based GB extraction program, (3) to reduce the detrimental surface protrusions, and (4) to gain insights of the fundamental phase transformation of p-Si thin films under the special far-from-equilibrium excimer-laser-induced-melting condition of ELA via the systematic analyses of the microstructure and planarization experiments with one excimer laser shot. It should be specially noted that the scheme and skill developed for the microstructure analysis in this thesis can be generalized to other research fields of material science, especially where polycrystals and particles are involved.

Chapter 3

An Image-processing-based Method for the Grain Boundary Extraction

As explained in the last chapter, the device performance fabricated on ELA films is substantially affected by the presence of the dense grain boundaries. In this chapter, we present the development of an image-processing-based method which enables precise and efficient extraction of grain boundaries (GB) from the TEM image of the ELA microstructure. The necessity of the GB extraction and the related difficulties are firstly identified. Then our approach to the image processing problem is described. Unlike traditional approaches for edge detection in images, our program is based on the Watershed Segmentation method [71][72]. Programing details such as definition, algorithm and pseudocode are presented. Going further this program will be referred to as the GB extraction program. The GB maps are successfully extracted with excellent precision using the program. It should be emphasized that without precise and efficient GB extraction it would be

extremely difficult to realize comprehensive and systematic ELA microstructure analysis, which simultaneously considers the spatial characteristics, the device-size and -location dependent characteristics and a statistically significant number of grains. This GB extraction program can also be applied in other material research fields, especially where the geometry and arrangement of grains or particles are of concern.

3.1 Necessity and Difficulties in the GB Extraction

The local microstructure analysis (LMA) scheme requires sufficiently large area and statistically meaningful grain number of the ELA microstructure. Recall from the previous chapter that the typical size of a TFT fabricated on an ELA-generated film is several tens of micrometers square in size and, in the ELA process, each movement of the scanning excimer-laser beam is around 20µm. Thus, an area of at least several hundreds of micrometers square is required to capture microstructure non-uniformities. Figure 3.1 is a TEM image of the ELA microstructure captured using our unique TEM and sample preparation skill, which captures an area of 33µm in length and 23µm in width and contains thousands of grains. In the image, the grain bodies are generally brighter and grains boundaries are relatively darker. The rare dark grain body coloring is attributed to the internal stress that leads to the local density change of the grains.

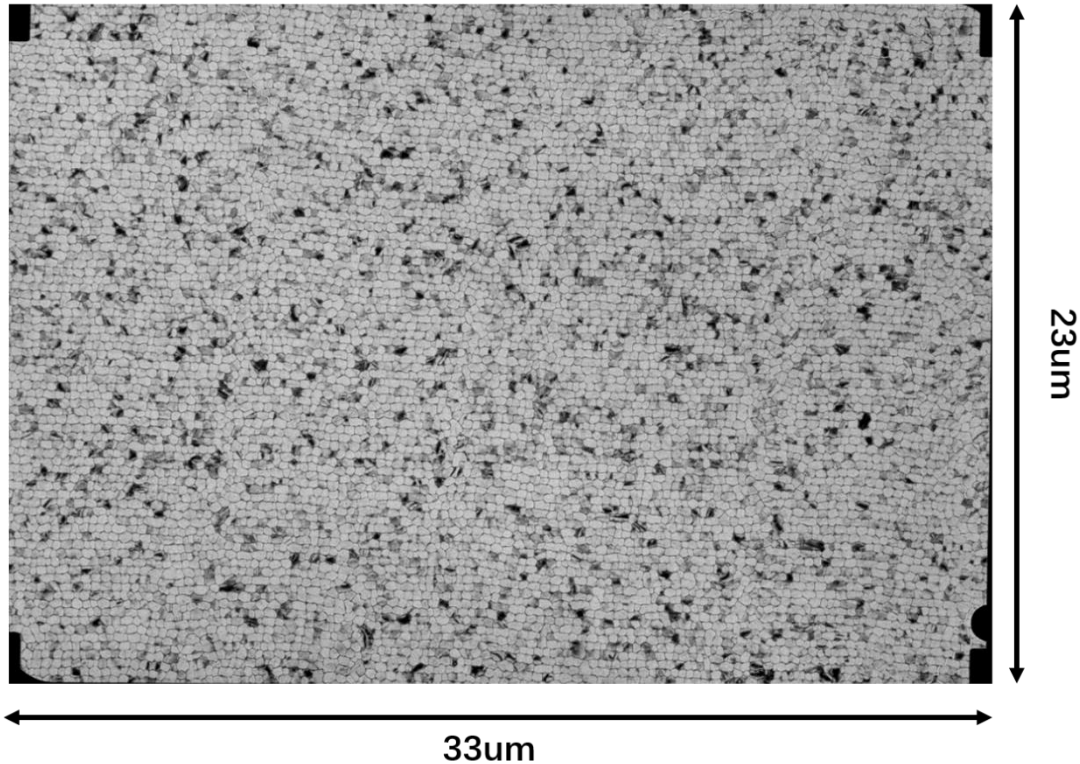

Figure 3. 1: Plane-view bright-field TEM image (33μm × 23μm) of the ELA microstructure. Around 9,000 grains are captured in the image, which is a statistically meaningful number for the quantitative analysis of the microstructure. In the previous study of the ELA p-Si, at most a few hundred of grains could be captured, which was not sensible to perform the thorough analysis this thesis is aiming for.

It would be strikingly inefficient to manually analyze thousands of grains, which is in fact what researchers previously did to a much smaller area consisting of at most several hundred grains [57]-[59]. Thus, a computer-assisted method is adopted. As the LMA is based on the extraction of grain boundaries, it is fundamental to let a computer program understand how to distinguish grain bodies and grain boundaries. As long as the grain boundaries are precisely extracted, the implementation of LMA would become more straightforward. Even though the grain bodies and boundaries in the TEM

image can be easily distinguished by a human eye, it is not as straightforward for a computer program. For example, simply partitioning the image based on contrast would cause the anomalously dark grains to be counted as grain boundaries. In fact, this task has extended into a specific technological field called image segmentation [73]. Therefore, the fundamental difficulty regarding the GB extraction is identified as enabling a computer program to precisely distinguish the grain boundaries versus grain bodies.

3.2 The Implementation of the Watershed Segmentation in the GB Extraction

A pixel is the smallest addressable and controllable element in a digital image. The entire image can be thought of as a digital grid (i.e. a matrix), where each site represents a pixel with an associated pixel index value determining its position. Pixel color in our greyscale image case is simply captured by a single numerical value (referred to as pixel value) determining the intensity (i.e. brightness) of the pixel. Precisely distinguishing the grain boundaries from bodies using a computer program requires a specific category of image-processing techniques called image segmentation. Among various commonly used image segmentation approaches, such as edge-detection-based segmentation, threshold method, region-based segmentation and cluster-based segmentation, the Watershed Segmentation based on mathematical morphology is identified as the most suitable method for our case. This is because (1) our TEM image is in greyscale; (2) the image contains a high density of boundaries; (3) the brightness contrast between grain bodies and grain boundaries is not sharp; (4) a TEM image normally contains significant noise and disturbance, causing trouble for traditional

image processing approaches [74]-[76]. The noise and disturbance are unavoidable due to the working principle of TEMs and the nature of materials which can be either distinguishable (such as the uncommon dark grain bodies) or indistinguishable (such as the pixel-level noise) by a human eye.

3.2.1 The Idea of the Watershed Segmentation

The pixel values of a TEM image, which is set to be 8-bit and in greyscale, vary from 0 to 255 where 0 means the lowest brightness (i.e. black) and 255 means the highest brightness (i.e. white), while the values between 0 and 255 mean grey. Figure 3.2 is one example illustrating the relationship between the pixel value and the brightness in display.

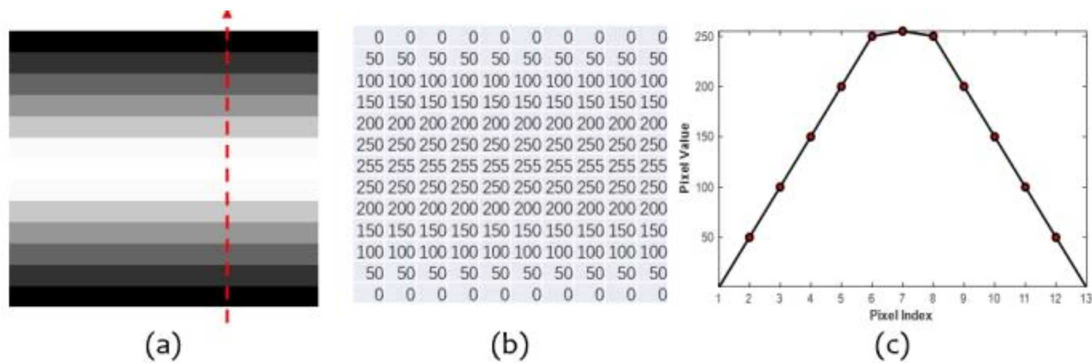

Figure 3. 2: A brief illustration of how a computer displays a greyscale image. Figure (a) is an image in greyscale which displays the matrix (b) with values ranging from 0 to 255. 0 displays in black (darkest) and 255 displays in white (brightest). (c) A diagram showing the value versus pixel location along the vertical red dash line in (a).

The idea of the Watershed Segmentation can be intuitively and graphically described as follows. A greyscale image can be considered as a topographic relief, where the address and the value of each pixel respectively represent the location and the altitude of each local point of the relief. Then,

we imagine continuously adding water onto the relief to gradually submerge the terrain. Water falls down and gathers at the low-altitude locations, forming lakes. The water level would continuously elevate with the addition of water, and the adjacent lakes would finally meet each other. According to the definitions in the Watershed Segmentation, the lakes and the meeting locations of the adjacent lakes are respectively referred to as the *catchment basins* and the *watersheds*, and the above described process is called the *immersion process* [77]. Figure 3.3 schematically shows the above description, where it can be understood that this method should be theoretically good at distinguishing the local contrast, which is exactly required in our case, since there is a plenty of disturbances in the global scale of the TEM images.

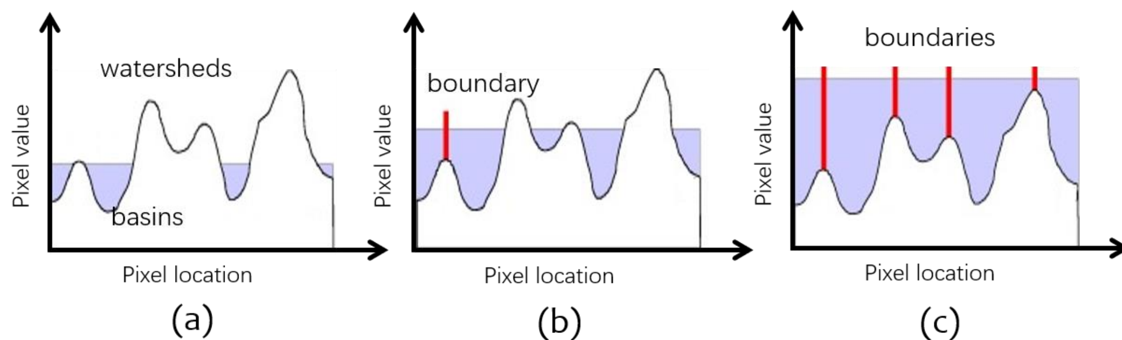

Figure 3. 3: (a) - (c) Schematic diagrams illustrating the conceptual description of the *immersion process* in the Watershed Segmentation. In the *immersion process*, water level, elevates monotonically from the lowest altitude (i.e. pixels with the smallest value) to the highest altitude (i.e. pixels with the largest value). The basins are then gradually filled with water and the water in the adjacent basins will finally meet as the water level elevates. The watersheds are then defined at the water-meeting location of adjacent basins.

In order to let a computer program distinguish between catchment

basins and watersheds, we first need to precisely describe the characteristics of catchment basins and watersheds. The characteristics of basins are captured as (1) each individual basin has its sole lowest-altitude region (referred to as '*local minima*', which consist of one or a set of pixels with the regionally minimum pixel value) and (2) the altitude monotonically increases from the *local minima* outward until the watershed is reached [77]. The watershed is defined as the exact location where adjacent basins meet together. Then, based on the above characteristics, the pixels can be naturally sorted into three different classes, namely (1) the pixels belonging to the *local minima*, (2) the pixels belonging to the basins but not the *local minima* of the basins and (3) pixels belonging to the watersheds. Following the above classification in mind, all pixels can be categorized into the three classes in a sequence from low altitude to high altitude in the *immersion process*. Figure 3.4 schematically illustrates the three classes of pixels and the *immersion process*.

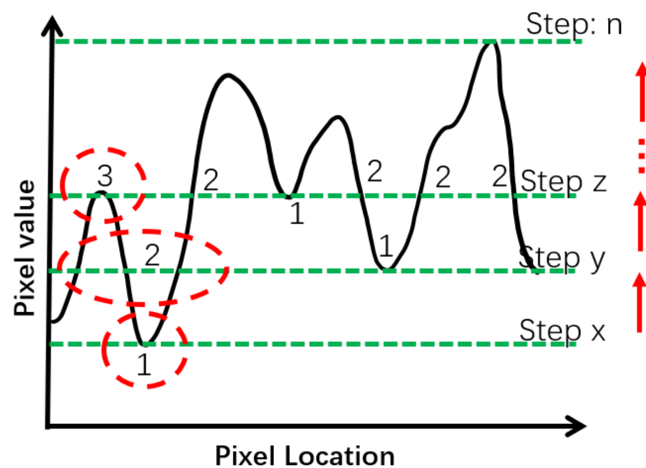

Figure 3.4: Schematic diagram illustrating the three classes that all the pixels need to be sorted into in the *immersion process* in order to let a computer identify basins and watersheds. Pixels belonging to *local minima* of a basin (green and black line intersections labeled by 1), to a basin but not the *local minima* (intersections labeled by 2), and to watersheds (labeled by 3) are presented. The horizontal green dash lines represent different

steps of the *immersion process*.

3.2.2 Theoretical Framework and Definitions

The idea intuitively and graphically described in the above subsection points out two major considerations when we design the program. On one hand, the program is supposed to start with the evaluation of the lowest altitude region (i.e. pixels with smallest value) and then monotonically move to the higher altitude regions (i.e. pixels with larger values). On the other hand, we need to set a quantitative criterion in order to determine which of the three classes a pixel belongs to, as well as to distinguish which pixels belong to which basins or watersheds. The first aspect can be realized by a commonly used method called *FIFO* (first-in-first-out) [78], the implementation of which will be described in the next subsection. The quantitative criterion can be realized by a mathematical-morphology dilation process via identifying the *geodesic influence zones* (*i*Z) of the *local minima* and the boundaries of the influence zones (referred to as *Skeleton by Influence Zones* (*SKIZ*)) [77].

A digital image can be written as a function denoting $I = (P, f(p))$ (Equation 3.1), where I represents a digital image, P represents the pixel set consisting of all the pixels in the image, p denotes an individual pixel and $f(p)$ is the pixel value of pixel p. The minimum path length between two pixels or from a pixel to a subset of P is defined as the *geodesic distance*. The *geodesic distance* from pixel p_i to pixel p_j which is denoted as $d(p_i, p_j)$ and the *geodesic distance* from one pixel p_i to a subset P_j within P which is denoted as $d(p_i, P_j)$ and defined as the minimum path length

among all the path lengths from the pixel p_i to any of the pixel p_j belonging to the subset P_j. This is schematically shown in Figure 3.5 (a) and defined as:

$$d(p_i, P_j)= MIN_{p_j \in P_j}(d(p_i, p_j)) \tag{3.2}$$

Let P be partitioned into k connected subsets P_i, $i = 1,2, \dots, k$, then the *geodesic influence zone* of the subset P_i within P, as schematically shown in Figure 3.5 (b), is defined as:

$$iz_P(P_i) = \{ p \in P | \forall j \in [1..k] \backslash \{i\}: d_P(p, P_i) < d_D(p, P_j)\} \tag{3.3}$$

Then the *skeleton by influence zones* of P is defined as:

$$SKIZ\ P = P / \sum iz_P(P_i) \tag{3.4}$$

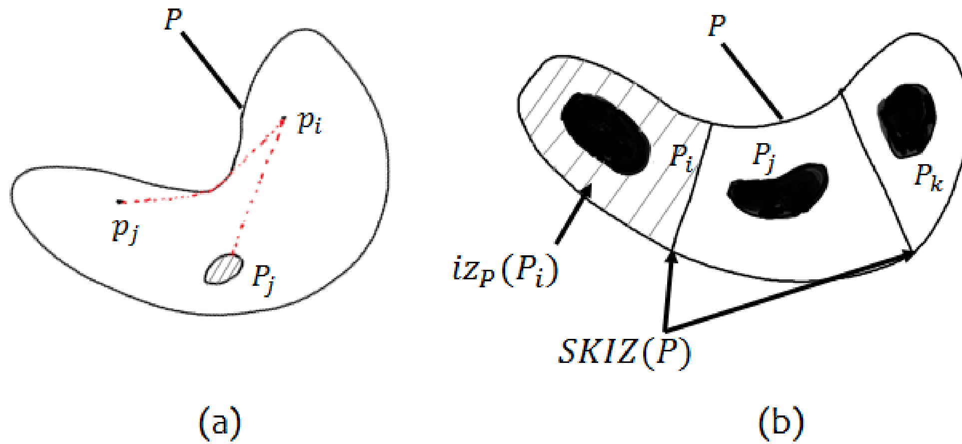

Figure 3.5: (a) Schematic diagram illustrating the geodesic distance between two pixels (p_i and p_j) and the *geodesic distance* between a pixel (p_i) and a subset （P_j） of pixels with in a pixel set *P*, and (b) schematic diagram illustrating the *influence zone* (hatched area) of a pixel subset P_i and the *skeleton by influence zones* (*SKIZ*) between P_i and P_j as well as

between P_j and P_k.

The water level described in the above subsection refers to all the pixels at the same altitude (say the altitude at value h) and can be defined as:

$$T_h = \{\, p \in P \mid f(p) \leq h \} \tag{3.5}$$

Based on the idea of the Watershed Segmentation, the three classifications of the pixels and the above definitions, the *immersion process,* which is the core of the Watershed method, can be formulated as a recursion:

$$\begin{cases} X_{h_{min}} = \{\, p \in P | f(p) = h_{min} \} = T_{h_{min}} \\ X_{h+1} = MIN_{h+1} \cup IZ_{T_{h+1}}(X_h),\ h \in [h_{min}, h_{max}) \end{cases} \tag{3.6}$$

The watershed Wshed (f):

$$\text{Wshed}\,(f) = P \backslash X_{h_{max}} \tag{3.7}$$

where X_h denotes the union of the set of basins computed at altitude h. Figure 3.6 is an example of computing the above recursion.

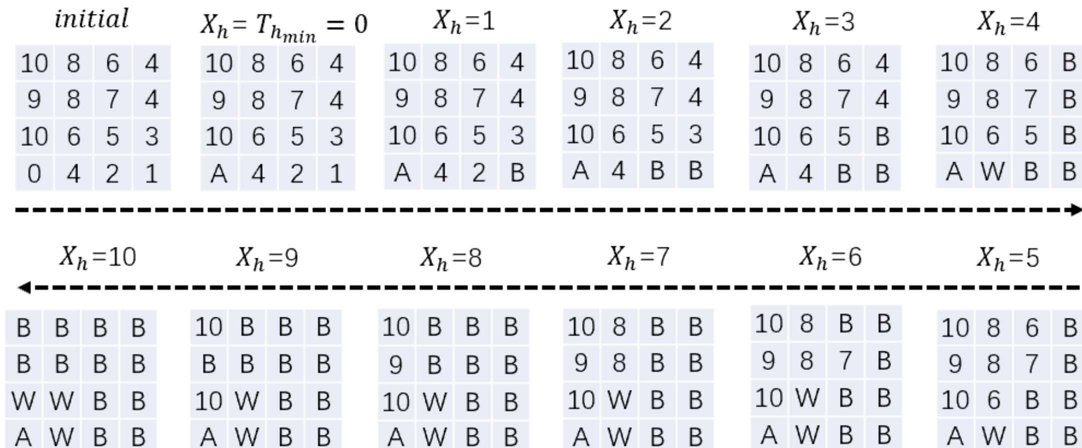

Figure 3.6: An example of computing the above recursion (the immersion process), where the numbers are the initial pixel values, the letters (A and B) represent two different basins and W represents watersheds.

3.2.3 The Algorithm

The algorithm is the implementation of the Watershed Segmentation theory, the mathematical definition of the criterion for categorizing the pixels and the formulation of the *immersion process*. In practice, we sequentially inspect each pixel and categorize it into one of the three classes. The inspection of the pixels is enabled by a dynamical labeling process, in which each pixel is first pre-labeled according to its status (such as "being inspected in the current loop", "already classified" or "has not yet been classified") and the labels of its neighbor pixels, and are then finally labeled according to its category. The dynamic labeling process is presented in the following content. The inspection also needs to consider two other aspects of one pixel which are (1) its pixel value and (2) the pixel index. In the algorithm, we define pixelvalue[p] meaning an operation to take the pixel value of pixel p (brightness) and outpixel[p] is an operation to take the label of pixel p. The algorithm is described as follows.

(1) In one loop, we one-by-one inspect all the pixels at the same altitude (i.e. all the pixels with the same pixel value);

(2) Sort all the pixels according to their value from the lowest to the highest and store them in a *FIFO* queue;

(3) Label each pixel according to its status and the labels of its neighbor pixels (top/left/right/bottom);

  a. Define two labels according to the status of a pixel, which are respectively outpixel[p]=1 meaning that the pixel value is above the

being-inspected altitude or the pixel won't be inspected in the current loop, and outpixel[p]=2 meaning that the pixel value is at the being-inspected altitude and the pixel will be inspected in the current loop;

b. Define two labels according to the three different classes, which are respectively outpixel[p]=n with ($n \geq 10$) meaning that the pixel belongs to a basin (each basin has its identical label) and outpixel[p]=0 meaning that the pixel belongs to a watershed;

c. Define one label according to the labels of the neighbor pixels, which is outpixel[p]=3 meaning that the being-inspected pixel has at least one neighbor pixel with outpixel[*neighbor*]≥10 or =0;

(4) Rules for categorizing;

a. If there exists a neighbor with outpixel[*neighbor*] ≥10 (say *A*) & the outpixel[*neighbor*] of the other neighbors are either the identical number *A* or 0 then the being-inspected pixel *p* is labeled as: outpixel[*p*]=*A*, meaning to merge into the same catchment basin. Note that any neighbor with outpixel[*neighbor*]=1, 2 or 3 does not affect judgement. All the situations that are separated by the grey lines are listed as below:

```
          A
        A 3 A
          A
-------------------------------------------------
      A         A
    A 3 0     A 3 ?        ? Denotes either 1 , 2 or 3
      A         A
-------------------------------------------------
  A      A      A       A      A      A
0 3 0  0 3 ?  ? 3 ?   A 3 0  A 3 0  A 3 ?
  A      A      A       0      ?      ?
-------------------------------------------------
          A
        0 3 0
          0
```

b. If there exists more than one neighbor with different outpixel[*neighbor*]

≥10 (say *A*, *B* or *C*), then the being-inspected pixel *p* is labeled as: outpixel[*p*]=0. Note that any neighbor with outpixel[*neighbor*]=1, 2 or 3 does not affect judgement. All the situations that are separated by the grey lines are listed below:

```
  A       A       A       A       A       A
B 3 0   B 3 0   B 3 ?   0 3 0   ? 3 0   ? 3 ?
  0       ?       ?       B       B       B
-------------------------------------------------------------
  A       A       A       A
B 3 0   B 3 ?   B 3 A   B 3 A        ? Denotes either 1 , 2 or 3
  A       A       0       ?
-------------------------------------------------------------
  A       A       A       A       A
B 3 A   B 3 A   B 3 A   B 3 B   B 3 C
  A       B       C       A       A
```

c. If there does not exist any neighbor with outpixel[neighbor] ≥10 & exists at least one neighbor with outpixel[*neighbor*] =0, then the being-inspected pixel *p* is labeled as: outpixel[*p*]=0. Note that any neighbor with outpixel[*neighbor*]=1, 2 or 3 does not affect judgement. All the situations that are separated by the grey lines are enumerative as below:

```
          0
        ? 3 ?
          ?
-------------------------------------------------------------
    0       0
  0 3 ?   ? 3 ?          ? Denotes either 1 , 2 or 3
    ?       0
-------------------------------------------------------------
          0
        0 3 0
          ?
```

d. If outpixel[*p*]=2 and there exists at least one neighbor with outpixel[*neighbor*]=3 & there does not exist any neighbor with outpixel[*neighbor*]=0 or ≥10, then change outpixel[*p*] of the being-inspected pixel *p* from 2 to 3. Note that any neighbor with

outpixel[*neighbor*]=1, 2 or 3 does not affect judgement. All the situations are enumerative as below:

```
   3           3           3           3           3
?  2  ?     3  2  ?     ?  2  ?     3  2  3     3  2  3
   ?           ?           3           ?           3
```

? Denotes either 1 or 2

(5) At last the remaining sets of pixels with outpixel[*neighbor*] = 2 are identified as the minima of different and new catchment basins and each of the pixel sets is labeled with an unique outpixel[] that has never been used yet to label any other pixel(s). One example is shown below, where the two sets of isolated pixels at the being-inspected altitude are identified as the two new *local minima* of two different basins.

```
   2 2                   D D          |  2 2 2               E E E
2  2 2 2              D  D D D        |  2 2 2 2             E E E E
2  2 2 2 2     =>     D  D D D D      |  2 2 2 2 2    =>     E E E E E
   2 2 2 2               D D D D      |  2 2 2 2 2           E E E E E
     2 2                   D D        |
```

3.2.4 The Pseudocode

The details of the program are presented in Appendix A and the pseudocode is as below:

/*define variables*/

final WSHED 0

final INIT 1

final MASK 2

int pixelvalue[x*y]

```
float outpixels[x*y]
connectivity = 4
current_label = 10
boolean stop = false
boolean flag = false
minLevel = 0
maxLevel = 255
init_fifo_queue(queue)

initialize outpixel[] for all pixels to be 1
```

/*inspect pixels from lowest pixelvalue[] to highest pixelvalue[]*/

```
Sort the pixelvalues for all pixels and store in a queue
for all item in outpixels
    item = INIT
end for
```

```
gray = pixelvalue[0]

for l = minLevel to maxLevel
```

/* Label the pixels at the altitude that will be inspected in the current loop to be 2 and label the pixels which pixels are adjacent to a grain or watershed (the being influenced pixels) to be 3 */

```
    for all p in D with grayleval(p) = gray
        outpixels[p] = MASK
        if p has neighbour q with (outpixels[q] > 4 or outpixels[q] = WSHED)
            outpixels[p] = 3.0
            fifo_add(queue, p)
        end if
    end for
```

/*First inspect all the being-influenced pixels*/

```
while(!isEmpty(queue))
    p = fifo_remove(queue)
    central = outpixels[p]
    for neighbour in p.neighbours with order(top, left, right, bottom)
        if outpixels[neighbour] > 9.0
            if central == 3.0
                outpixels[p] = outpixels[neighbour]
                central = outpixels[neighbour]
            else if central == 0.0 && flag
                outpixels[p] = outpixels[neighbour]
                central = outpixels[neighbour]
            else if central > 9.0 && central != outpixels[neighbour]
                outpixels[p] = WSHED
                central = 0.0
                flag = false
            end if
        else if outpixels[neighbour] == 0.0
            if central == 3.0
                outpixels[p] = WSHED
                central = 0.0
                flag = true
            end if
        else if outpixels[neighbour] == MASK
            outpixels[neighbour] = 3.0
            if topNeighbour(p) == neighbour
                outpixels[top(p)] = 3.0
                fifo_add(queue, top(p))
            else if leftNeighbour(p) == neighbour
                outpixels[left(p)] = 3.0
                fifo_add(queue, left(p))
            else if rightNeighbour(p) == neighbour
                outpixels[right(p)] = 3.0
                fifo_add(queue, right(p))
            else if bottomNeighbour(p) == neighbour
```

```
                outpixels[bottom(p)] = 3.0
                fifo_add(queue, bottom[p])
            end if
        end if
    end for
end while
```

/*Second process all the isolated groups of pixels (the minima of new catchment basin*/

```
for all p in D with (grayleval(p) = gray && !stop)
    if outpixels[p] == MASK
        ++current_label
        stop = (current_label > 1000000.0f)
        fifo_add(queue, p)
        outpixels[p] = current_label
        while(!isEmpty(queue) && !stop)
            pp = fifo_remove(queue)
            for neighbour in pp.neighbours with order(top, left, right, bottom)
                if outpixels[neighbour] == MASK
                    if topNeighbour(pp) == neighbour
                        fifo_add(queue, top(pp))
                    else if leftNeighbour(pp) == neighbour
                        fifo_add(queue, left(pp))
                    else if rightNeighbour(pp) == neighbour
                        fifo_add(queue, right(pp))
                    else if bottomNeighbour(pp) == neighbour
                        fifo_add(queue, bottom[pp])
                    end if
                    outpixels[neighbour] = outpixels[pp] = current_label
                end if
            end for
        end while
    end if
    if gray >= maxLevel
```

```
            stop = true
        end if
    end for
    gray = next graylevel in pixelvalue[]
end for
```

3.3 The Results

The interim outputs when running our program are shown in Figure 3.7 in order to present the way that the program works. It can be seen that the program starts by inspecting and labeling the pixels at the lowest altitude of the entire image. Then the inspected and labeled region starts to expand like lifting up the water level, constituting the *immersion process*. In the meantime, new *local minima* are detected following the new expansions starting from the new *local minima*. Gradually, all the basins (grain bodies) are identified, followed by the recognition of the watersheds (grain boundaries) at the meeting locations of the nearby basins. At last, a binary image as shown in Figure 3.7(h) is generated from the TEM image shown in Figure 3.7(a) using our program.

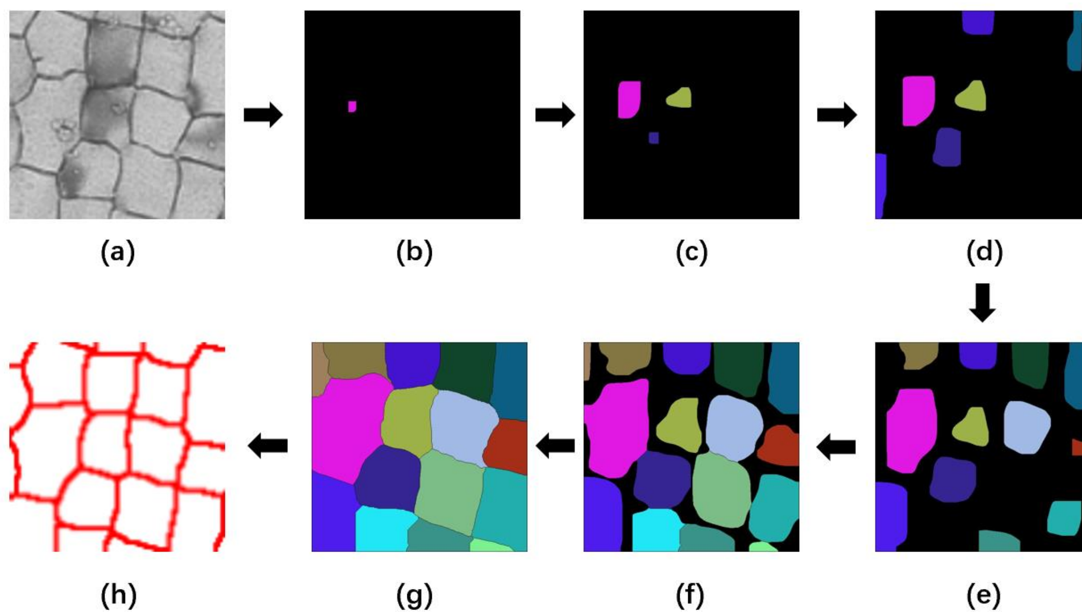

Figure 3. 7: (a) A cropped plane-view bright-field TEM image of an ELA-generated p-Si thin film, which is the input of our grain boundary segmentation program (GB segmentation program), (b) the beginning of the program when one *local minimum* at the lowest altitude of the entire image is identified, (c)-(f) interim outputs when running the program, (g) the end of the program when all the pixels are classified and all the basins and watersheds are identified, and (h) the final result, which is the generation of the binary grain boundary map (GB map).

The final result after running our program is a binary GB map, where all the grain boundaries are in red (i.e. all the pixels at the grain boundaries have the same value) and all the grain bodies are in white (i.e. all the pixels in the grain bodies have the same value), based on which LMA of ELA microstructure can be realized. Figure 3.8 shows the result of the GB map converted from an entire TEM image of ELA microstructure. The TEM image covers the area more than 600μm^2 and contains thousands of grains. It can be seen that our program is very effective and precise in identifying and extracting the grain boundaries.

It should be pointed out that preprocessing and postprocessing should also be applied before and after running our program in order to eliminate the rare, prominent and hard to overcome noise and disturbances that existed in the TEM image. In the pre process filtering, contrast tuning, thresholding and blurring are used. In the post process, some incorrectly generated watersheds (about 5%) have to be manually corrected.

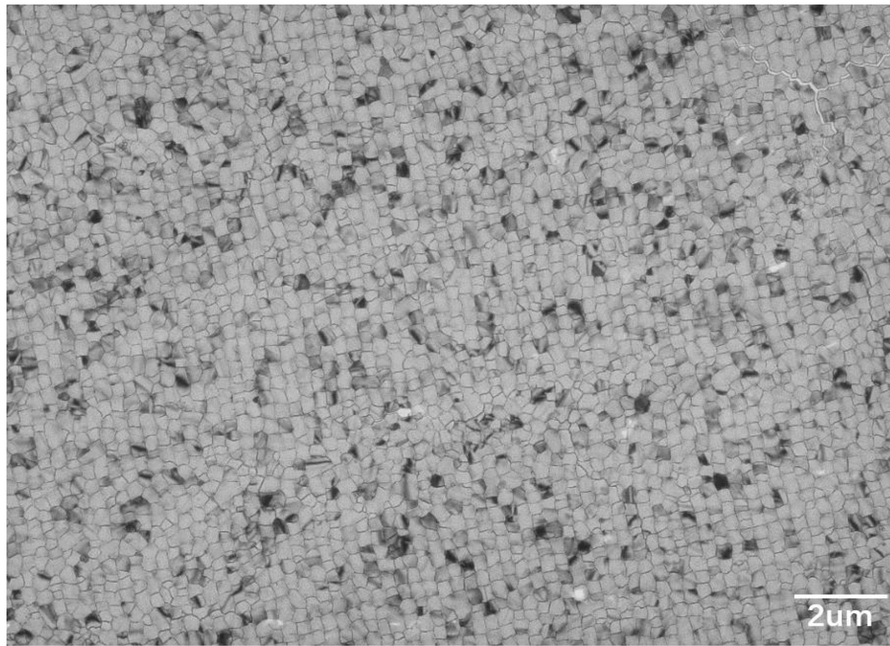

(a)

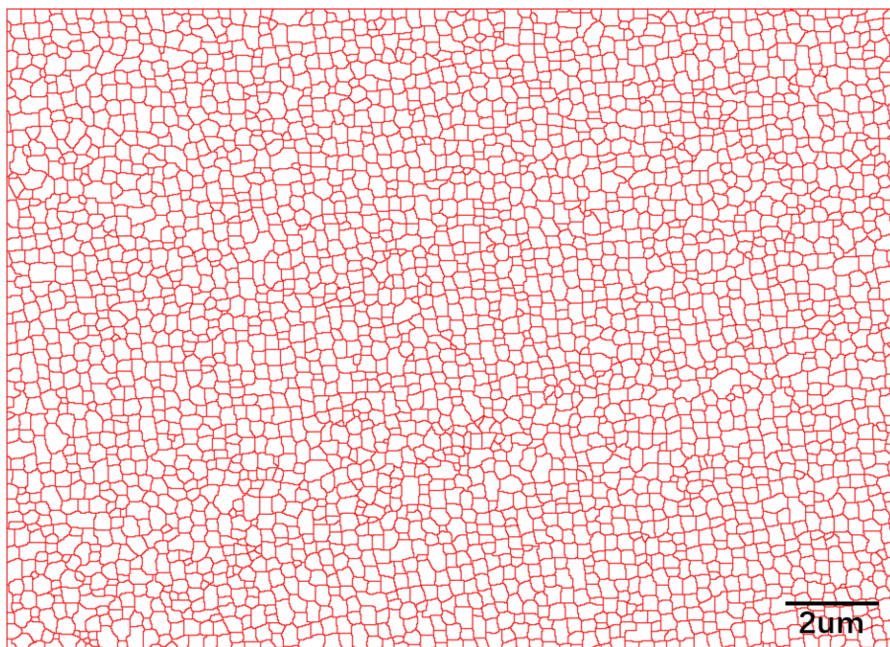

(b)

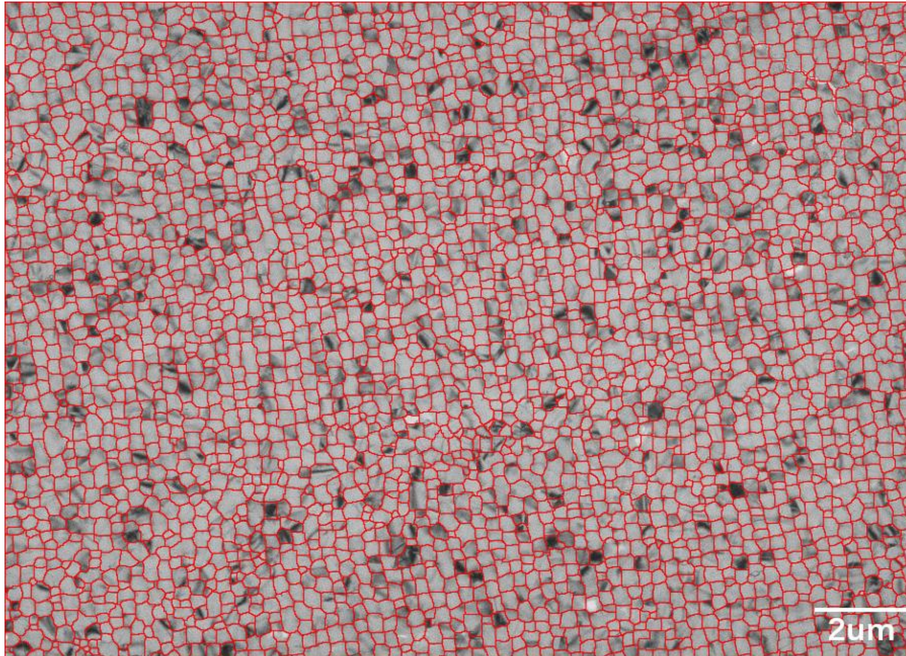

(c)

Figure 3.8: (a) A plane-view bright-field TEM image of the microstructure of the ELA-generated p-Si thin film; (b) the GB map converted from the TEM image (a); (c) the overlapped image of the TEM image (a) and the GB map (b) which verifies the accuracy of our GB segmentation program.

3.4 Summary

The LMA requires an area of at least several hundreds of micrometers square for the reason that the typical size of a TFT is around several tens of micrometers square and the scan step of the excimer laser beam in the ELA process is around 20µm. The major difficulty to perform LMA lies in the precise and efficient GB extraction.

The idea and the implementation including mathematical definition, formulation and the algorithm of the Watershed Segmentation are presented in detail. We subsequently develop a GB extraction program which has been proven to be effective and accurate in distinguishing grain boundaries from

grain bodies, leading to the successful generation of binary GB maps from the TEM images. The value of this work can be recognized as it is the successful GB extraction and the generated GB map that allows realizing the LMA of the ELA microstructure, which would be otherwise extremely difficult to perform manually.

It is worth pointing out that the Watershed Segmentation method is not limited to TEM images and grain boundary extraction. AFM and SEM images of the ELA microstructure can also serve as the input. More generally, the Watershed Segmentation method can be extended to process other aspects of the microstructure, like sub-grain boundaries and dislocations, as long as the contrast between bodies and boundaries of interest is sufficient.

Chapter 4

The Local Microstructure Analysis (LMA)

In this chapter, we present a systematic microstructure analysis of the ELA-generated p-Si thin film by taking the advantage of the GB extraction program and the LMA scheme. The grain-size analysis of a statistically significant number of grains is presented, the results of which intriguingly deviate from the commonly observed log-normal distribution of the grains in general polycrystalline materials. The spatial characteristics of the microstructure based on the geometry and the arrangement of the grains are quantified. Such analyses constitute the most systematic and comprehensive investigation of the device-performance related microstructure to date. The results, which provide engineers and researchers quantitative data and description to better understand the microstructure of the material, the related properties and the phase transformation, contribute to both the related technological community and the scientific society.

4.1 Grain Size Statistics

We have pointed out in the last chapter that in order to perform a statistically sensible quantitative analysis, the number of grains should be at least several thousand. The TEM image of the ELA-generated p-Si, as shown in Figure 4.1(a) satisfies the requirement of grain number. The GB map generated from the TEM image using our GB extraction program is shown in Figure 4.1(b). Based on the GB map, we conduct the statistical analysis of the grain size and the result is shown in Figure 4.1(c). The distribution resembles a normal distribution with a mean value of 191.787nm and standard deviation of 51.528nm, but an anomalous peak can be found at around 250nm. Here we point out that such grain-size distribution is unusual, since the researchers commonly observe a log-normal distribution of grain size in polycrystalline materials due to the stochastic nature of the grain formation [79]-[81].

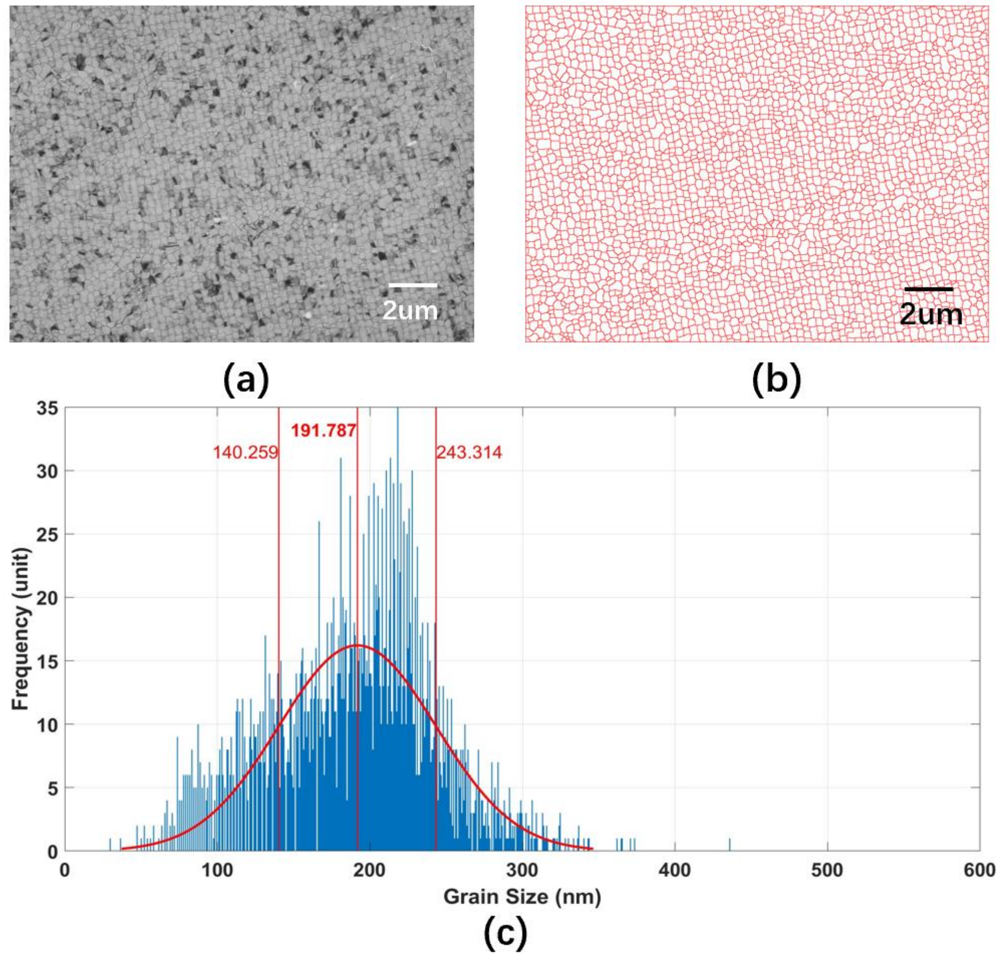

Figure 4.1: (a) The plane-view bright-field TEM image of the ELA microstructure, (b) the binary GB map generated from the TEM image (a) using our program, and (c) the statistical grain-size distribution and the normal distribution fitted curve. The grain size deviates from the commonly observed log-normal distribution characteristic of stochastic grain formation process.

4.2 Spatial Analysis of the Microstructure

The spatial analysis quantitatively reveals the local variations of the ELA microstructure aspects related to the device performance. In this section, three aspects of the spatial microstructure analysis are presented, which are respectively (1) the LMA-GB density analysis, (2) the LMA-orientation analysis and (3) periodicity analysis. Such analyses have been long desired by

the engineers but haven't been quantitatively performed in the past.

4.2.1 The LMA-GB Density Analysis

The display industry, where ELA p-Si thin film is used for the TFT backplane, suffers from location-dependent performance nonuniformity of TFTs. To overcome such nonuniformity compensation circuitries must be used, additionally increasing the manufacturing cost. If we zoom in and look at the details of the grains in the TEM image (Figure 4.1 (a)) of the ELA-generated p-Si thin film, it can be intuitively seen that some regions consist of relatively smaller grains and some regions consist of relatively larger grains, and most of the regions consist of 'regular' grains. Smaller grains lead to higher local GB density, while larger grains lead to lower GB density. We already introduced in the above chapters that the leakage current and the decrease of the field-effect carrier mobility, which degrade the device performance, are linked to the grain boundary density. Therefore, it can be understood that the TFTs fabricated on the boundary-rich region may not perform as well as those fabricated on the low GB density region. We define the GB density and the relative GB density as:

$$\sigma = \frac{L_{total}}{A_{trans}} \text{ and } \alpha = \frac{\sigma}{\sigma_{aver}} \tag{4.1}$$

where σ, L_{total}, and A_{trans} are respectively the GB density, the total length of the grain boundary underneath a transistor and the size of the transistor, and α and σ_{aver} are respectively the relative GB density and the average GB density over the entire film.

In the LMA-GB density analysis, a probing circle with chosen diameter

is used to represent a TFT, which pixel by pixel scans over the entire GB map. During the scan the pixel indices of the scanning circle and the associated α underneath the circle are recorded and calculated at each pixel of the GB map. In the end, a heat map can be generated using such data by representing the recorded α values with different color that ranges from blue (the minimum α) to red (the maximum α). We call such heat map to be the GB density heat map. It can be understood that the GB density analysis is thus device-size dependent. Figure 4.2 (c) is one GB density heat map calculated from the GB map (shown in Figure 4.1 (b)), assuming the circle diameter to be 2µm. Hot (or reddish) regions with higher relative density and cold (or blueish) regions with lower relative density can be identified. The difference of relative GB density between the hottest and coldest regions reaches as high as around 25%. The sizes of the hot and cold regions are of the same order as the TFTs used in the current ELA display. Therefore, we can understand that the performance consistency of TFTs has to be detrimentally affected by the microstructure nonuniformity.

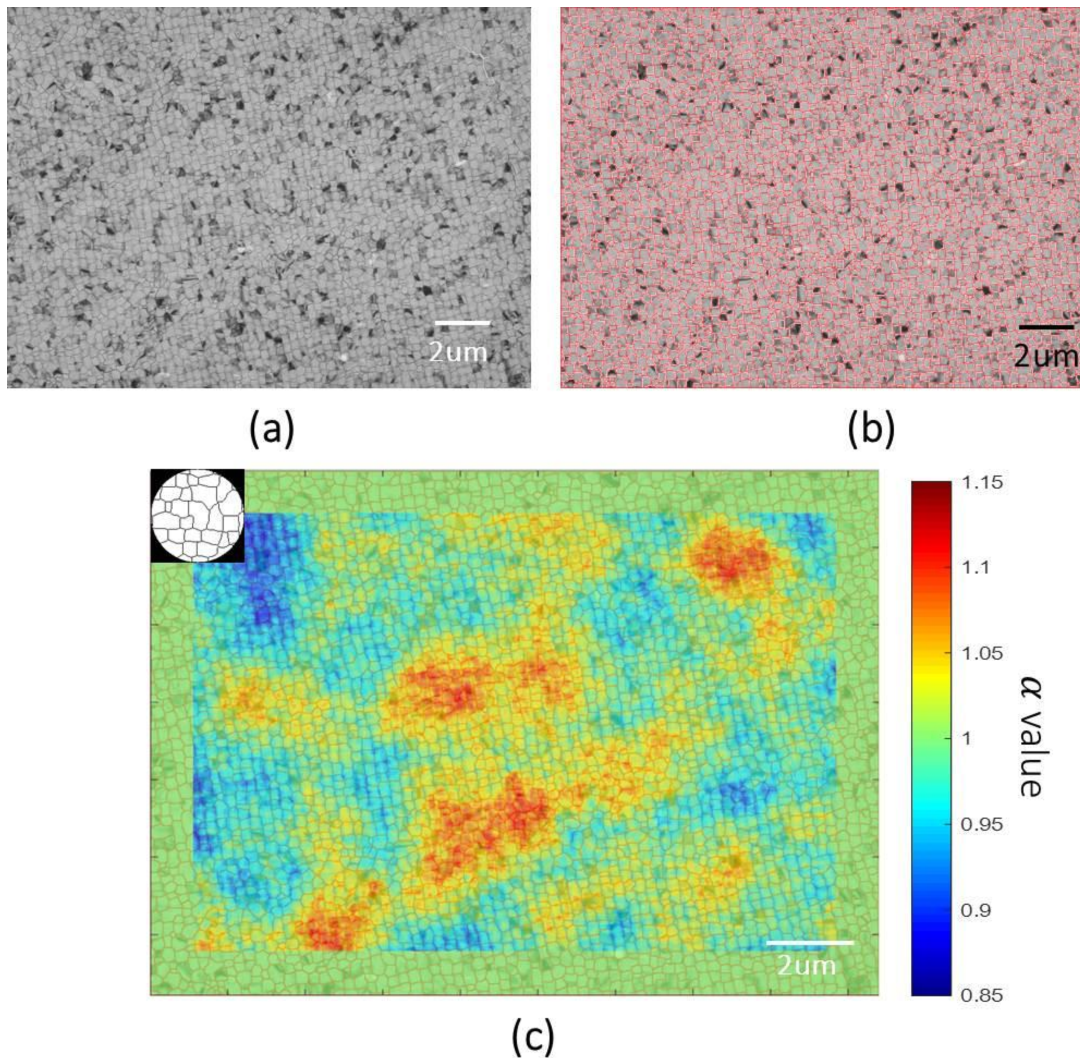

Figure 4.2: (a) The TEM image of the microstructure of an ELA-generated p-Si, (b) the overlapped image of the GB map and the original TEM image, and (c) the overlapped image of the TEM image, the GB map and the GB density heat map, where hot (reddish) regions indicate higher GB density while the cold (bluish) regions indicate lower defect density. The inset on the top-left corner of figure (c) is the scanning circle, with 2μm in diameter, used to generate the heat map. The pixel indices of the scanning circle and the associated relative grain boundary (α) underneath the circle are recorded and calculated at each pixel of the GB map. The green frame (equal in thickness to the TFT probe radius) around the image is caused by setting the default α=1 where the probe would partially lie outside the GB map.

In manufacturing, it is found that TFTs with large size perform more consistently than those with small size. Here, we take probing circles of different diameter to sweep over the identical GB map (Figure 4.1 (b)) and generate corresponding GB density heat maps. The results are shown in Figure 4.3, where the diameter of the probing circles are respectively assumed to be 0.5μm (Figure 4.3 (a)), 1μm (Figure 4.3 (b)) and 2μm (Figure 4.3 (c)) for each sweep. Figure 4.3 (d) shows the curve-fitted statistical diagrams of α values under the three diameter situations, where the blue, orange and yellow curves respectively correspond to 0.5μm, 1μm and 2μm probing circle diameter. From both the color fluctuation in the heat map and the distribution profile of the fitted curves, it can be seen that the local nonuniformity dramatically magnifies as the TFT size shrinks. Since the total length of grain boundaries underneath a TFT primarily determines the field-effect carrier mobility, it can be understood that larger local nonuniformity of the GB density must considerably lead to the more inconsistent device performance. Therefore, as we shrink the TFT size following the pursuit of the ever-increasing display resolution, we expect that the nonuniformity of TFT performance caused by the local nonuniformity of GB density would become more and more severe.

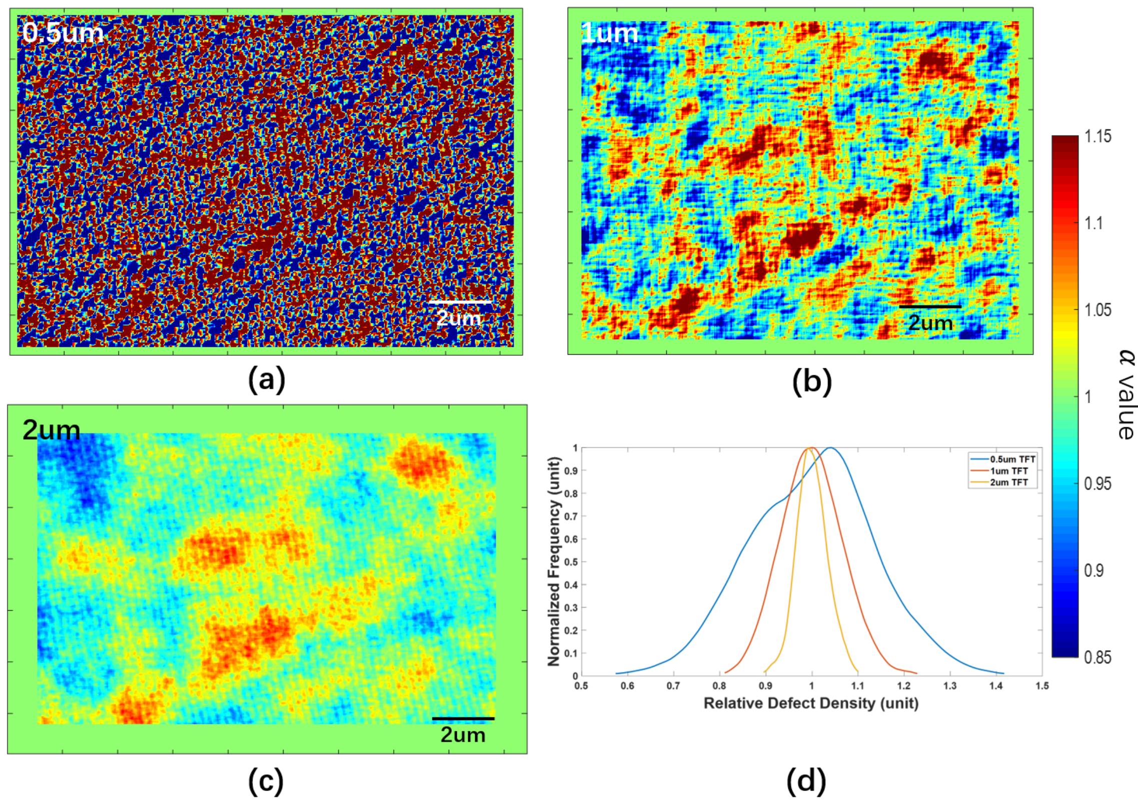

Figure 4. 3: (a)-(c) GB density heat maps respectively corresponding to 0.5μm, 1μm and 2μm probing circles, where reddish color means high GB density (consisting of relatively smaller grains) while blueish color means low GB density (consisting of relatively larger grains), and (d) the curve-fitted statistic diagrams of the α values under the three situations, where the blue, orange and yellow curves respectively correspond to 0.5μm, 1μm and 2μm diameter situations. The broad distribution profile of the blue curve indicates the large local nonuniformity of the GB density. The width of green-color (meaning the α value to be 1) area on the edge equals to half of the diameter of the probing circles. The insets on the top left corner are the diameters of the probing transistors (circles).

4.2.2 The LMA-Orientation Analysis

In the advanced display such as AMOLED, TFTs are used to drive large electrical current in a pixel, which is different from those used in the traditional LCD displays, where TFTs only serve as switching transistors that require much smaller current. Therefore, higher carrier mobility of the ELA-

generated p-Si thin film is preferred. On the other hand, the inconsistency of device performance as a result of local nonuniformity of field-effect carrier mobility is always desired to be minimized. Carrier mobility in the case of an ELA film primarily depends on the total grain boundary length within the channel area of a TFT (i.e. roughly, the more grain boundaries within the channel area of a transistor, the lower the field-effect carrier mobility). Keeping in mind the characteristic square-like geometry of the ELA grains, we suppose that there may exist certain transistor orientation that optimizes the field-effect carrier mobility in the channel area (i.e. either achieve higher average field-effect carrier mobility over the entire film or improve the local uniformity of the field-effect carrier mobility, or both). The LMA-orientation analysis is adopted, which is defined in the similar way as the LMA-GB density analysis. The difference between the two analyses is that in the LMA-orientation analysis a probing oval instead of a circle is used. The major and minor axes are set to be 3μm and 1μm, and the angle between the major axis and the horizon is set from 0° to 165° with an increase of 15° for each trial. The analysis results of different orientations are selectively shown in Figure 4.4. Figure 4.4 (c) gives the optimal orientation (135° with respect to horizon) and the corresponding statistical histogram (Figure (c2)) of the α values is relatively narrow and sharp with the standard deviation of 9.26%. Meanwhile, Figure 4.4 (b) gives the worst orientation (75° with respect to horizon) and the corresponding statistical histogram (Figure (b2)) of the α values is relatively broad with the standard deviation of 11.61%. The orientation (75° with respect to horizon) shown in Figure 4.4 (a) yields moderate uniformity with the standard deviation of 9.90%. This analysis indicates that devices would very likely perform more consistently if we align the devices along the direction following Figure (c1).

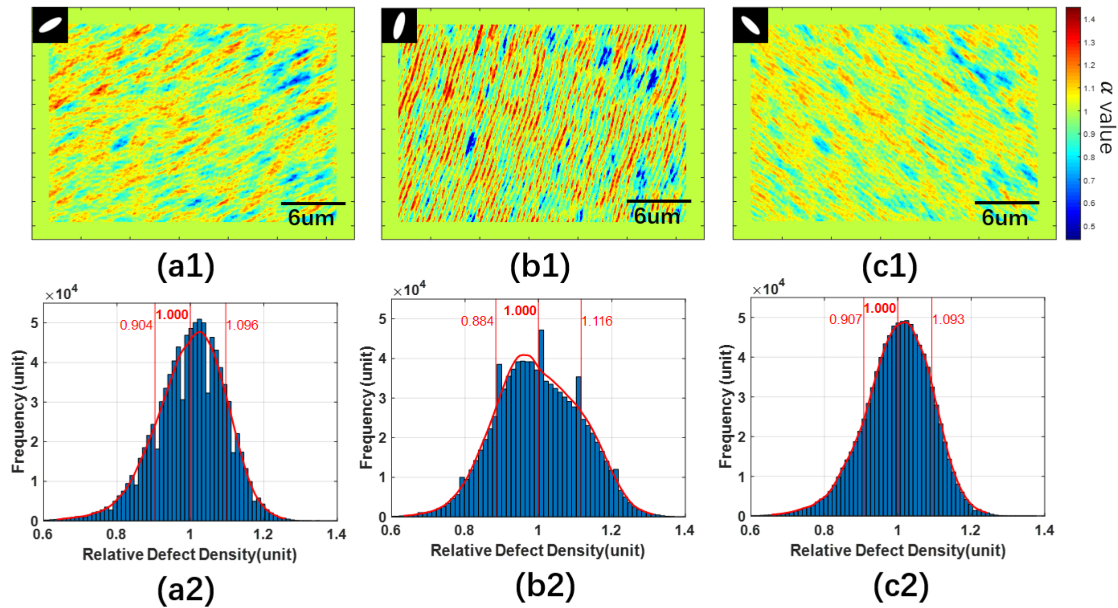

Figure 4. 4: (a1)-(c1) The GB density heat maps when the major axes of the testing oval are respectively at the angle of 30°, 75° and 135° with respect to the horizon, and (a2)-(c2) the corresponding statistical histograms of the α values respectively corresponding to (a1)-(c1). The insets on the top-left corner of figure (a1)-(c1) are the 3µm×1µm probing ovals. 135° gives the best local uniformity (with the standard deviation of 9.26%) of GB density, while 75° gives the worst (with the standard deviation of 11.61%).

4.2.3 Periodicity Detection

The industry-grade ELA-generated p-Si thin film always exhibits some periodicity of the grain distribution. It is generally accepted that higher periodicity means better quality of the film and thus better product performance. This is similar to what grain size statistics do, but here we focus on distinguishing more periodic regions from the less periodic. For some ELA samples, the periodicity may not be very clear and can only be intuitively identified by experienced engineers. The binary GB map enables digital recognition of the periodicity, from which the extent of periodicity can be easily quantified using a factor that we name as ‘area fraction of periodicity’.

Fast Fourier Transform (FFT) is applied to the binary GM map shown in Figure 4.5 (a) and a diffraction image is generated shown in Figure 4.5 (b). The background signal and noise are filtered by a thresholding function using the software called ImageJ, producing the image of Figure 4.5 (c). In Figure 4.5 (c) diffraction patterns are observed which clearly indicate the existence of periodicity. Inversed FFT (IFFT) is then performed to Figure 4.5 (c) and the resulting image highlights the periodically distributed grain boundaries. From the IFFT image (Figure 4.5 (c)), the area percentage of the periodic regions over the entire area is calculated to be 48.94%, which can be used to quantitatively describe the extent of periodicity that we define as 'area fraction of periodicity' (γ). This analysis will be implemented and discussed further in Chapter 5.

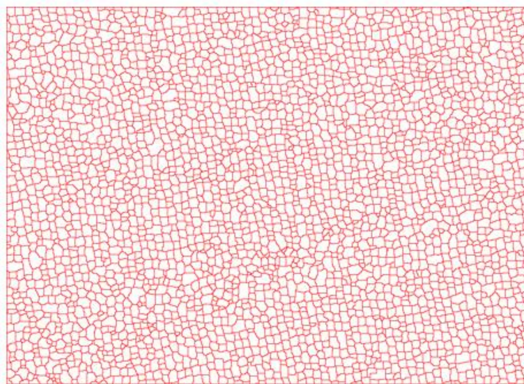

(a)

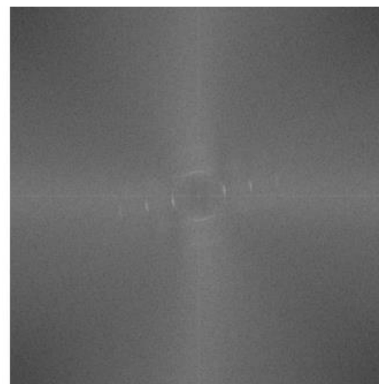

(b)

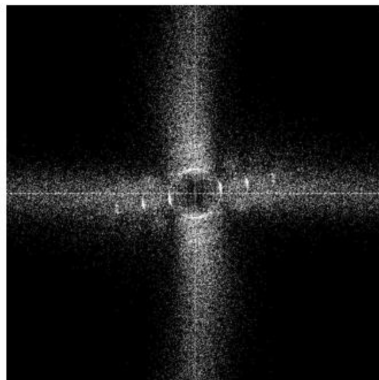

(c)

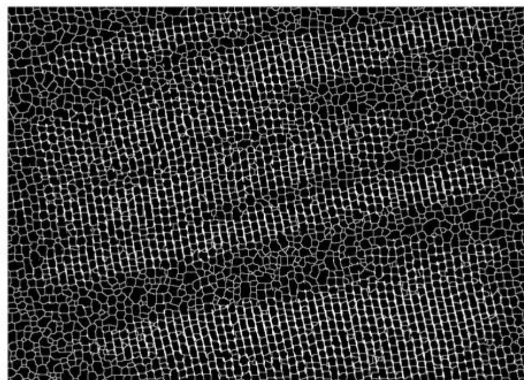

(d)

Figure 4. 5: (a) The binary GB map generated from the TEM image of the ELA-generated p-Si thin film, (b) the FFT diffraction pattern obtained from the GB map, (c) the filtered FFT image after diminishing the background signal and noise, and (d) the inversed FFT image transformed from (c). The previously qualitatively observed periodic regions in the ELA microstructure are now visually enhanced and quantitatively identifiable.

4.3 Discussion

The grain size of several thousand grains is statistically analyzed. It can be seen from Figure 4.1 (c) that the size of the grains ranges from about 50nm (very small grains) up to about 350nm (very large grains). The numbers of very small grains and very large grains are marginal and most of the grains lie in the range from 140nm to 241nm. The statistical distribution of the grain size deviates from the normally observed log-normal distribution. This result tells us some of the characteristics of the ELA-generated p-Si thin film, namely that (1) the p-Si thin film is relatively uniform from the statistical point of view, (2) very small grains and very large grains coexist with the grains of the 'regular' size, and (3) the grain distribution is not log-normal, indicating that the grain formation process is not purely stochastic. The first two characteristics capture the statistics of grain size distribution of a significant number of ELA grains. The third characteristic stands as an evidence, from the grain-size statistics point of view, of the light-diffraction phenomenon that is believed to influence the ELA grain formation during laser irradiation. The light diffraction effect of the ELA microstructure has been recognized and the subsequent laser energy redistribution was theoretically studied in the previous literature [23][41]. Figure 4.6 shows strong evidence of the existence of light diffraction in the ELA film, which was reported by *Van der Wilt et al* [21].

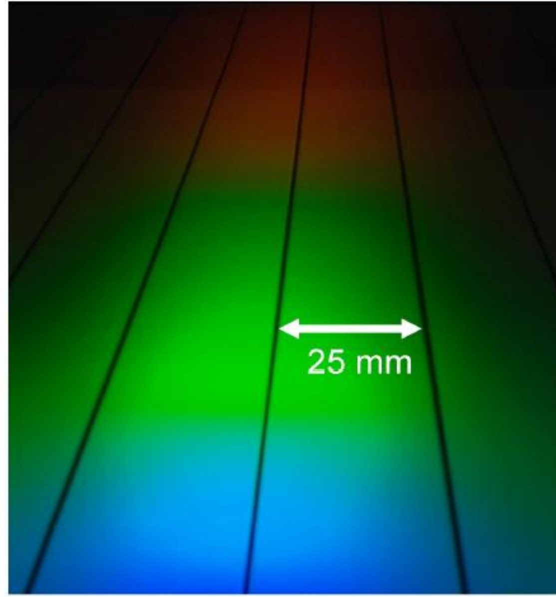

Figure 4. 6: A flash photograph of the surface of an ELA-generated panel under oblique angle. The different colors at different angles of view evidence the existence of light diffraction [21].

The spatial microstructure analysis is performed based on the GB map. From the LMA-GB density analysis, we observe that (1) small, large and 'regular' grains are not uniformly distributed, resulting in the local nonuniformity of α values on the device length scale and (2) the local nonuniformity magnifies dramatically as the size of the probing transistors shrinks. The former observation for the first time discloses the long-term qualitatively recognized but never quantitatively captured nonuniformity issue. Even though the microstructure appears uniform from just considering the grain size statistics, there is local nonuniformity in the device scale which would definitely considerably contribute to the inconsistency of the device performance fabricated at different locations. We can predict from the second observation that the display industry would suffer more from the performance inconsistency of the devices as the pixel size is getting smaller. From the LMA-orientation analysis, we demonstrate that there are preferred

orientations, where the local uniformity of the α values can be optimized, leading to potential improvement of the inconsistent device performance issue. Furthermore, the periodicity of ELA microstructure is digitally detected using the GB map. By applying FFT, signal filtering and inversed FFT, the area fraction of periodicity (γ) is calculated to be 57.18%. The γ can be potentially adopted to quantitatively define the extent of the periodicity of the ELA microstructure, which could help engineers assess the quality of the generated p-Si films.

4.4 Summary

In this chapter, we demonstrate the statistical grain-size analysis and the spatial analysis of the microstructure over a statistically significant grain number and a sufficiently large area by taking the advantage of the GB map and the LMA scheme. The LMA scheme and the quantitative definitions presented in this chapter could benefit the related research field, especially for the engineering community to better understand the ELA process, the generated material and the product performance.

Chapter 5

The ELA Experiments and Comprehensive Microstructure Analysis

As introduced in the section 2.3.3 (The Microstructure and Surface Morphology of ELA Si Thin Films), excimer-laser annealing is a sequential partial-melting-based method. Each of the tens of laser pulses incident upon the same area causes a melting and resolidification cycle, leading to a gradual microstructure evolution. The novel image-processing based GB extraction program developed in chapter 3 and the rigorous local microstructure analysis (LMA) demonstrated in chapter 4 can now be applied at various intermediate stages of ELA to study the fundamental grain evolution mechanisms and to improve the process understanding for engineers. Such analysis has been so far hindered by (1) the incapability to capture high quality images of sufficiently large areas of the film, (2) the lack of high-quality samples and (3) the unavailability of effective approaches to perform the analysis, such as our GB extraction program and LMA tools.

This chapter describes our ELA experiments with 5 to 30 shots incident upon industry-grade a-Si thin film samples. Our method of acquiring high-quality Transmission Electron Microscopy (TEM) images of large thin film areas is presented. The TEM images of microstructure generated from different shot numbers are processed using our program to extract the GB maps and perform LMA. Then the evolution of the microstructure and the related implications are discussed. The findings of this work could provide abundant information for studying the phase transformation in the ELA process as well as for understanding the ELA technique and the generated material, which will benefit both the related scientific society and the technological community.

5.1 ELA Experiments

5.1.1 Experimental Plan

We irradiate different precursor a-Si thin films of identical sample configuration using 5 shots, 10 shots, 15 shots, 20 shots, 25 shots and 30 shots. The adopted laser is xenon-chloride gas excimer laser with wavelength of 308nm and pulse duration of 30ns at full-width-half-maximum (FWHM). The time interval between shots is around 200ms, so the irradiated area can completely cool after each melting and resolidification cycle. The laser spot size in the sample is 1mm × 1mm, so most of the irradiated area would not be thermally affected by the unirradiated region. The experiments are done under room temperature and regular atmosphere environment. After finishing the ELA experiments, the processed thin films are subject to TEM

characterization. At last, we systematically analyze and compare the microstructures of the films processed with different shot numbers.

5.1.2 Sample Configuration of the precursor a-Si

The unprocessed samples are industry-grade a-Si thin films deposited on glass substrates. The a-Si layer is deposited using plasma-enhanced chemical vapor deposition (PECVD) equipment that ensures high quality and avoids the formation of microcrystal clusters and contamination. The thickness of the a-Si film is around 50nm and the total thickness of the sample after adding the glass substrate is around 4mm. The deposited a-Si film is dehydrogenated to avoid the hydrogen residue that could disturb the intrinsic phase transformation properties of the material. The generated a-Si thin film has a thin oxide layer at the top surface and an atomically flat Si/oxide interface at the bottom.

5.1.3 Experiment Setup

The system used for the ELA experiments is shown in Figure 5.1. An excimer laser generates pulses with the wavelength of 308nm and pulse duration of 30ns at FWHM in a xenon-chloride gas chamber. An attenuator is used to finely tune the energy density of the laser beam, which is then monitored using a calibrated pyroelectric energy meter. After the attenuator the laser beam is shaped when passing through an array of optics including telescope, homogenizer, field and projection lenses, and is output with a relatively uniform spatial intensity profile with the size of 1mm×1mm. A

computer-controlled sub-micron-precision translation stage is used to bring the sample surface to the focus point of the laser beam.

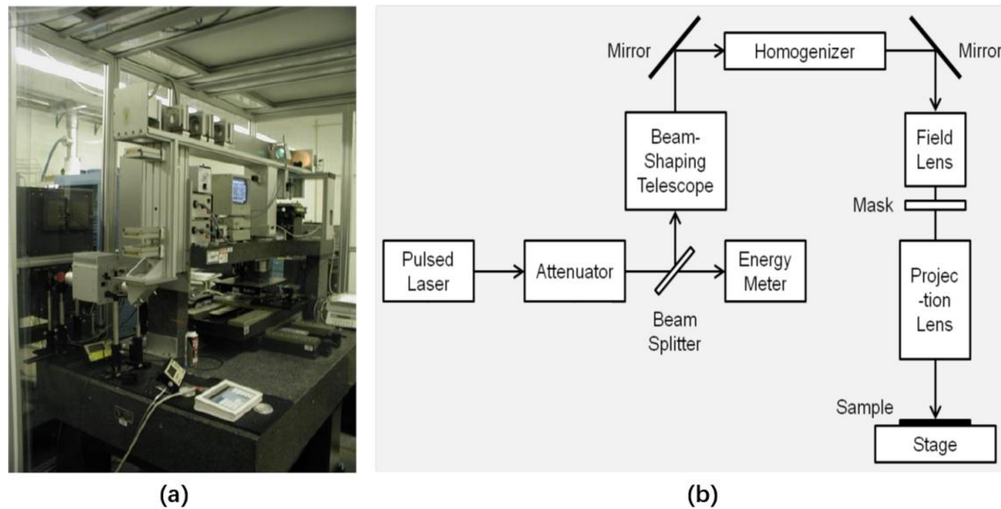

Figure 5. 1: (a) Laser system setup for the ELA experiments and (b) the optical layout schematic of the beam delivery system.

5.2 Grain Imaging by Transmission Electron Microscope

Previous chapters have pointed out that for successful microstructure characterization several TEM image requirements must be satisfied, namely (1) sufficiently large area, (2) high image contrast between grain bodies and boundaries and (3) low image noise. The aged TEM model JEOL 100CX shown in Figure 5.2 (a) better satisfies our requirements than the more recent models. The necessary image pixilation in modern digital TEM cameras causes a high number of anomalously bright spots, which are not easily removed during our image processing. The major reason that JEOL 100CX is more suitable for us is its compatibility with electron microscopy photo films shown in Figure 5.2 (c). The imaging here relies on the fluorescence-sensitive emulsion coating that undergoes a chemical change when struck by the scattered electrons. The merit of electron microscopy films is their natural

tendency to average out the abrupt bright spots in the fluorescence, yielding smooth brightness gradients in the captured image. Additionally, our technique of using TEM photo films and later digitizing the image in a high-quality scanner yields images of higher resolution than it is possible to obtain directly from TEM digital cameras.

When operating the TEM, we use a trick to slightly defocus the electron beam from the film surface in order to increase the contrast between the grain bodies and the grain boundaries, taking the advantage of the fact that there exists a thickness difference between the grain bodies and the grain boundaries. Before capturing the image of the microstructure, the TEM sample is prepared by a lift-off technique as follows. The ELA-generated samples are first immersed into buffered hydrofluoric acid (BHF) to remove the oxide layer on the top surface of the p-Si film. Then a Secco etchant, which can effectively etch the defects in Si material, is used to gently etch through some of the grain boundaries. Then a droplet of hydrofluoric acid (HF) is placed onto the surface of the film and kept for several minutes to let HF leak into the bottom Si/oxide interface through the etched grain boundaries in order to separate the Si film from the glass substrate. At last, we hold the sample horizontally and slowly immerse it in water. The separated Si film is then lifted off and floats on the surface of the water. Then we can transfer the lifted film onto a TEM grid shown in Figure 5.2 (b). It should be pointed out that the controlled grain-boundary etching is an essential step without which the grain boundary would not be as clearly revealed in the TEM image. An example of properly grain-boundary etched area versus inappropriate etched area is shown in the TEM image of figure 5.2 (d). The areas with properly removed oxide and etched grain boundaries show very distinct grains, while the insufficiently etched areas appear cloudy and would not yield an effective

GB extraction.

(a)

(b)

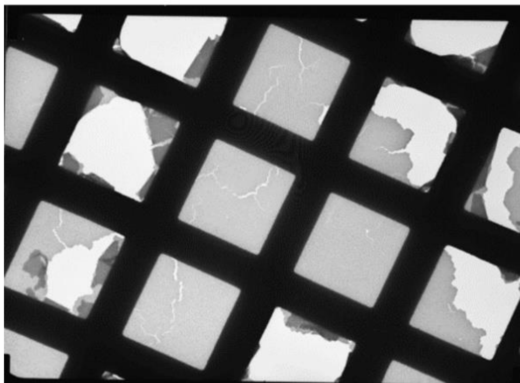

(c)

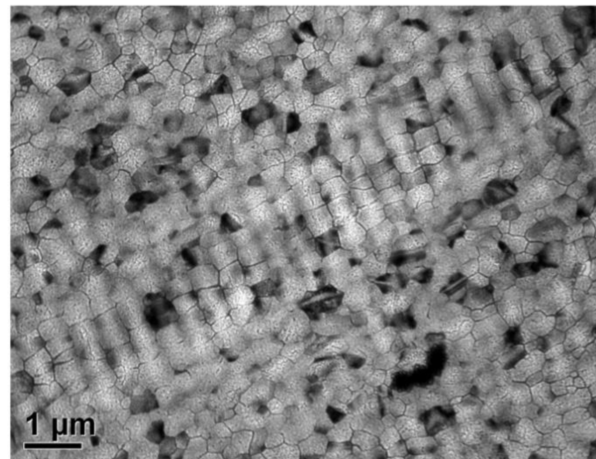

(d)

Figure 5.2: (a) A photo of JEOL 100CX TEM system used in the microstructure characterization, (b) the electron microscopy film after exposure and development, which captures the microstructure of the p-Si thin film, (c) the lifted ELA-generated p-Si thin film on a copper TEM grid, and (d) a TEM image showing distinct grains in the properly etched areas and blurry grains otherwise.

After the exposure and development of the electron microscopy film, we use an ultra-high-resolution scanner to digitize the captured image. The

final scanned TEM images of the p-Si thin films generated respectively with 5, 10, 15, 20, 25 and 30 shots of laser irradiation are shown in Figure 5.3. The images are of high quality with high resolution and contrast, which greatly facilitates the conversion of the TEM images into binary images using our computer program. At the first glance at the TEM images in Figure 5.3, it can be seen that with the increase in shot number the grain size generally increases, the shape of the grains becomes more square-like, and the arrangement of the grains becomes more ordered, which clearly shows the fact that microstructure evolves during the multiple shots of the ELA process and some characteristic evolution trends can be identified.

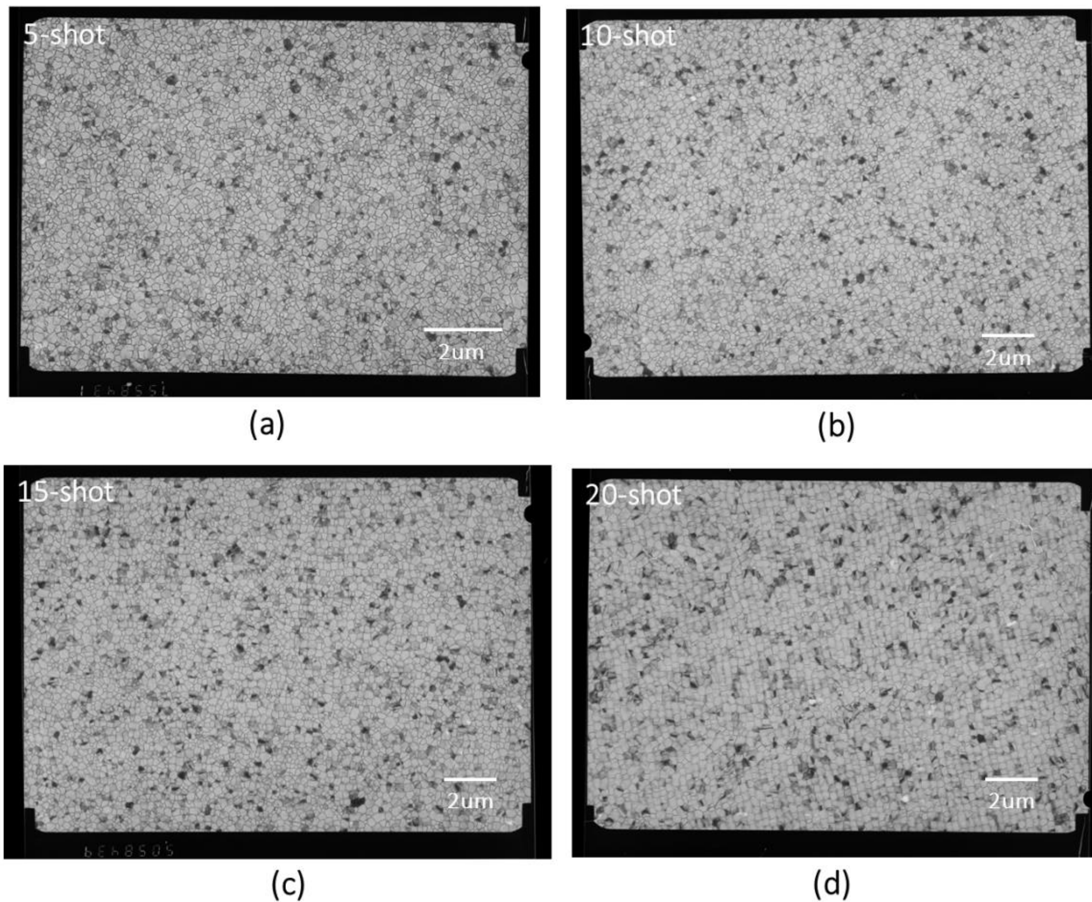

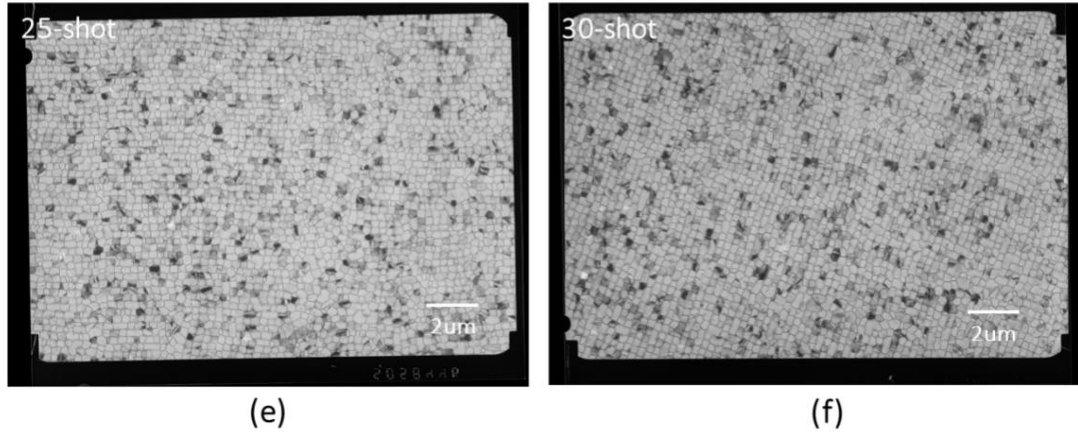

Figure 5.3: (a)-(d) The TEM images of the microstructure of the multiple-shot irradiated Si thin films respectively with 5, 10, 15, 20, 25 and 30 shots of laser irradiation. (a) is under 7500x magnification and the rest are under 5000x magnification. It can be qualitatively seen that the grain size generally increases and the grain distribution becomes more periodic as the shot number increases.

5.3 Systematic Microstructure Analysis and Comparison

We convert the above TEM images into GB maps using our developed Watershed-Segmentation-based GB extraction program. The GB maps are overlapped with the TEM image and shown in Figure 5.4, where we can see that the detection of the grain boundaries is very precise. With the GB maps, the microstructure of the p-Si generated with different shot numbers can be rigorously analyzed and effectively compared.

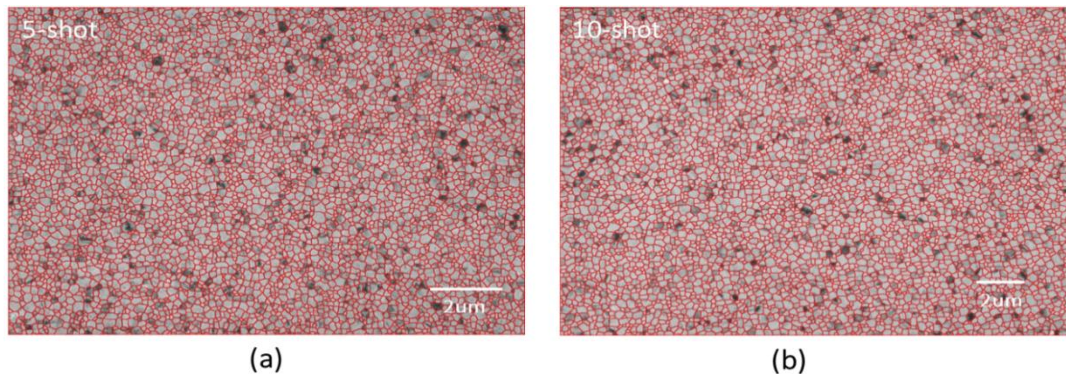

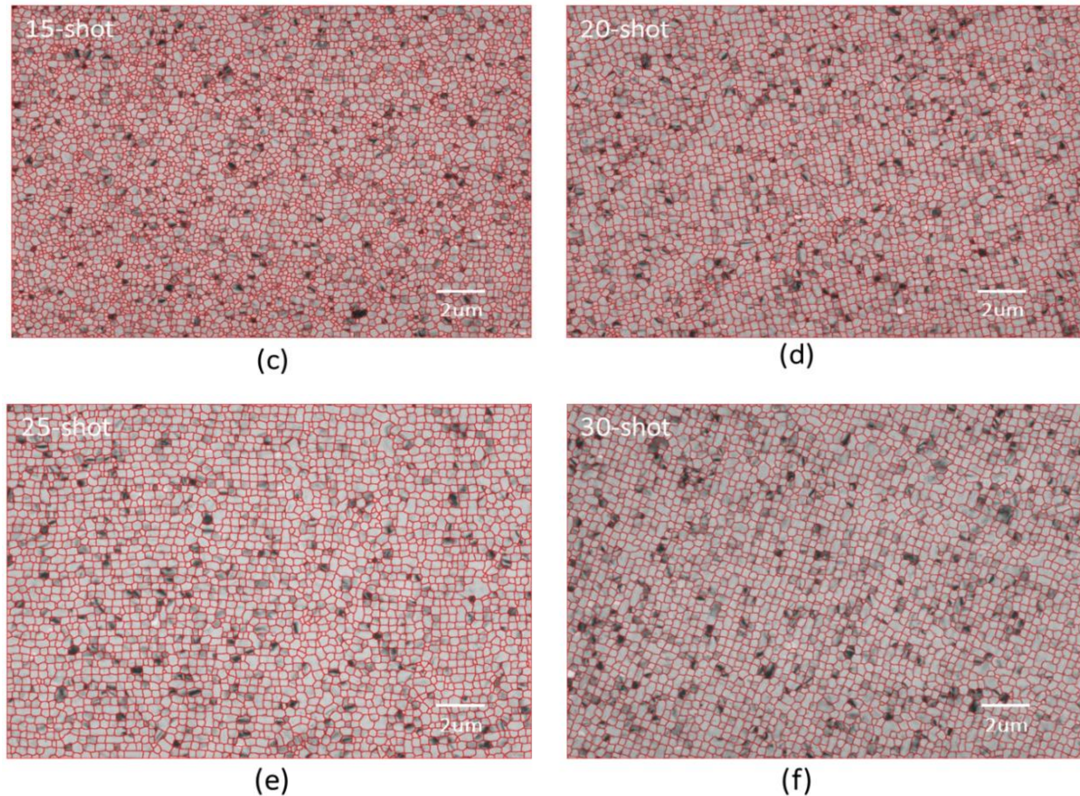

Figure 5. 4: The GB maps (red) overlapped with their source TEM images resulting from 5 shots (a), 10 shots (b), 15 shots (c), 20 shots (d), 25 shots (e) and 30 shots (f) of laser irradiation. It can be seen that the GB extraction is very precise.

5.3.1 Grain Size Statistics

The statistical grain-size distributions of the p-Si thin films generated respectively with 5, 10, 15, 20, 25 and 30 shots are shown in Figure 5.5. It can be seen that the grain size generally increases when the shot number increases. The width of the distribution is relatively narrower for 5-shots condition and getting wider when the shot number increases from 10 shots to 25 shots, and, at last, becomes narrow and sharp for the 30-shots condition. The mean values and standard deviations for different shot numbers are shown in Table 5.1.

Table 5. 1: The mean values and standard deviations of the p-Si grain size generated with different shot numbers.

	5-shot	10-shot	15-shot	20-shot	25-shot	30-shot
Mean Value	90nm	146nm	179nm	191nm	227nm	302nm
Standard Deviation	33nm	53nm	62nm	51nm	57nm	80nm

The distribution fits well with the log-normal distribution for smaller shot number conditions (5 shots and 10 shots), and deviates from the log-normal distribution for higher shot numbers. Steep slopes on the right are seen for the 20-, 25- and 30-shot conditions. For the 30-shots condition, a second peak is identified at around 450nm position.

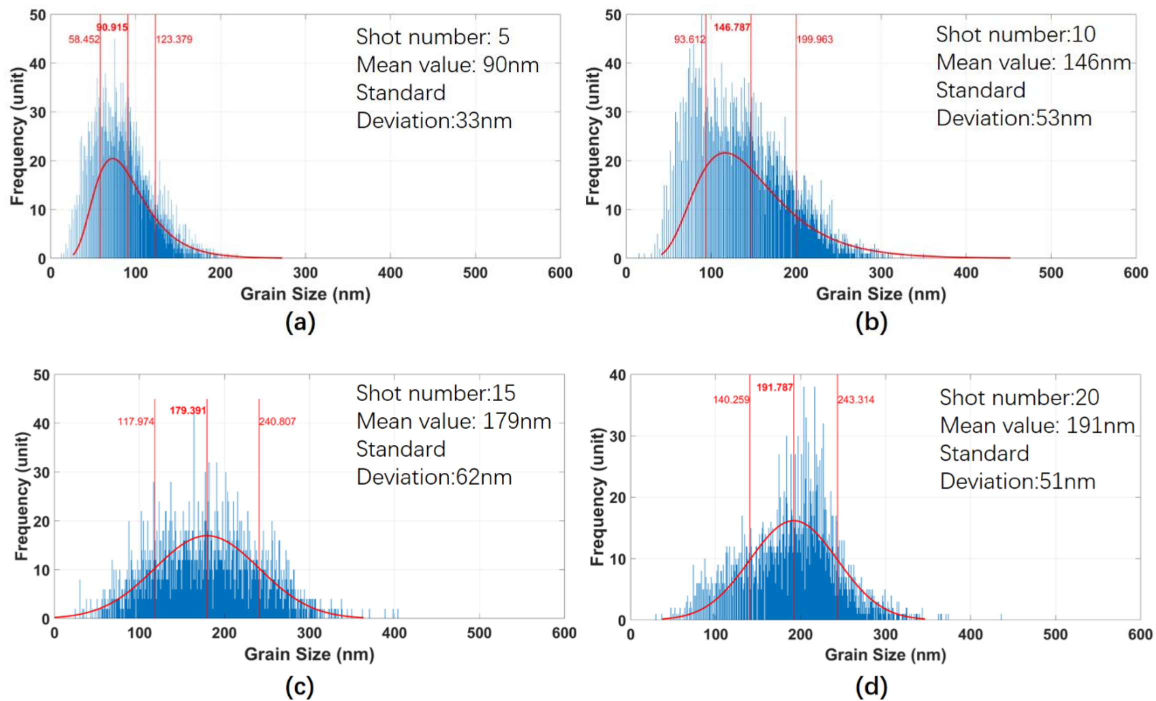

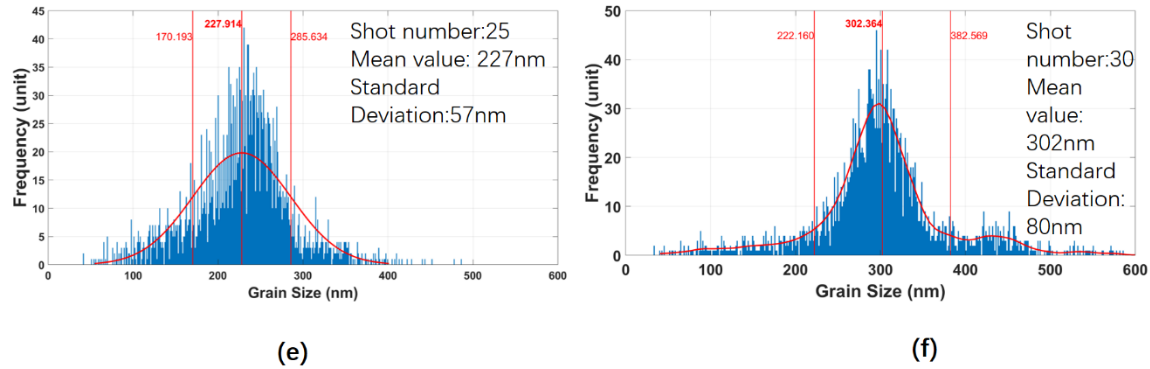

Figure 5. 5: (a)-(f) The statistical grain-size distributions of the multiple-shot irradiated p-Si thin films respectively under 5-, 10-, 15-, 20-, 25- and 30-shot conditions. The insets in the top right corner show the average and standard deviation.

5.3.2 The LMA-GB Density Analysis

We perform the LMA-GB density analysis by respectively assuming the probing TFT (circle) diameter to be 0.5μm and 2μm, of the six laser-shot conditions (i.e. 5 shots, 10 shots, 15 shots, 20shots, 25 shots and 30 shots). The result, presented in the form of the GB density heat map, with respect to 0.5μm diameter is shown Figure 5.6. The heat maps of Figure 5.6 (a)-(f) are respectively corresponding to 5-, 10-, 15-, 20-, 25-, and 30-shot conditions, where we can see that among all the shot-number conditions the microstructure of the 5-shot condition is relatively more locally uniform, but still, reading from the color bar, with the maximum α difference around 50% between the hottest and the coldest regions. Meanwhile the microstructure of the 30-shot condition is the most nonuniform with the maximum α difference around 120% between the hottest and the coldest regions. Additionally, beyond 10 shots the square-like heat map features appear and become clearer with the increase of shot number as a result of the onset of the square-like grain geometry and the abrupt variation of the α values within a

small range. This means that when the TFT size is small, especially comparable to or even smaller than the grain size, the total grain boundary length underneath a TFT would fluctuate significantly from location to location.

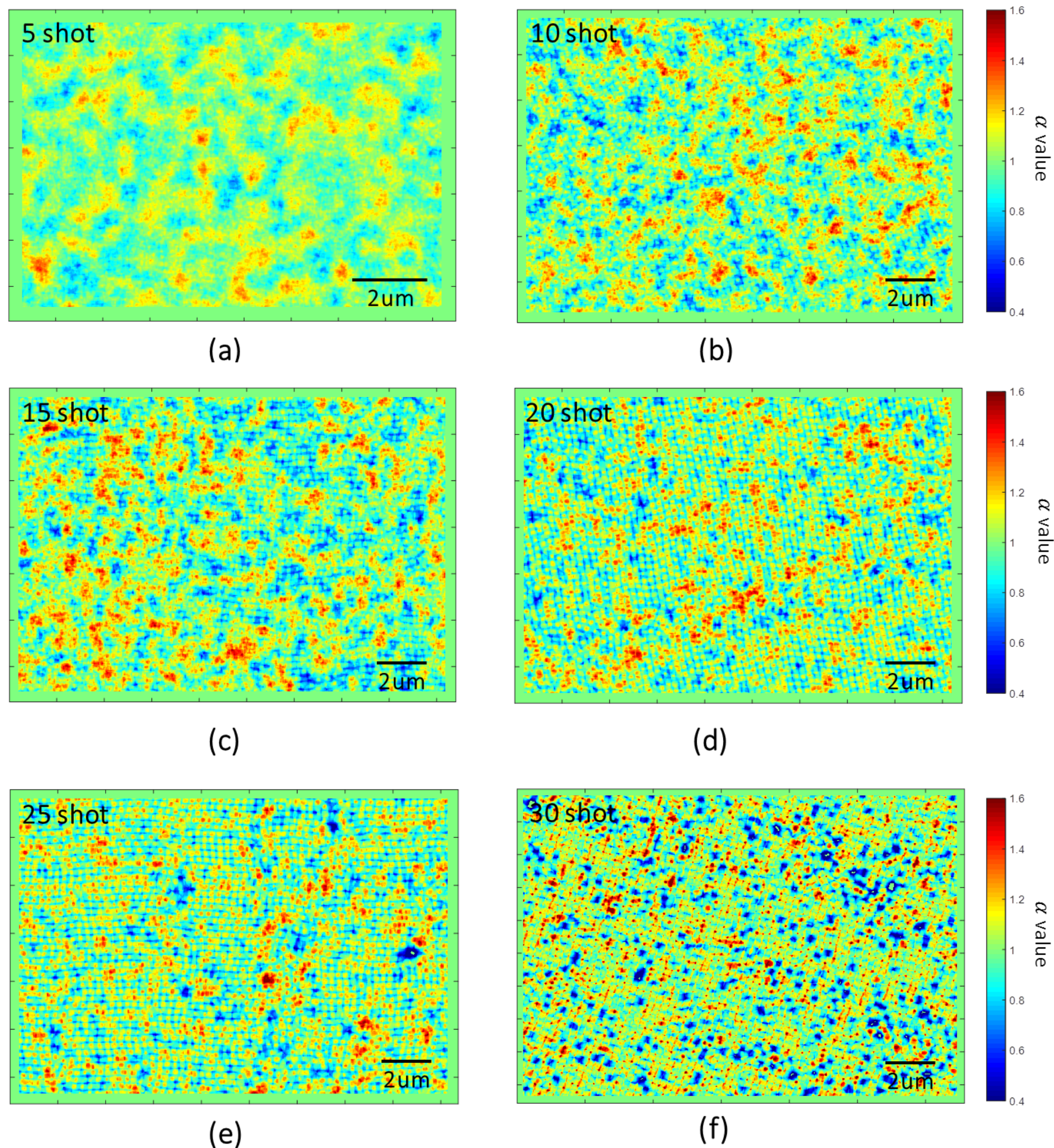

Figure 5. 6: (a)-(f) The heat maps of the relative defect density distribution of multiple-shot-irradiated p-Si under 5-, 10-, 15-, 20-, 25- and 30-shot conditions with respect to 0.5µm TFT size, where the 'hot' area represents high relative defect density regions, while the 'cold" area represents low relative defect density regions. The local microstructure of the 5-shot condition is the most uniform one with 50% α peak-to-valley difference, while (f) that in the 30-shot condition is the most nonuniform one with 120% α difference.

Figure 5.7 shows the heat maps with respect to 2µm probing TFT

diameter, where Figure 5.7 (a)-(f) are corresponding to 5-, 10-, 15-shot, 20-, 25- and 30-shot conditions. It can be seen that the color variation in this batch of heat maps is generally smoother compared to those shown in Figure 5.6. The peak-to-valley α difference in the most uniform 5-shot condition is around 20%, while that in the most nonuniform 30-shot condition is around 30%.

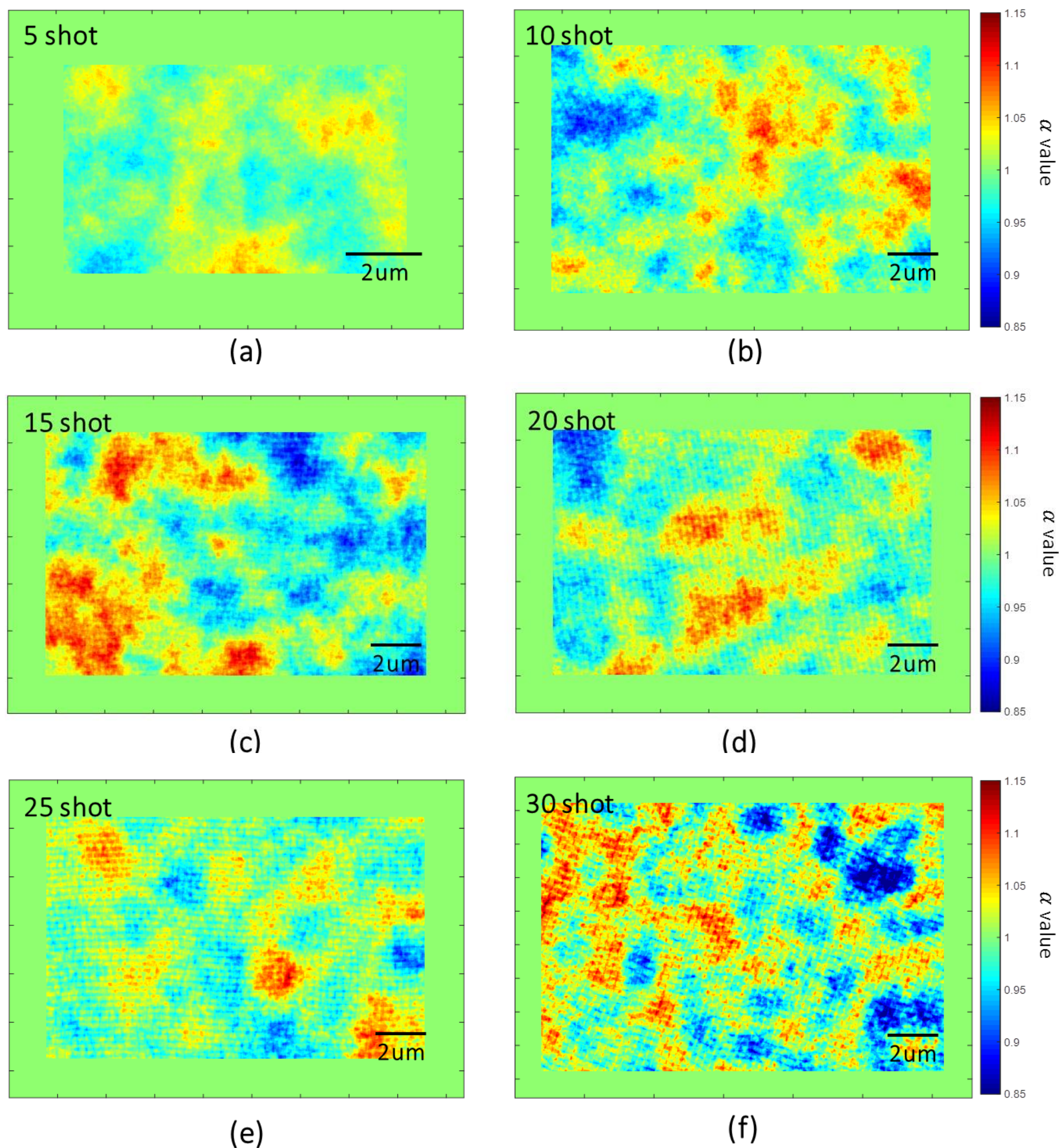

Figure 5.7: (a)-(f) The heat maps of the relative defect density distribution of multiple-shot irradiated p-Si under 5-, 10-, 15-, 20-, 25- and 30-shot conditions with respect to 2μm TFT

size, where the 'hot' area represents high relative defect density regions, while the 'cold" area represents low relative defect density regions. It should be pointed out that the range of the color bars of 0.5μm TFT size condition and 2μm TFT size condition are different, which are respectively 0.4 to 1.6 for the 0.5μm TFT size condition and 0.85 to 1.15 for 2μm TFT size condition.

5.3.3 The LMA-Orientation Analysis

We perform the LMA-GB orientation analysis of the microstructure generated by the six laser-shot conditions. The results that present the largest, median and the smallest standard deviations of α values from the 5-shot and the 30-shot conditions are selected and organized in Table 5.2.

Table 5. 2: Standard deviations of the α value at selected orientations in 5- and 30-shot conditions.

5-shot	0°	90°	165°
Standard Deviation	4.2%	4.6%	4.1%
10-shot	30°	75°	135°
Standard Deviation	9.6%	11.6%	9.3%

The GB density heat maps and the corresponding statistical histograms at the selected orientations in 5- and 30-shot conditions are presented in Figure 5.8. For the 5-shot condition, at the first glance, the heat maps look generally uniform at all the selected orientations. The standard deviation maximizes at 4.55% for 90°and minimizes at 4.07% for 165°with respect to the horizon. The difference of these two standard deviations is marginally small, being

0.48%. Meanwhile, for the 30-shot condition, the nonuniformity of the α value is evidently much higher than that of the 5-shot condition. The standard deviation maximizes at 11.61% for 75 and minimizes at 9.26% at 135 with respect to the horizon and the difference of these two standard deviations is 2.35%, which would likely yield a noticeable difference of the products in manufacturing.

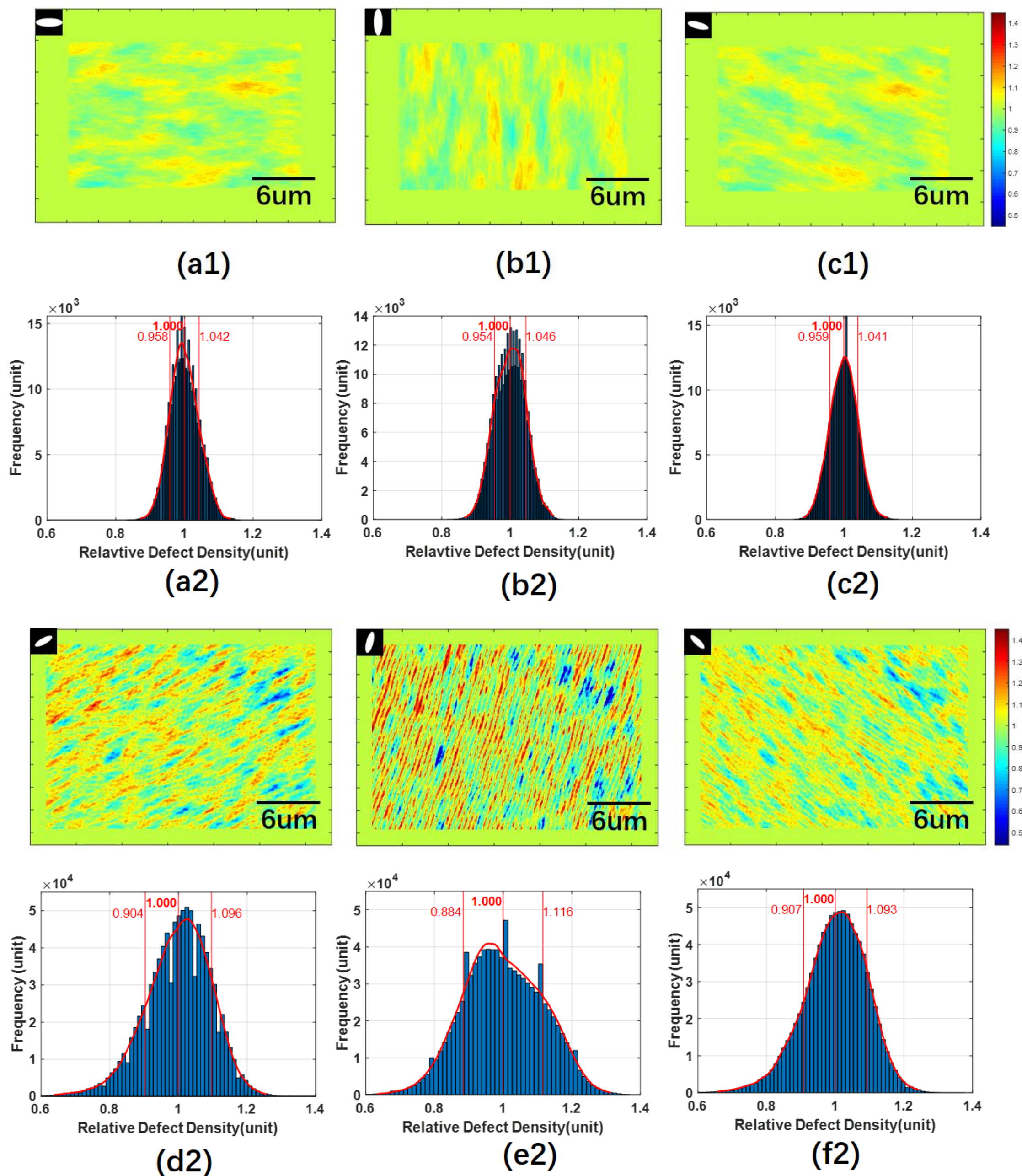

Figure 5.8: (a1) (a2)-(c1)(c2) Figure pairs of the heat maps and statistical histograms of the spatial distribution of the relative defect density, respectively corresponding to 0°, 90° and 165°TFT orientations for the 5-shot condition, and (d1)(d2)-(f1)(f2) same figure pairs respectively corresponding to 30°, 75° and 135° orientations for the 30-shot condition. Top left corner insets show the probing oval (3μm×1μm) and its orientation used to generate the heat maps.

5.3.4 Periodicity Analysis

Recall that in Figure 5.4 we could intuitively tell that the microstructure of the 5-shot condition does not exhibit periodicity of grain arrangement, which, on the other hand, seems apparent in the microstructure of the 30-shot condition. It was demonstrated in the subsection 4.2.3 that filtering the Fourier Transform image could help identify the existence of the periodicity, while the inversed Fourier Transform, associated with the area fraction of periodicity, could quantitatively describe the extent of the periodicity in the whole area of the film. Figure 5.9 presents the filtered FFT and the IFFT results of the six laser-shot conditions. Figure 5.9 (a1) (a2) (a3) - (f1) (f2) (f3) are the overlapped images of TEM image and the GB map, diffraction patterns of FFT after filtering the background signals and noises, and the IFFT images of highlighted periodic area respectively for 5-, 10-, 15-, 20-, 25- and 30-shot conditions. In the filtered FFT image of Figure 5.9 (a2), no diffraction patterns can be identified and, as a result, there is no visibly highlighted area in the corresponding IFFT image of Figure 5.9 (a3). The two semicircles shown in image Figure 5.9 (b2) indicate a weak two-fold periodicity which cannot be easily identified by a human eye, but is still detected by the FFT method, and the highlighted periodic area is shown in Figure 5.9 (b3). In Figure 5.9 (c2),

two orders of diffraction pattern appear, which indicates the enhancement of the periodicity and the enlargement of the periodic area as shown in image (c3). In Figure 5.9 (d2), three orders of diffraction pattern appear, indicating the further enhancement of the periodicity, and, in addition, another diffraction pattern in semicircle shape emerges in the direction perpendicular to the original diffraction patterns, which indicates that significant periodicity starts to form in a new direction. In Figure 5.9 (e2) and (f2), it can be seen that the periodicity continuously enhances in both of the two perpendicular directions when the shot number increases, as evidenced by the increase and the sharpening of the diffraction orders as well as the continuous enlargement of the periodic area shown in Figure 5.9 (e3) and (f3). The periodicity shown in the two perpendicular directions is a result of the square-like shape of the grain geometry.

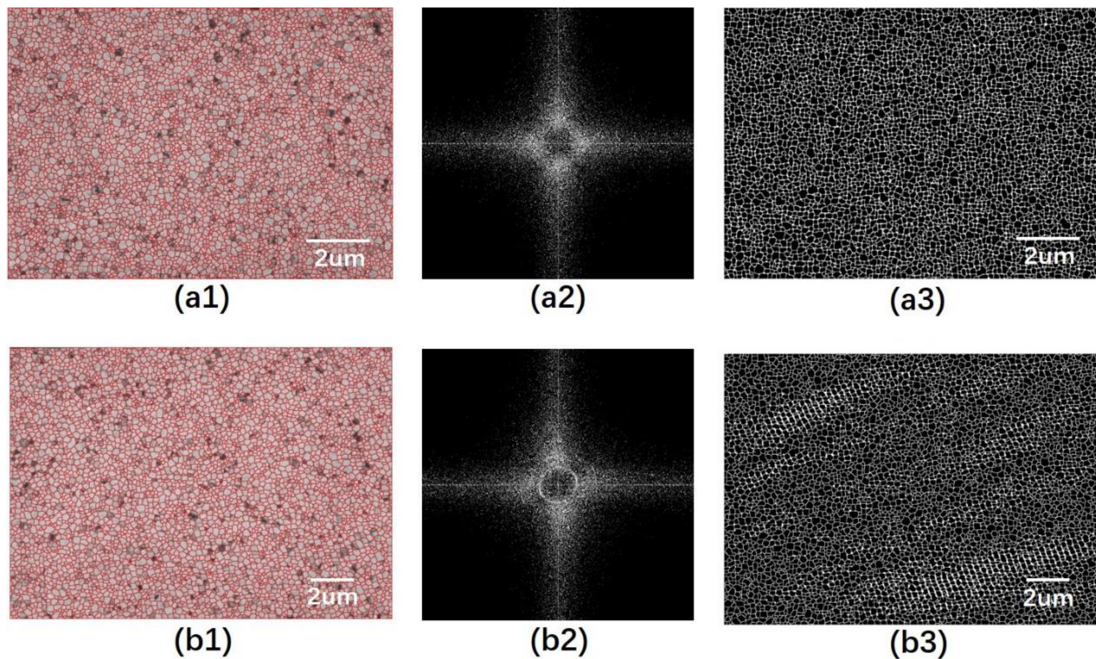

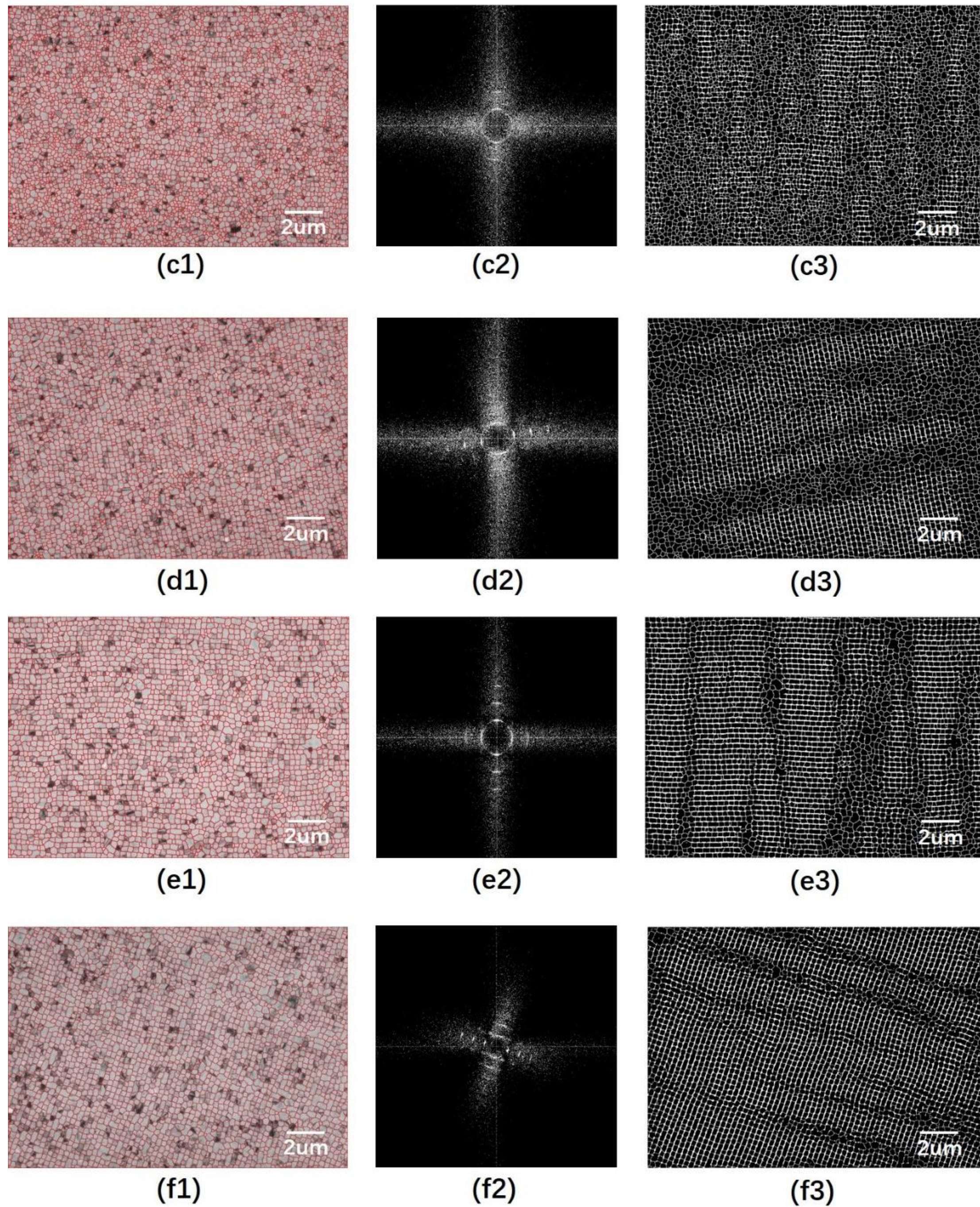

Figure 5.9: (a1) (a2) (a3) - (f1) (f2) (f3) Figure sets of the overlapped image of TEM image and the GB map, FFTs of the GB map with filtered background signals and noises, and the IFFTs of the filtered FFT image, which highlight the periodic area respectively for the 5-, 10-, 15-, 20-, 25- and 30-shot conditions of laser irradiation. The area fraction of periodicity is apparently enhanced as the shot number increases.

5.4 Discussion

The above results of the systematic analysis of the microstructure of the ELA-generated p-Si thin films are mutually corroborated with each other and contain fruitful information. By correlating and comparing the analysis results of the above four aspects lead us to comprehensively understand the microstructure and the related material properties, as well as to appreciate the profound implications about the phase transformation mechanisms underlying the ELA process.

The statistical grain-size histograms and the fitted curves of 5-shot, 10-shot, 15-shot, 20-shot, 25-shot and 30-shot conditions, as respectively shown in Figure 5.5 (a)-(f), reveal a plenty of information. First, looking at the Figure 5.5, we see that with the increase in shot number the average grain size increases, which is the grain enlargement tendency expected from annealing. Secondly, since the total area of the analyzed film is the same, the increase of the average grain size implies elimination (or disappearance) of small grains during the repeated laser irradiation. Thirdly, the increasing deviation from the log-normal distribution of the grain-size statistics as the shot number increases comes along with the increment of the periodicity of the grain arrangement. This further supports the theory that the abnormal grain-size distribution is due the light-diffraction phenomenon, which is amplified by the periodic structure.

Figure 5.10 compares the fitted curves to the statistical α-value histograms from Figures 5.6 and 5.7. Figure 5.10 (a) and (b) respectively correspond to 0.5μm probing TFT size and 2μm probing TFT size for the six laser-shot conditions, and (c) is the comparison of (a) (dashed lines) and (b) (solid lines). For the 0.5μm TFT size, as shown in Figure 5.10 (a), the 5-shot

condition yields the narrowest distribution, and the distributions become broader as the shot number increases until 30 shots, when the distribution gets narrower again. If we recall the TEM images in Figure 5.3, the grain-size statistics in Figure 5.5 and the GB density heat maps in Figure 5.6, this trend can be understood as follows. The grain sizes generated under 5-shot condition are around 100nm, as shown in Figure 5.5 (a), and are much smaller than the 0.5μm TFT size, thus the α value can always be considered as very uniform, leading to the narrow distribution. As the shot number increases from 10 shots to 25 shots, we start seeing a coexistence of a large number of small grains (less than 100nm) and large grains (around 300nm) with the medium grains, all non-uniformly distributed in the area. Since the TFT size is 500nm, which is comparable to the size of the larger grains, the α values would considerably fluctuate when scanning across small-grain area and large-grain area, leading to the broad statistical distribution for 10- to 25-shot conditions. When the shot number reaches 30 shots, the size of the grains becomes considerably uniform, as shown in Figure 5.5 (f), and the spatial distribution of the grains becomes ordered and periodic. Therefore, the GB density that one TFT faces at different locations becomes less discrepant, resulting in a narrower GB density distribution compared to those from the 10- to 25-shot conditions. The 2μm TFT size is much larger compared to the size of the grains generated by each of the six laser-shot conditions, therefore the α values do not vary much among the different locations, resulting in the narrow statistical local α value distribution shown in Figure 5.10 (b). The results of 0.5μm TFT size and 2μm TFT size are compared in the same plot of Figure 5.10 (c), where we can see that when the TFT size is 2μm, the uniformity of the α values for all of the laser-shot conditions is generally much better than that of 0.5μm TFT size. From the above discussions, it can be seen that if the

grain size is small enough compared to the size of a TFT, the local microstructure of the film can always be regarded as location-independently uniform. However, on the other hand, small TFTs and large grains are the desired direction of pursuit in the application of ELA p-Si thin film for increasing display resolution and carrier mobility. Therefore, there should exist a tradeoff between the TFT size and the achievable grain size, which could give the engineers an optimized combination of the two factors and lead to the best product performance. In addition, according to the analysis in the subsection 5.3.3, the local variation of the defect density is also orientation-dependent, especially when the grain sizes are large. We suggest that when designing the ELA material, the relevant manufacturing processes and the microelectronic elements, the process engineer should at least take all of the influential factors that have been discussed above into consideration.

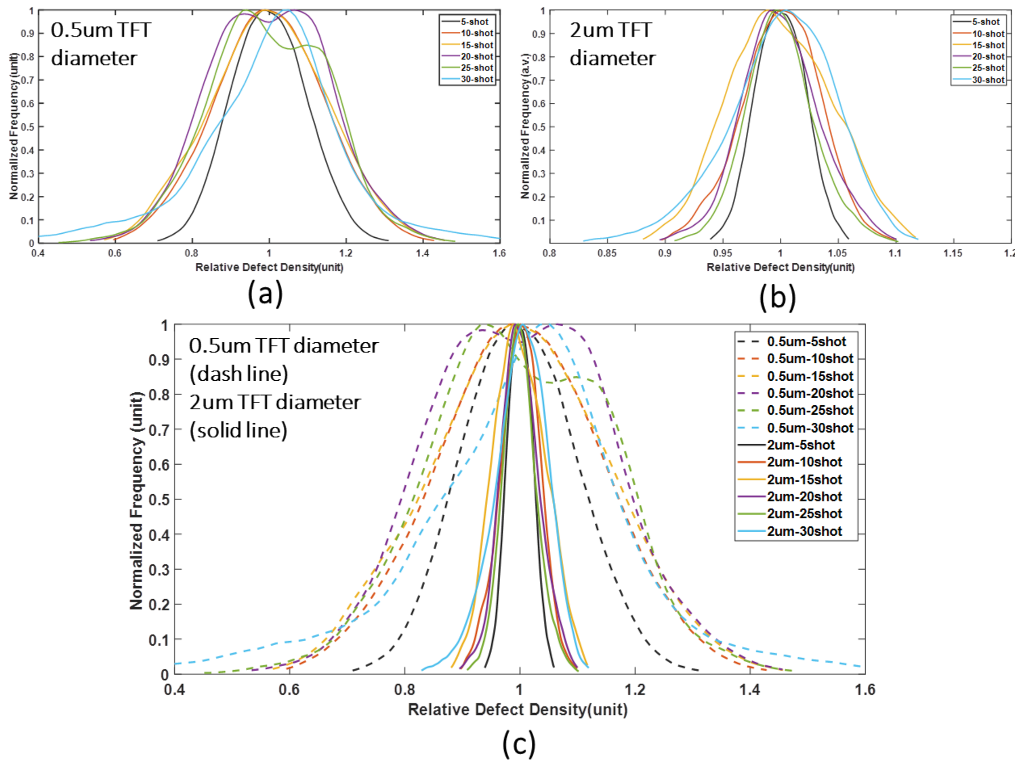

Figure 5. 10: (a) and (b) The fitted curves of the statistical histograms of the α values

respectively corresponding to 0.5μm TFT size and 2μm TFT size for the six laser-shot conditions, (c) The comparison of (a) (dashed lines) and (b) (solid lines) in the same plot. If the device size is large enough compared to the grain size, the microstructure can always be treated as location-independently uniform. However, the display technology is always seeking for the opposite direction, where small device size and large grain size are preferred. Thus, such analysis potentially provides engineers with a tool to quantitatively look for the optimal combination between the device size and the available ELA p-Si grain size when designing their products.

The area fraction of periodicity (γ) for the six laser-shot conditions are calculated to be 0%, 17.12%, 38.95%, 57.18%, 70.76%, 88.25%, which shows a monotonic improvement of the periodicity as the shot number increases. It is apparent that the grain size becomes more uniform with the increase of the area fraction of the periodicity. Besides, by comparing Figure 5.5 and Figure 5.9, we can see the close connection between the grain-size distribution and the periodicity: the statistical grain size distribution deviates more from the log-normal distribution as γ increases. The grain size distribution starts out very close to log-normal for the 5-shot condition, where no periodicity exists. In contrast, the grain size distribution for the 30-shot condition is somewhat bi-modal, where the γ value is as high as 88.25% and the vast areas of uniform and periodic grains coexist with areas of slightly larger grains.

As introduced in the work of Van der Wilt et. al [21], the interference of the excimer laser light induces some surface roughness with the 308nm periodicity corresponding to the Excimer laser wavelength. Those surface protrusions enhance the non-uniform energy deposition by diffracting the incident light during the next irradiation cycles, causing the growth of the periodic areas and a deviation from the purely stochastic grain formation

process. The increased periodicity will then in turn enhance the light diffraction. Thus, we say that the development of periodicity and the increase of light diffraction mutually enhance each other. In such way, the ELA microstructure and the abnormal grain-size distribution are developed.

5.5 Summary

In this chapter, we firstly design and conduct a series of systematic ELA experiments using different shot number ranging from 5 shots to 30 shots with an increment of 5 shots for each step. Next, high-quality TEM images of the ELA microstructures are successfully captured over sufficiently large areas, which has not been achieved in the previous ELA studies, by taking the advantage of our unique sample preparation and TEM skills. The GB maps are then generated from the TEM images using our Watershed-Segmentation program, forming the base for the following microstructure analyses. Then comprehensive and systematic microstructure analysis are performed, focusing on the four microstructure aspects, which are the statistics of grain size, LMA-GB density analysis, LMA-orientation analysis and the periodicity analysis for all the laser-shot conditions (i.e. 5-shot, 10-shot, 15-shot, 20-shot, 25-shot and 30-shot). The results of different shot-number conditions (1) provide the engineers with some clues about the ELA microstructure and the related device performance, and (2) reveal how the microstructure evolves during the ELA process, which helps us appreciate the phase transformation mechanisms in the repeated melting and solidification processes.

Chapter 6

Surface Planarization of As-is ELA Si Thin Films

The surface of the ELA-generated p-Si thin film is rough. It has been commonly recognized that a rough surface of the semiconductor material is detrimental to the microelectronic devices and, in many cases, also causes difficulties in the microfabrication. The surface roughness, especially when the roughness is of high-aspect ratio, induces locally enhanced electric field and reduces the effective thickness of the dielectric gate material, which is believed to be one of the reasons causing the decrease of the breakdown voltage and the shift of the characteristic I-V curve of the transistors. Thus, the reduction of the surface roughness is strongly demanded by the ELA-related industrial applications. In this chapter, we first conduct a characterization of the surface morphology of ELA-generated p-Si thin films and then seek for the possibilities to reduce the surface roughness. One previous study is recognized [82], where laser irradiation is adopted to

successfully planarize the surface roughness of single crystalline silicon (c-Si) and, being inspired by this work, we try to use the excimer laser to reduce the surface roughness of the ELA-generated films while maintaining the original geometry and the spatial arrangement of the grains. The experiment on oxide-capped p-Si described in this chapter did not achieve that goal. However, the characterization tools we developed for this experiment gave us precious *in situ* information about the melting and solidification scenario throughout each excimer laser irradiation. A numerical simulation was implemented to more vividly describe and better understand the melting and solidification process. These details coupled with the results of the extensive microstructure evolution analysis presented in chapter 5 allowed us to come up with a better approach and a more successful planarization experiment described in chapter 7.

6.1 Characterization of Surface Morphology

The surface morphology of the as-received industry-grade ELA p-Si thin film (as-is sample) is characterized via atomic force microscope (AFM) and shown in Figure 6.1 (a) featuring periodic protrusions, the root mean square (RMS) roughness of which, as shown in Figure 6.2 (b) is measured to be 13.75nm. Protrusions are known to be located above the grain boundaries, as in the example in Figure 6 (c), where the grain boundaries were selectively exposed by etching [21].

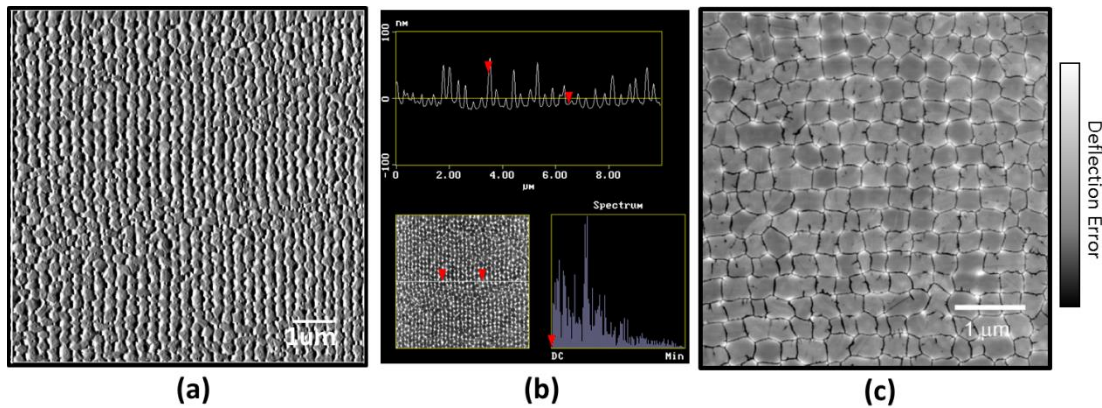

Figure 6. 1: (a) the AFM image of an as-is ELA-generated p-Si thin film, (b) the roughness analysis at one cross-section of (a), and (c) one previously reported high-resolution AFM image of the surface morphology where the grain junctions are selectively etched by a Secco etchant [21]. The root-mean-square (RMS) surface roughness of the as-is generated film is measured to be 13.75nm. It can be seen from (c) that the protrusions are located right at the grain boundary location.

6.2 The Previous Study of Surface Planarization

Earlier attempts of Si surface planarization were focused on compensating for the anisotropic etching of c-Si wafers. In the year of 1996, *A. Bosseboeuf et al* used an excimer laser to planarize the rough surface of a c-Si wafer prepatterned with rectangular steps and ridges [82]. The surface morphology before and after planarization is compared in Figure 6.2 (a) and (b), where the RMS roughness has been successfully reduced from 25 nm down to around 7nm. The original geometry of the prepatterned structures was also fully preserved. Hence, we were asked by industry to attempt reducing the rough surface of the ELA film via using excimer laser irradiation, since such a method would be of great convenient in the ELA manufacturing.

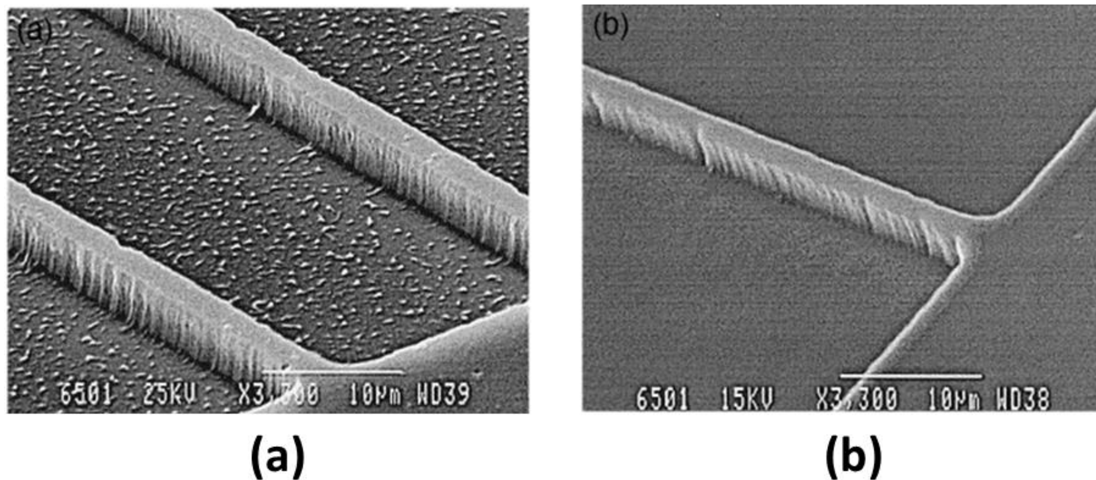

Figure 6.2: Scanning electron microscope (SEM) images of the patterned c-Si wafer surface, (a) before and (b) after excimer-laser-induced planarization [62]. From the comparison, it can be seen that the planarization is very effective while the original geometry of the prepatterned rectangular steps and ridges are also fully preserved. We need to reduce the RMS surface roughness as much as possible while still maintaining the original ELA microstructure to be unchanged.

6.3 Planarization Experiments

6.3.1 Experimental Details

The planarization experiments are done on the as-is sample under the same experiment conditions as in the subsection 5.1.3, where the wavelength of the laser beam is 308nm with the pulse duration is 30ns at FWHM. The irradiated area is selected to be 1mm×1mm using the projection system. In addition, optical in-situ probing system is set up to detect the changes in transient reflectance (TR) and transient transmittance (TT) of the Si film during melting and solidification. The setup is schematically shown in Figure 6.3. A TT probing laser is set to overlap with the excimer laser and is vertically

incident upon the front surface of the sample, while a photodetector is set on the other side of the sample to receive the transmission signal. A TR probing laser and a photodetector are placed on the top side of the sample to detect the transient reflectance from the front surface, termed the front-side transient reflectance (FTR) of the p-Si film. Another TR probing laser and photodetector pair is placed on the bottom side of the sample to detect the transient reflectance from the back surface, referred to as the backside transient reflectance (BTR) of the p-Si film. The TR and TT lasers are continuous-wave laser diodes with the wavelength of 670nm, which is not significantly absorbed by Si. The spot size of lasers is around 75μm × 300μm, much smaller than selected excimer spot size, thus it can be safely assumed that the TT and TR signals are collected from a uniformly irradiated area. The photodetectors are equipped with ultraviolet light filters to block the possible disturbance caused by the excimer laser. The transparent substrate of the ELA sample enables a simultaneous measurement of the FTR, BTR and TT signals. All signals are recorded by a multi-channel digital oscilloscope with a 0.2ns sampling rate. In order to ensure that the three signals are directly comparable, identical electrical components including photodetectors, lasers and connecting cables are used. The signals are smoothed and enhanced by increasing signal-to-noise ratio and filtering high-frequency noises using Savitzky-Golay filters.

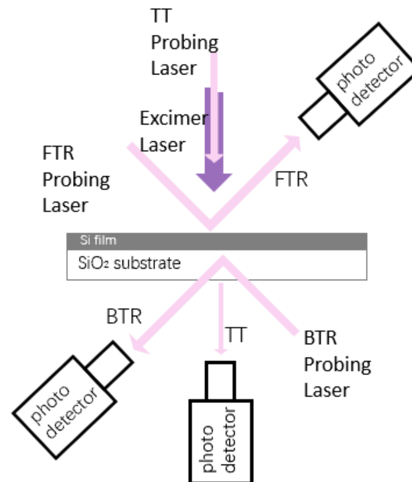

Figure 6.3: The schematic of the in-situ optical probing system used to measure the transient reflectance from the front surface (FTR), the bottom side of the p-Si thin film (BTR) and the transient transmittance (TT) of probing lasers. The probing laser does not affect the melting and solidification process of the film. The spot size of the probing laser is much smaller than that of the excimer laser.

With the in-situ optical probing system in place, a set of planarization experiments with a single excimer laser shot was performed. The energy window of excimer-laser is selected to be around 70% to 90% of the complete melting threshold (CMT) of the as-is ELA-generated film. After the planarization experiments, the surface morphology and the RMS surface roughness are characterized by the AFM. The native surface oxide covering the front surface of the samples was preserved during the irradiation but had to be removed using BHF for successful AFM characterization.

6.3.2 Results and Analysis

The RMS surface roughness of the original as-is ELA-generated sample is around 13.75nm. We chose four energy levels of the excimer laser to perform the planarization experiments, which are respectively 70%, 75%, 85%

and 90% of the CMT; the results are shown in Figure 6.4. It can be seen that the surface morphologies shown in Figure 6.4 (a), (b) and (c) do not exhibit notable difference from that of the original sample, while the surface morphology in Figure 6.4 (d) is noticeably different. Figure 6.4 (e) compares the RMS surface roughness of the original sample and the four processed samples, where it can be seen that no significant planarization is achieved but, on the contrary, the RMS surface roughness increases for the energy conditions of 75% and 85% of CMT. We can further observe that firstly, the RMS roughness of the sample processed under 70% CMT condition is similar to that in the original sample, meaning that either such laser energy level is insufficient to trigger melting of the as-is p-Si thin film or the melting induced by the laser irradiation is not strong enough to affect the surface roughness. Secondly, the RMS roughness of the samples processed under 75% and 85% of CMT clearly increases, while the surface morphology does not notably change, meaning that the laser energy is now high enough to cause some extent of melting of the films to affect the roughness, but the surface morphology restores after resolidification. Thirdly, the significant change in the surface morphology of the sample processed at 90% CMT indicates substantial melting of the film. If we carefully look at the AFM image of Figure 6.4 (d), three new features can be clearly identified, which are (1) the formation of new circle-like protrusions, (2) the generally flat and smooth area between the circle-like protrusions and (3) the small and isolated protrusions on the flat area. According to the previous studies conducted in our group, we can safely claim that large grains with flat and smooth interior area are formed under such energy condition and the circle-like protrusions are at the junction locations of neighboring grains. The formation of the large grains under the condition of 90% CMT is consistent with the phase transformation scenario

in the near-complete melting regime described in the subsection 2.2.2. Here the melting of the solid is so substantial that only a few solid islands preserve, sparsely distributed throughout the sample. When the irradiation ceases the super-lateral growth (SLG) results in such large grains with smooth surface across the grain bodies. Interestingly, small and isolated protrusion islands, which line up in the vertical direction with a periodicity similar to the original samples, are found inside the SLG regions. We argue that the isolated protrusions are redeveloped at the same locations of the original protrusions, which is caused by the native surface oxide layer, which retards the liquid follow during melting and solidification. More evidence supporting this argument will be provided in the next chapter. Even though the RMS roughness of the sample processed under the condition of 90% CMT decreased by around 2nm from the as-is film, this improvement may not be able to be directly applied in the current manufacturing, since the microstructure significantly changes, which would very likely lead to the change of material properties and needs to be further evaluated.

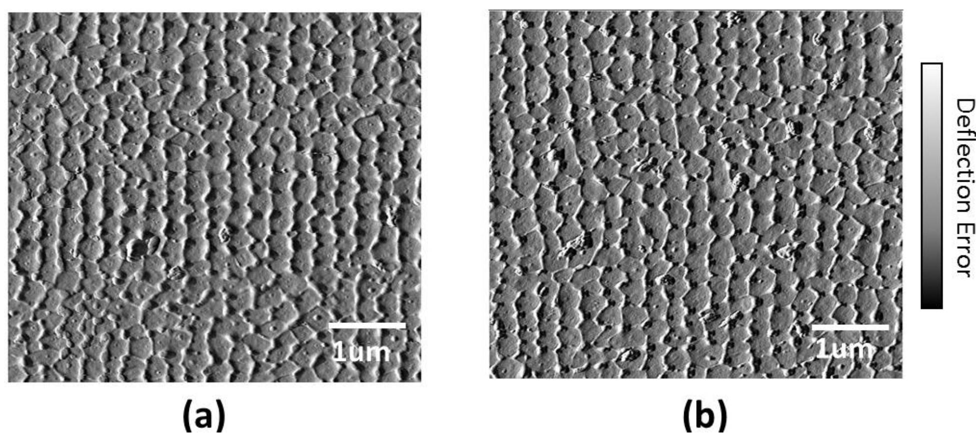

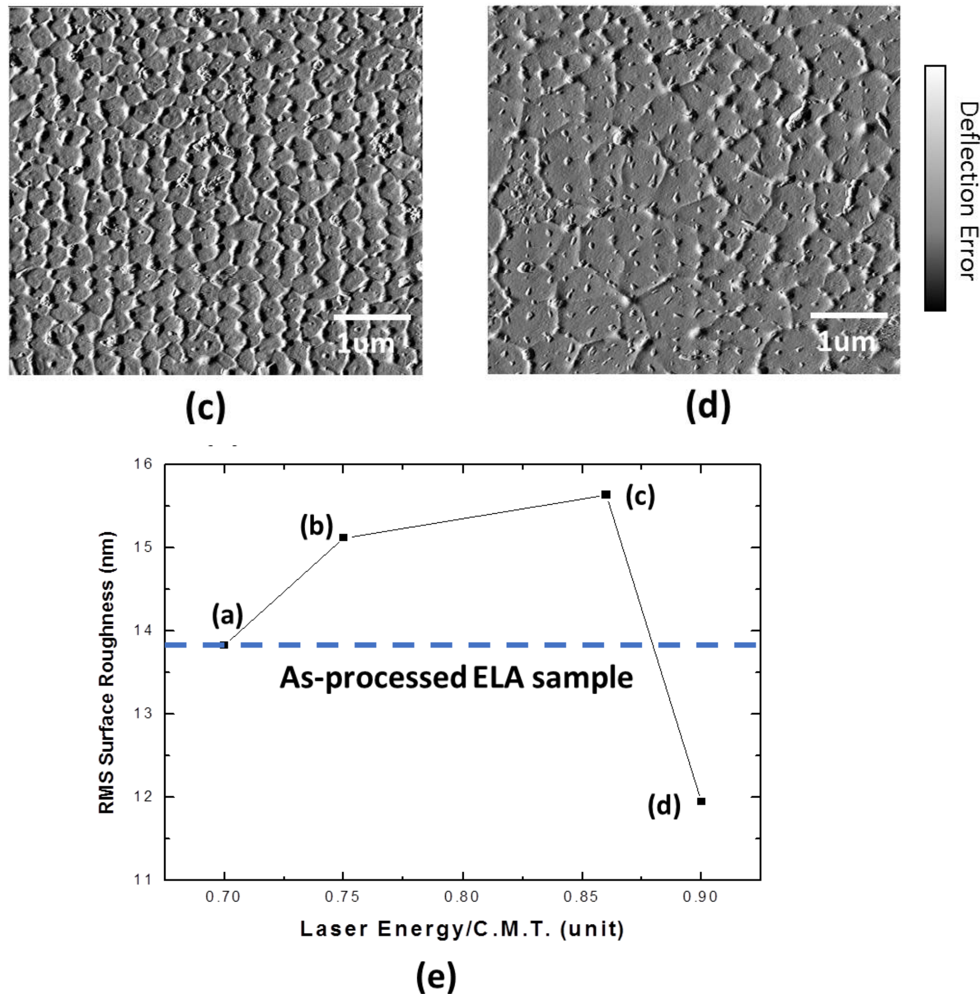

Figure 6.4: (a)-(d) The AFM images of the sample surfaces after irradiation at 70%, 75%, 85% and 90% CMT respectively. (e) The plot of RMS surface roughness after planarization versus laser energy. The horizontal dashed line is the original RMS surface roughness. The RMS is 13.75nm before irradiation and even increases after irradiation. Surface planarization is not successful achieved in this set of experiments.

6.3.3 Transient Reflectance and Transmittance Analysis

The in-situ optical probing method is used to collect spatiotemporal information of the melting and solidification scenario during the planarization experiments, where the transient FTR, BTR and TT signals are recorded,

analyzed and compared among the four energy conditions. The results are shown in Figure 6.5 where the image pairs (a1) (a2) to (d1) (d2) are the AFM images and the in-situ signals of the probing laser respectively corresponding to the excimer-laser energy conditions of 70%, 75%, 85% and 90% CMT, and the back, red and blue signals respectively represent the FTR, BTR and TT. For the 70% CMT condition, a small hump appearing in the FTR signal indicates the onset of melting causing an abrupt increase of reflectivity when Si transforms from solid to liquid. The extent of melting has to be quite limited at 70% CMT because the FTR signal hump is very small. The lack of distinct changes in the BTR signal signifies that the melting only happens at the front side of the film and does not propagate to the bottom side. The dip appearing in the TT signal is also attributed to the sudden transition from the solid phase to the liquid phase of Si. The gradual change of the signals after about 150ns has nothing to do with the phase transition, but occurs merely because of the temperature-dependent nature of the reflectivity of Si. Humps appear in the BTR signals for the other three energy conditions, indicating the formation of liquid phase at the bottom side of the film, and, as the laser energy increases, the humps in both FTR and BTR signals simultaneously enlarge, indicating the enhancement of the extent of melting. The humps in the BTR signals are very temporally close with those in the FTR signals, which means that the amount of liquid simultaneously increases or decreases at both the front and the bottom sides of the film during melting and solidification. The broad dip of TT signal in Figure 4.6 (d2) is an evidence of substantial melting happening at the high excimer-laser energy level. However, it should be emphasized that although the film already melts substantially in the case of Figure 4.6 (d2), still no continuous liquid layer forms at the front surface, as indicated by the absence of a plateau in the FTR signal introduced in the subsection 2.2.3.

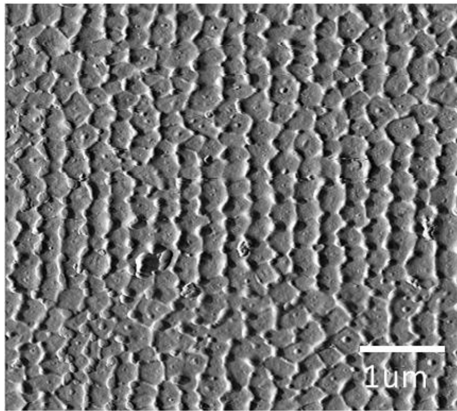

(a1)

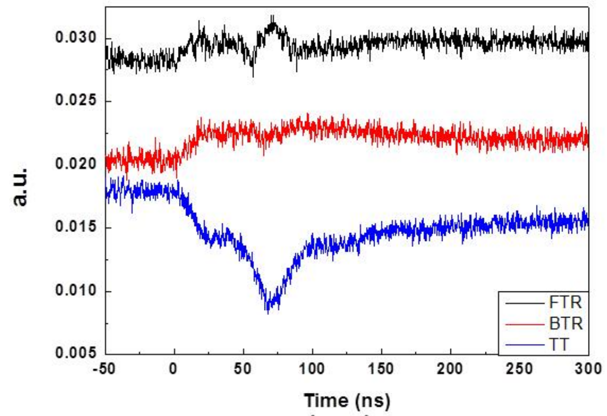

(a2)

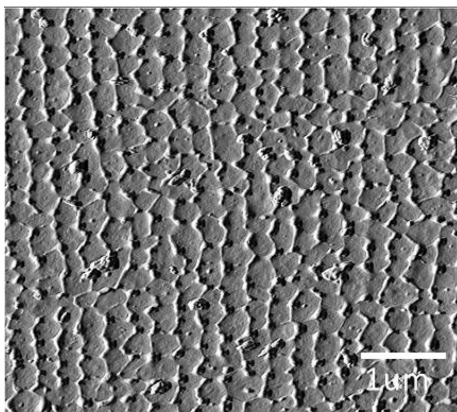

(b1)

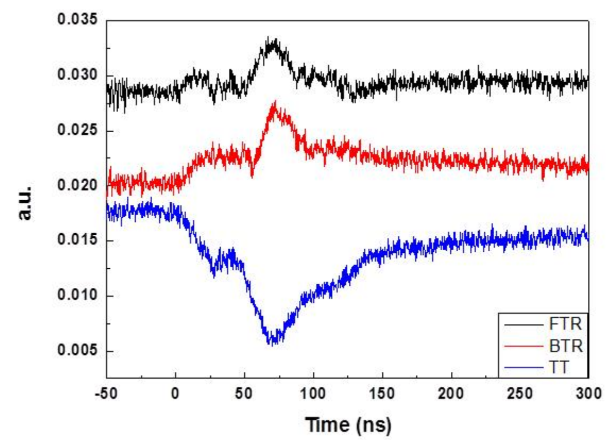

(b2)

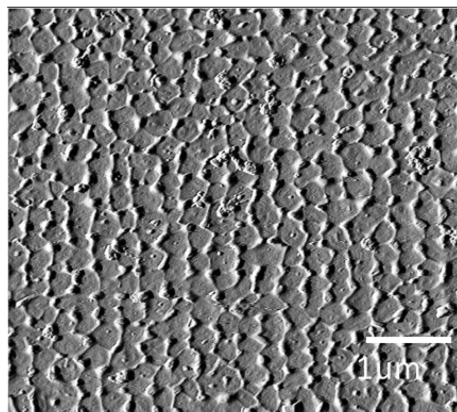

(c1)

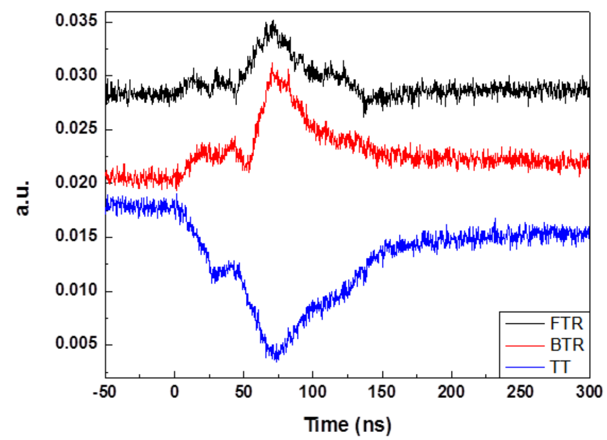

(c2)

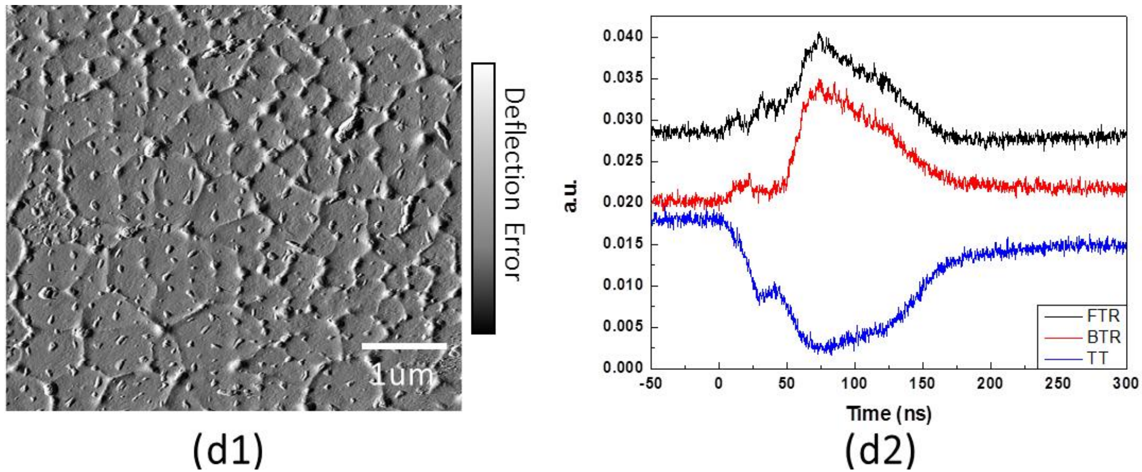

Figure 6.5: (a1) - (d1) The AFM images of the sample surfaces after irradiation under the energy conditions of 70%, 75%, 85% and 90% of CMT; (a2) - (d2) depict the corresponding transient signals. The black, red and blue colors respectively represent the FTR, BTR and TT signals. The signal data is originally collected as millivolts, but the Y-axis is presented here as arbitrary units for easier feature comparison.

6.4 Discussion

At the beginning of this chapter we mentioned that although the planarization attempt with preservation of grain structure is not successful, useful information can still be extracted. In fact, the value of this experiment comes mostly from the developed understanding of the phase transformation scenario during excimer laser irradiation of ELA-generated p-Si thin film. Thus, instead of studying the mechanism of protrusion formation, which is a relatively straightforward result of volume expansion from liquid to solid phase of Si at the end of solidification when two nearby grains impinge onto each other, our discussion focuses more on the fundamental aspects of melting and solidification in this material.

6.4.1 The Melting and Solidification Scenario

Based on the above observations of surface morphology and reflectance signal changes during excimer irradiation, we can construct a phenomenological picture of how molten material is distributed throughout the thin film. Three relevant aspects of the Si film microstructure can be identified, namely (1) the thin and dense oxide layer at the front side of the Si film forming an inert Si/oxide interface, (2) the predominantly high-angle boundaries between columnar grains, representing the high excess free energy sites and (3) another inert Si/oxide interface between the Si film and the oxide substrate. According to our group's past experience, melting prefers to initiate at high-excess free energy sites when a material is heated. From this perspective, the simultaneously occurring humps in the BTR and the FTR signals suggest that the melting first initiates at the grain boundaries, vertically penetrates through the thickness of the film along grain boundaries, and forms a vertical liquid/solid interface. Since the Si/oxide interfaces at the top and the bottom of the film are both relatively inert and inhibit the formation of liquid, the melting is likely to proceed as a lateral propagation of the liquid/solid interface from the grain boundaries towards the inside of the grains. Such 2-D melting scenario also explains the missing plateau in the FTR signal at high laser energy, as the front surface is never completely melted. Since the laser heating is input at the front surface, it would always be hotter than the bottom interface. Thus, the liquid/solid ratio should be larger at the front side than that on the bottom side, resulting in the observation that the humps in the FTR signals are always larger than those in BTR signals. The scenario of melting can be schematically drawn in a sequence from (a) to (d) in Figure 6.6 and the dimensionality of the phase transformation mechanisms presented here is

followed up in another recent work from our group.[27]

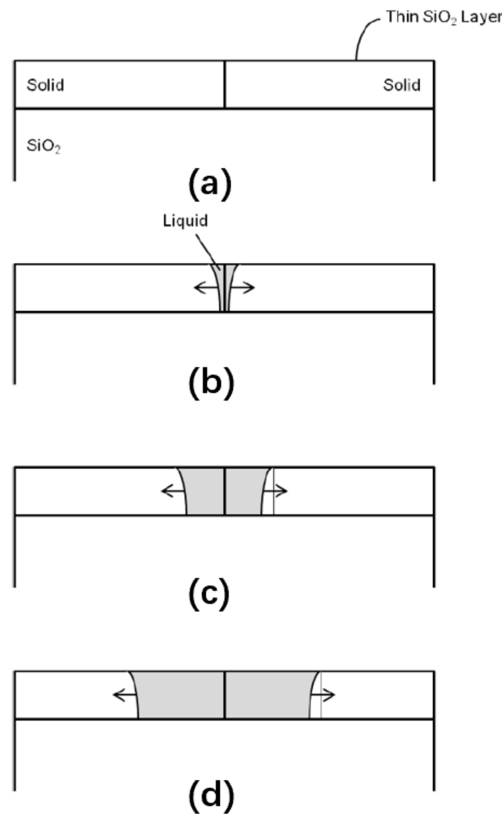

Figure 6.6: (a)-(d) phenomenological picture of the melting process sequence during excimer laser irradiation of ELA-generated polycrystalline thin films.

When the grain resolidification starts, the liquid/solid interfaces move outward from the grain interiors until they eventually impinge onto each other together, forming grain junctions. After the resolidification, the grain boundary may (as shown in Figure 6.4 (a)- (c)) or may not (as shown in Figure 6.4 (d)) form at the original location, which could be affected by various factors, including the extent of melting in this case. It should be noted that the abovementioned redistribution of laser energy caused by light diffraction can also affect the location of the newly formed grain boundaries and protrusions after resolidification. More information about the melting and solidification is presented in the following subsection via numerical simulation. The reasons

causing the appearance of the small and isolated protrusions at the flat area inside the SLG grains will be discussed in the next chapter.

6.4.2 The Numerical Simulation

In order to get a more comprehensive sense of the entire melting and solidification scenario in the ELA process, numerical simulation is performed using a software package developed in our group called nDNS. The nDNS adopts finite difference (FD) method and is designed to simulate time-resolved rapid heat flow and first-order phase transformation of materials by taking the coupled temperature-dependent, phase-dependent and material-dependent parameters into the numerical calculation. The two governing equations implemented in the software are (1) the general heat transport equation shown in Equation 6.1 and (2) the linear approximation of the interface response function shown in Equation 2.2. In the calculation, the sample geometry is meshed into cubic cells with defined material properties and temperature profile. Therefore, nDNS is capable of dealing with the nonequilibrium phase transformation process occurring in the nonequilibrium excimer-laser-induced melting and solidification, as well as to tracing the solid/liquid interface in a time-resolved manner. The time resolution is set to be nanosecond scale and the space resolution is in nanometer scale. This simulation package has also incorporated the superheating effect and preferential melting at grain boundaries.

$$c_p(\emptyset, T)\frac{dT}{dt} = \nabla \cdot (\kappa_T(\emptyset, T)\nabla T) + \dot{q}_L + \dot{q}_E \qquad (6.1)$$

The general heat transport equation where c_p is the heat capacity at constant pressure, $\emptyset$ denotes the phase, T is temperature, t denotes time, κ_T is the thermal conductivity, $\dot{q}_L$ is the rate of latent heat being absorbed or released respectively during melting or solidification, and $\dot{q}_E$ is the rate of surface heat input from the laser. Radiative and convective heat dissipations are ignored in the simulation, since the laser irradiation process is very rapid and the heat conduction into the substrate is dominant.

The simulated structure is schematically shown in Figure 6.7 where two grains are respectively colored in red and green color. Protrusions are neglected, since the simulation does not incorporate curvature and the Gibbs-Thompson effect, which is an acceptable assumption in our study focused on the melting-solidification scenario. A thin layer of silicon oxide and a sufficiently thick oxide substrate are constructed respectively at the top and bottom of the Si grains. The Si/oxide interfaces are set to be relatively inert and the grain boundary is set to be reactive and favoring melting. The vertical dimension of the Si thin film is set to be 50nm, while the direction normal to the paper is set to be infinite. The melting temperature of Si is set to be 1685K. The system is set to be adiabatic throughout the process. The laser irradiation, with the time profile the same as that used in the experiments, comes from the top. We intentionally let the laser energy focus on the right side of the front surface in order to generalize and include the possible effects as abovementioned (1) the laser energy redistribution in a nonuniform manner caused by light diffraction in the ELA process and (2) other factors that cause nonuniform melting and solidification rates among different grains such as the orientation, local curvature and size effect of a grain.

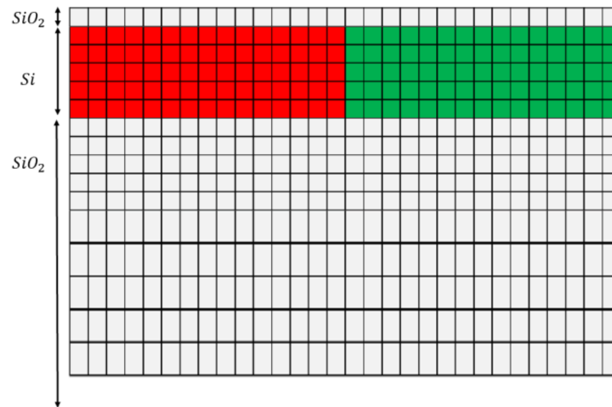

Figure 6.7: the schematic of the simulated structure, where the red and green regions are set to be two different c-Si grains forming a grain boundary in the middle.

In the simulation, we analyze and visualize the time-resolved evolutions of several distributions including the spatial profiles of the phases, spatial temperature profile, temporal laser-energy profile and temporal profiles of the melt fractions at the top, bottom and overall throughout the film during the melting and solidification process. The melt fraction is defined as the percentage of the liquid in the considered space. Several representative intermediate states are selected and presented in Figure 6.8. Figure 6.8 (a) – (f) demonstrate the situation before the laser irradiation, at the time when the laser irradiation begins, the time when melting just initiates, the time when liquid reaches the bottom of the film, the time when the liquid fraction reaches the maximum and shortly before complete resolidification. Each figure consists of three subfigures containing abundant information. Subfigures (a1) - (f1) are the vertical cross sections of the film with a vertical white dash line denoting the location of the initial grain boundary. The heat maps are used to display spatial temperature distribution at each time frame and the solid black lines denote the liquid/solid interfaces. Brighter color in the heat maps means higher temperature. Subfigures (a2) – (f2) are the plots of the temperature profiles as a function of location at the front surface (green) and the back

surface (blue) of the film at each time frame. The horizontal black dash lines in subfigures (a2) – (f2) denote the melting temperature of Si at 1685K. The four subplots in each of (a3) - (f3) describe temporal variations, and the vertical dashed line indicates the simulation time at which the spatial profiles are constructed. Temporal evolutions of the input laser pulse energy, front, bottom and overall melt fractions are presented. It can be seen from Figure 6.8 (b) that liquid does not form at the beginning of laser irradiation, since the temperature does not reach the melting temperature yet. Seen from Figure 6.8 (c), the grain boundary first melts when the local temperature at the grain boundary reaches the melting point, even though the grain-boundary location is not the first region that reaches the melting point. In fact, by then, the grain body on the right side of the boundary has already been superheated above the melting temperature by around 200K. The reasons causing the preferential melting at the grain boundaries and the superheating inside the grains are studied in detail in another recent work in our group [27]. From Figure 6.8 (d) and (f), we can see that the melting penetrates through the thickness of the film forming a vertical liquid/solid interface and the melting (or resolidification) progresses in a manner of the lateral movement of the two liquid/solid interfaces toward (or outward) the grain interior. After resolidification, the grain boundary restores at the original location, which explains the unchanged surface morphology after planarization shown in Figure 6.5 (a1) - (c1).

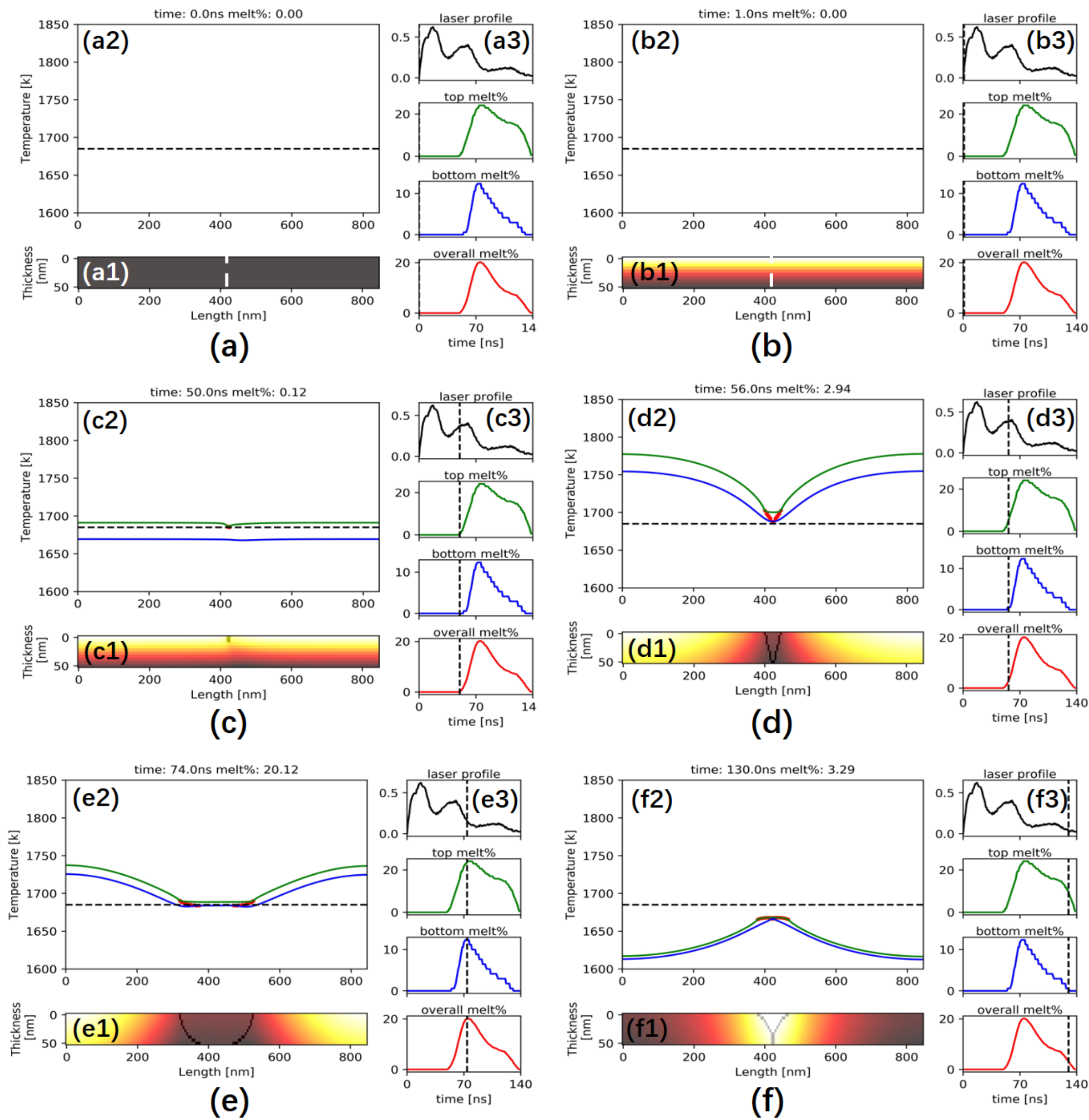

Figure 6. 8: (a)-(f) The selected representative time frames in the phase transformation simulation (a) before laser irradiation, (b) at the beginning of laser irradiation, (c) the starting point of melting, (d) when the formed liquid reaches the bottom, (e) when the melting reaches the maximum, and (f) some time before complete resolidification. After resolidification, the grain boundary restores at the original location.

6.5 Summary

In this chapter, we conduct a set of systematic experiments initially attempting to planarize the surface protrusions on the ELA-generated p-Si thin film via single-shot excimer laser irradiation at 70%, 75%, 85% and 90% of the film's CMT. The *in-situ* optical probing system is set up to collect spatiotemporal information about the phase transformation during the laser irradiation by recording the FTR, BTR and TT signals. The surface morphologies of the p-Si thin films irradiated under different laser-energy conditions are characterized by an AFM. A phenomenological picture of the melting and solidification scenario is logically deduced and simulated numerically. We conclude that it involves lateral movement of vertical liquid/solid interface that initiates at grain boundaries and proceeds toward (or outward) the grain interiors during melting (or solidification), which we call a 2-D melting phenomenon. The findings based on the set of experiments in this chapter along with the results of the systematic microstructure analysis in Chapter 5 helps us form a better understanding of the microstructure evolution both from the microstructure-analysis point of view and the microscopic phase-transition point of view during the ELA process.

Chapter 7

Surface Planarization of BHF-treated ELA Si Thin Films

Based on the understanding developed in the above chapter, we repeat the planarization experiments using ELA samples treated with buffered hydrofluoric acid (BHF). After BHF treatment, the thin oxide layer on the front surface is completely removed, exposing the free surface that has affinity for melting comparable to the grain boundaries. The energy window of the laser irradiation is chosen to be similar as that used in the planarization experiments presented in Chapter 6. AFM and in-situ optical probing system are still used to characterize the surface morphology and collect the spatiotemporal information of the melting and solidification process. Surface planarization has been successfully achieved maximally at 41.8% in this set of experiments, confirming the ideas presented in the discussion of Chapter 6. By comparing the experimental results gained in this chapter and those in Chapter 6, we form more understanding about the phase transformation

properties of the ELA-generated p-Si thin films and the influence of the surface oxide layer during the excimer-laser induced melting and solidification process.

7.1 Planarization Experiments

Before laser irradiation, the as-is ELA-generated samples are first dipped into BHF solution for sufficiently long time (several minutes) ensure the complete removal of the oxide layer from the front surface. Then the planarization experiments, which are the same as those done in Chapter 6, are conducted on the BHF-treated samples.

7.1.1 Results and Analysis

The energies of the excimer laser are respectively chosen to be 70%, 77%, 82% and 88% of the CMT, and the planarization results are shown the in Figure 7.1 where Figures 7.1 (a) – (d) are the AFM images of the surface morphology respectively resulted from the four laser-energy conditions, while Figure 7.1 (e) plots the RMS surface roughness after irradiation. From the AFM images of Figures 7.1 (a) – (c) and the corresponding RMS surface roughness we can see that the protrusions become shallower and less periodic after planarization compared to those in the original sample. The surface roughness respectively reduces from the original 13.75nm to 9.1nm, 8.4nm and 7.5nm, as found in Figure 7.1 (e). For the energy condition of 88% CMT, as shown in Figure 7.1 (d), large super-lateral growth (SLG) grains can be identified along with the newly formed prominent protrusions. Comparing

Figures 7.1 (a) – (c) and Figures 6.4 (a) – (c), we can easily tell that the effect of planarization is much better for the BHF-treated samples than for the oxide-capped samples. We also recognize that there are no small and isolated protrusions at high laser energy condition shown in Figure 7.1 (d), like those persisting in Figure 6.4 (d). The bouncing up of the RMS roughness under high laser-energy condition of 88% CMT is attributed to the newly formed prominent protrusions at the boundaries of the SLG grains. The maximum planarization is achieved at 41.8% of the original RMS surface roughness under the energy condition of 82% CMT.

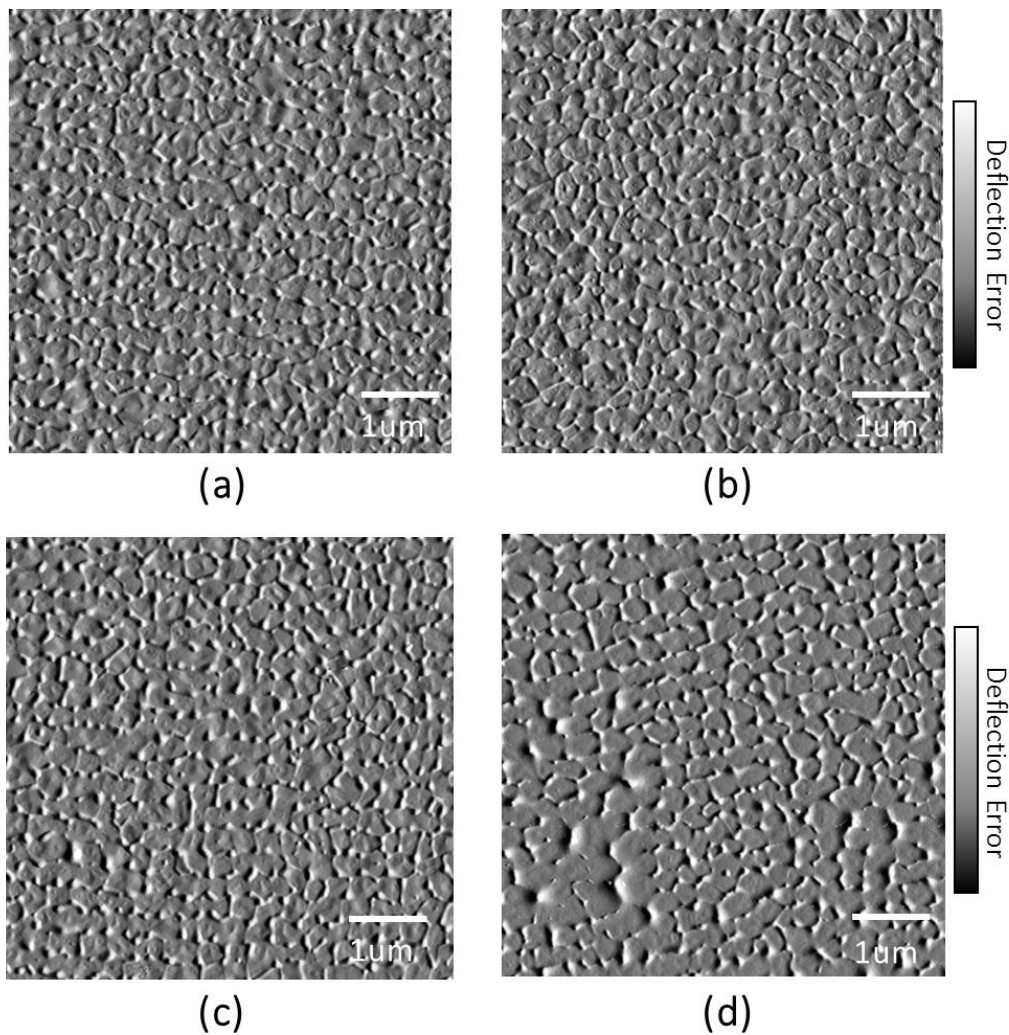

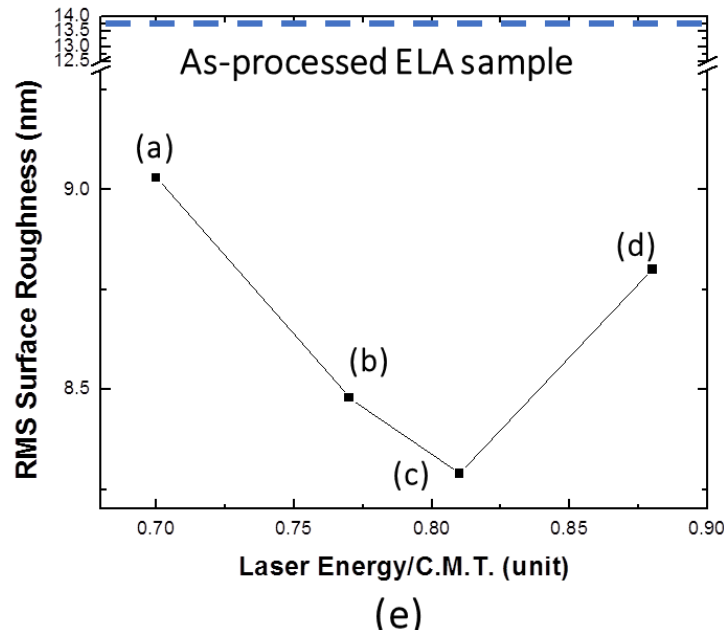

(e)

Figure 7.1: (a) – (d) AMF images of the surface morphology after planarization respectively under the energy conditions of 70%, 77%, 82% and 88% of the CMT, and (e) the plot of the corresponding RMS surface roughness. The RMS surface roughness respectively reduces from the original 13.75nm (blue dashed line) to 9.1nm, 8.4nm and 7.5nm under the first three energy conditions. The maximum reduction reaches 41.8%.

7.1.2 Transient Reflectance and Transmittance Analysis

The recorded front-side reflectance FTR (black color), back-side reflectance BTR (red color) and transient transmittance TT (blue color) signals for the four laser-energy conditions are plotted in the Figures 7.2 (a2) – (d2). It can be seen that, for all of the four laser-energy conditions, the BTR signals do not follow with FTR signals as well as those shown in Figures 6.5 (a2) – (d2). Based on our previous experience, the oscillations occurring right before the ramp up of the BTR signals in the Figures 7.2 (a2) – (d2) are caused by the diode laser interference as the probe light gets partially reflected from the bottom surface of the formed liquid layer at the front surface. Such

observations are the clear evidence showing that the melting and solidification scenario of the BHF-treated ELA films is qualitatively different from the case in the oxide-capped samples, even though the laser-energy conditions are similar.

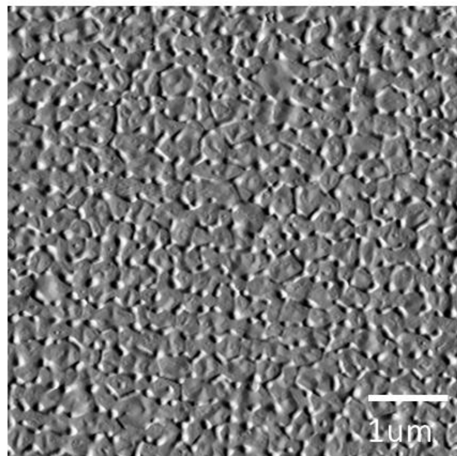

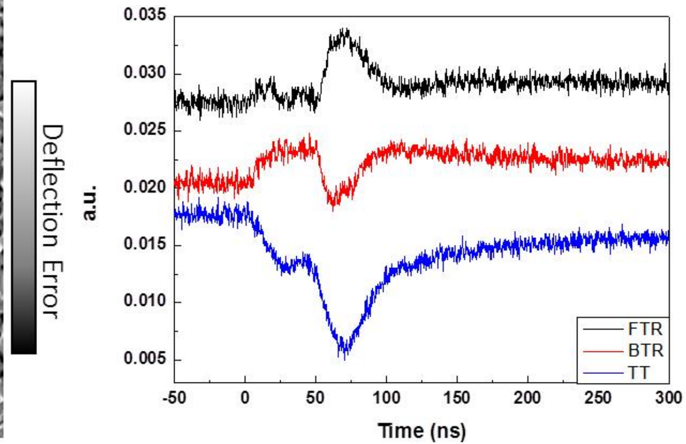

(a1) (a2)

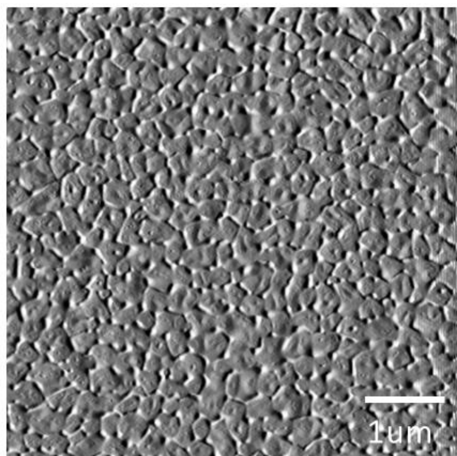

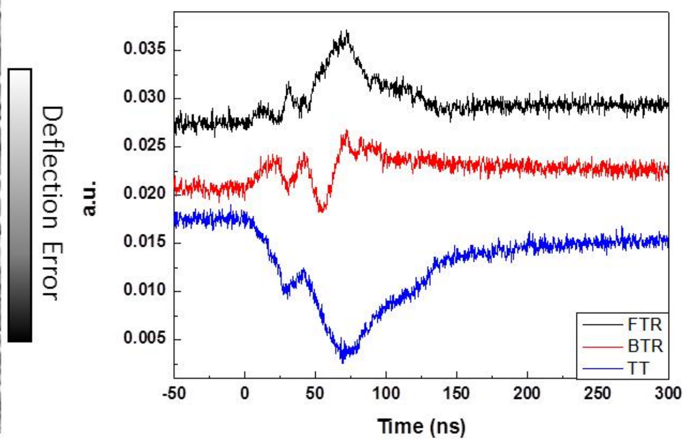

(b1) (b2)

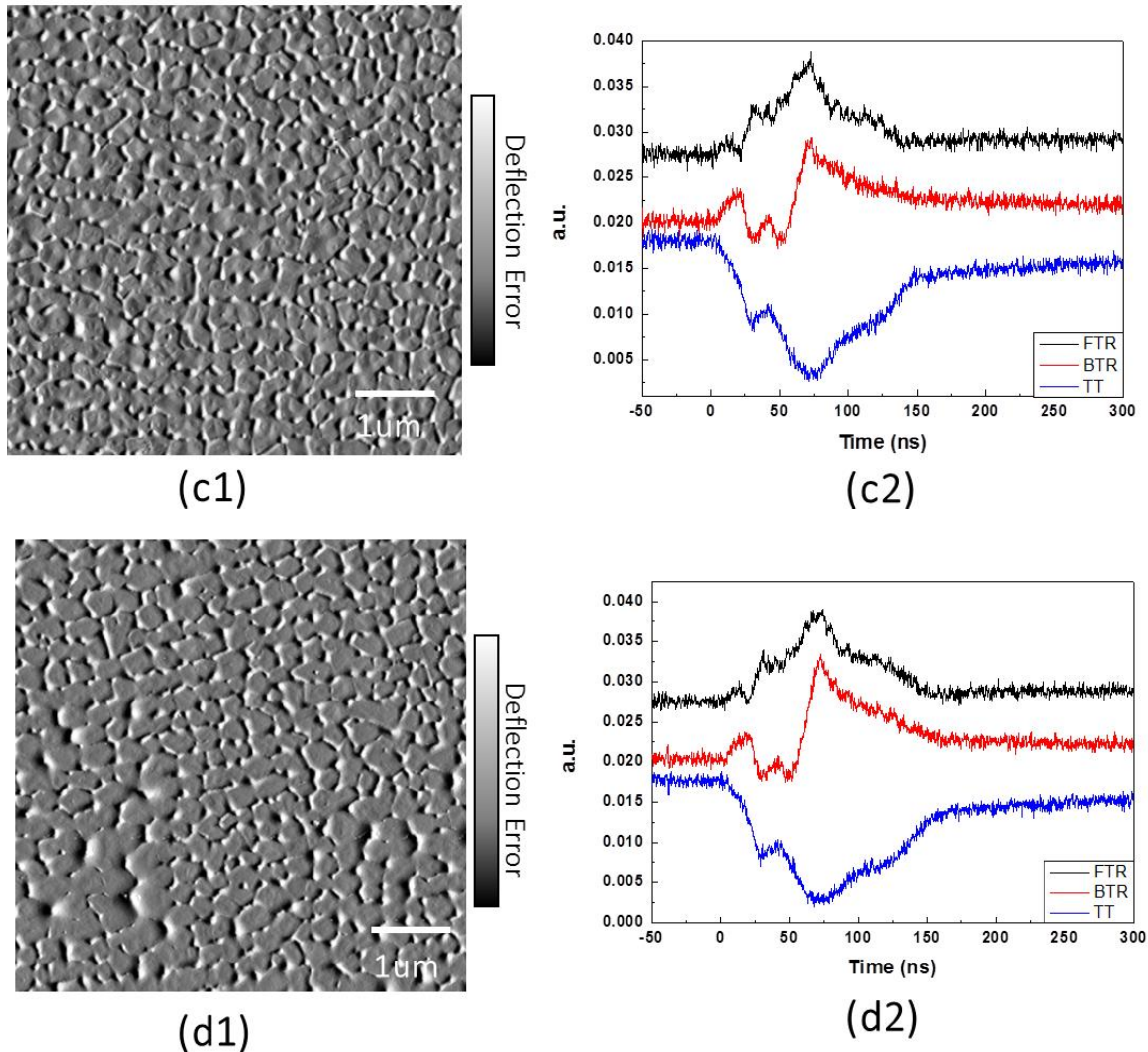

Figure 7.2: (a1) – (d1) AFM images of the surface morphology after planarization respectively under the laser-energy conditions of 70%, 77%, 82% and 88% of the CMT, and (a2) – (d2) the corresponding FTR, BTR and TT signals recorded by the in-situ optical probing system. The black color, red color and blue colors respectively represent the FTR, BTR and TT signals.

7.2 Discussion

The results obtained during the planarization experiments of the BHF-treated samples are quite different from those presented in chapter 6. Considerable extent of planarization with the maximum reduction of RMS

surface roughness at 41.8% has been achieved on the oxide-free samples here, all the while using the same laser energy that had produced negative results before. The surface morphology and transient signals obtained from the BHF-treated samples are also clearly different from those in the oxide-capped samples. This indicates that we are dealing with a different melting and solidification scenario here. Unlike in the oxide-capped samples, small and isolated protrusions also do not appear on the flat surface inside the SLG grains of the BHF-treated samples after irradiation with high laser energy. All of these above experimental differences between the BHF-treated samples and the oxide-capped ones should be attributed to the influence of the surface oxide layer upon melting and solidification, since the removal of the surface oxide layer is the only experiment modification. Based on the observation in *A. Bosseboeuf*'s report and the observations in chapter 6 and 7, we can categorize the melting and solidification scenarios of the c-Si (after etching leaving free surface), BHF-treated (free surface) and the as-is ELA (oxide-capped) p-Si thin films during planarization as primarily one-dimensional (1-D) or two-dimensional (2-D). The melting and solidification scenarios of the reported c-Si condition, the BHF-treated condition and the as-is ELA condition are respectively shown in Figure 7.3 (a1) – (a3), Figure 7.3 (b1) – (b3) and Figure 7.3 (c1) – (c3). For the c-Si condition, the free surface is substantially molten, forming a continuously liquid layer with the surface tension of the liquid driving the surface to flatten. The subsequent solidification proceeds in a planar fashion, i.e. through the vertical 1-D growth of solid leading to the smoothed surface after planarization. For the free-surface ELA-film condition, grain boundary is also present in addition to the free surface. The free surface and the grain boundary are both excess free energy-rich sites, and the excess free energy density of the former is higher

than that of the latter [83][84][85]. Thus, upon laser irradiation, melting proceeds at both the free surface and the grain boundaries, but the free surface melts more aggressively than the grain boundaries. Even though the liquid formed on the free surface does not form a continuous layer (evidenced from the transient signal in Figure 7.2), the surface tension still drives to flatten the surface to some extent. The liquid at the grain boundaries leads to the redevelopment of protrusions as a consequence of mass accumulation resulting from the phase-change associated density change during solidification. At the properly tuned laser energy and the surface tension effect of the formed liquid, the redeveloped protrusions are not as tall as the original ones. For the as-is ELA condition, the passivated oxide/Si surface interface prevents surface from melting, resulting in a 2-D melting (evidenced from transient signals in Figure 6.5) at grain boundaries (the only excess free energy rich sites in as-is condition) and results in the superheating of about 200K inside the grains, estimated from the numerical simulation. Besides, the surface oxide retards the mass flow of the molten material at the protrusions, causing them to redevelop at the original locations with unreduced height.

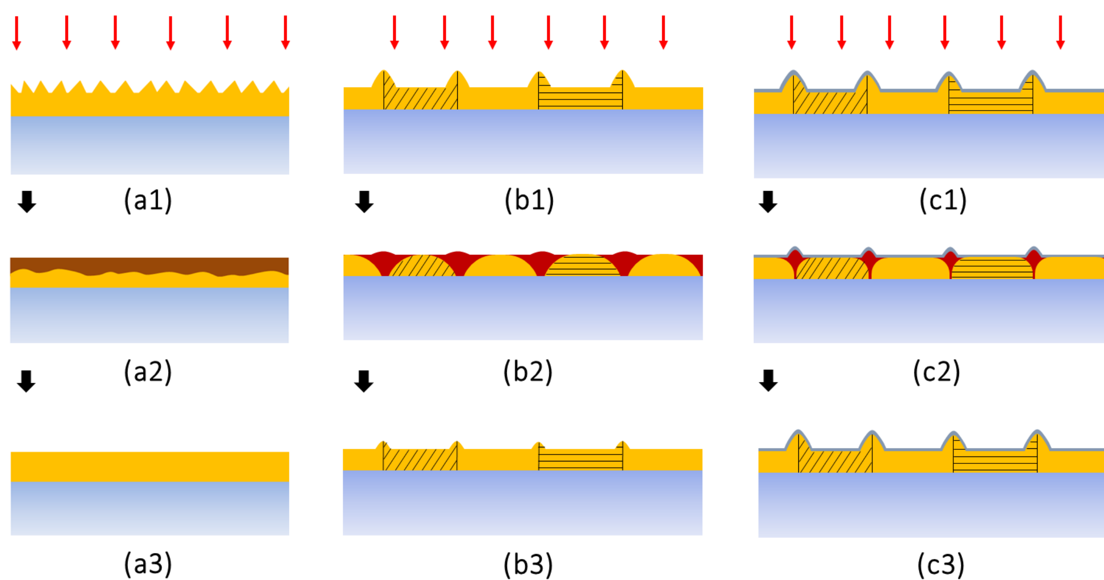

Figure 7.3: (a1) – (a3), (b1) – (b3) and (c1) – (c3) schematic diagrams of the melting and solidification processes during planarization experiments respectively of the reported c-Si condition (free surface), the BHF-treated ELA film (free surface) and the as-is ELA film (oxide-capped). The descriptions of and the reasons causing the different melting and solidification scenarios are discussed in the above paragraph.

7.3 Summary

In this chapter, we conducted planarization experiments on BHF-treated ELA samples from which the surface oxide layer had been completely removed. Considerable extent of planarization was achieved with the maximum protrusion reduction around 41.8%. The surface morphology and the transient signals obtained in the work of this chapter are quite different from those presented in Chapter 6, leading us to further evaluate the influence of the surface oxide on the melting and solidification process. The influence of the surface oxide is concluded as two-fold, namely (1) to passivate the free surface of Si and to induce superheating inside the grains, and (2) to retard the mass transport of liquid Si. Based on this understanding, we present a comprehensive picture of the melting and solidification scenario of both BHF-treated (free surface) and as-is (oxide capped) ELA samples. The understanding formed in this chapter would help scientists and engineers to better appreciate the phase transformation mechanisms and protrusion formation occurring in the ELA process and the material properties of the ELA-generated p-Si thin films.

Chapter 8

Conclusions

8.1 Conclusion

The excimer-laser annealing of Si thin film is currently an irreplaceable technology used in the manufacturing of the TFT backplane material in modern advanced LCD and OLED displays, due to its low-thermal-budget substrate compatibility, relatively low cost and good scalability. The ELA-generated p-Si thin film consisting of relatively uniform grains satisfies the current demand of the high-resolution display by providing high carrier mobility (~200cm^2/Vs) with acceptable cost. For a long time, the research of ELA p-Si has been obsessively focused on directly studying the influence of the miscellaneous technological details, such as the laser energy, processing parameters and ambient atmosphere ingredients, on the electrical characteristics of devices fabricated with the ELA films, but missed the link (the microstructure and surface morphology) connecting all of them. Besides, the efforts of improving ELA material were, unfortunately, merely devoted to achieving more uniform grains over a large scale, while the local microstructure variation in the device length scale was omitted, which in fact substantially affects the performance of the subsequently manufactured devices. In addition, the very limited previous studies of the fundamental

phase transformation mechanism in the ELA process are only based on individual grains, so they fail to discuss how the numerous ELA grains collectively evolve during the process.

In the work of this thesis, the ELA microstructure and its evolution during the multiple laser shots are unprecedentedly rigorously and systematically analyzed on a statistically significant number of grains over a large ELA-film area. In order to realize such analyses, an image-processing-based grain boundary extraction program (GB extraction program) is developed based on the theory of Watershed Segmentation Algorithm, which can precisely and efficiently distill the grain boundary maps (GB map) from the TEM images of the ELA microstructure. Based on the availability of GB maps, the local microstructure analysis (LMA) scheme is proposed and adopted to capture the local microstructure variation in the device length scale by considering the device geometry and orientation. Fast Fourier Transform (FFT) is used to quantitatively identify the periodicity existing in the grain boundary distribution. ELA p-Si thin films are generated using different number of excimer-laser shots (i.e. 5, 10, 15, 20, 25 and 30 shots) for the microstructure evolution analysis. From the analysis, we find that (1) small grains disappear and the remaining grains generally enlarge during the repeated laser irradiations; (2) the grain-size distribution fits well with the log-normal distribution for a small shot number and deviates away from the log-normal distribution as the shot number increases; (3) periodicity starts to appear and becomes more pronounced in the grain boundary distribution when the shot number increases; (4) although a statistical look at the grain sizes might suggest that the ELA microstructure is uniform, significant local non-uniformity may exist; (5) such nonuniformity magnifies either with the decrease of the device size, the enlargement of grain size or the increase of

periodicity; (6) the local nonuniformity varies with the change of the device orientation and there are certain orientations at which the local nonuniformity could be minimized. The finding (1) reflects the 2-D melting behavior of grains during melting and solidification, which is identified in the planarization experiments. The findings (2) and (3) are the results of the light diffraction effect and the subsequent nonuniform laser energy distribution in the ELA process. The energy redistribution caused by periodic protrusions abates the stochastic grain-growth process, leading to the deviation of grain-size distribution away from log-normal. The findings (1)-(3) and the analysis results in Chapter 5 clearly capture the details how the microstructure evolves during the multiple laser shots during the ELA process. The findings (4)-(6) quantitatively capture the local microstructure nonuniformity and further the understanding of the connection between the local microstructure nonuniformity and the performance consistency of devices fabricated on different locations of the film.

In the attempt of surface planarization, we conduct experiments respectively using as-is (oxide-capped) ELA-generated films and BHF-treated (free surface) films. Successful surface planarization was achieved using BHF-treated samples with a maximum reduction of the RMS surface roughness of 41.8% and major preservation of the original microstructure of the ELA film, while, on the contrary, the surface protrusions become even more prominent after irradiation of the as-is (oxide-capped) samples. By comparing the planarization results, we deduce a two-fold influence of the surface oxide layer in the laser-induced melting and solidification of the p-Si thin film, which involves (1) preventing the front surface from melting via surface passivation and (2) retarding the mass transport of liquid Si. Besides, we recognize the highly two-dimensional (2-D) melting-and-solidification

behavior of the ELA grains upon laser irradiation, which is very different from the 1-D planar melting scenario encountered in the c-Si material. In the 2-D case, melting happens at the grain boundaries, forming vertical liquid/solid interface throughout the entire thickness of the film. The melting and subsequent solidification proceed via lateral movement of liquid/solid interface. Meanwhile, the top oxide/Si interface that receives laser irradiation and has the highest temperature surprisingly does not melt. Numerical simulation is performed to more vividly present such melting and solidification scenario and verify our logical deduction. In addition, the simulation also captures the superheating of around 200K above the melting temperature of Si in the grain interiors during 2-D melting.

The contribution of this thesis can be concluded as two-fold. On one hand, the tools and schemes developed to analyze the microstructure of the ELA-generated p-Si thin films can be generalized to research of other materials, being most applicable when the geometry and arrangement of grains and particles are of interest. On the other hand, the understanding gained in this work can be recognized as providing valuable implications for the scientific study of the phase transformation mechanisms of general polycrystalline materials as well as providing effective approaches and clear clues for the engineers when they study the ELA technique and the generated material.

8.2 Suggestions for the Future Work

We have demonstrated the existence of the local microstructure nonuniformity, and discussed how the local nonuniformity affects the

performance consistency of devices, as well as provided effective tools to analyze the ELA microstructure. Further work may thus include optimizing the size and orientation of TFTs fabricated with the ELA films. We suggest engineers to try to optimize the TFT performance by adjusting the size and orientation of TFTs with respect to their currently manufactured ELA films. We believe that such attempt is likely to result in improving the product performance with a relatively low implementation cost, which could benefit the related industry.

The understanding gained in this work can also be leveraged to guide the improvement of the TFT backplane material and the design of the microelectronic elements in the future. With the tendency to decrease the device size, the industry might eventually face a point where the device-size-dependent local microstructure nonuniformity is causing too much performance inconsistency. Therefore, we suggest to probe the limit of the current ELA-generated p-Si thin films using sufficiently small TFTs in order to provide the industry directions to further advance the TFT backplane material and device design.

The approaches we developed and effectively demonstrated in the study of the microstructure and surface morphology of the ELA-generated p-Si can also be adopted in the investigation of other materials. LMA may be directly applied for an in-depth study of promising processes such as sequential-lateral-solidification (SLS) of p-Si thin films [14], mixed-phase-solidification (MPS) of large-grained p-Si thin film [86] and the currently emerging spot-beam-crystallization (SBC) of p-Si thin film [15]. Furthermore, the microstructure of other polycrystalline materials involved in important modern technologies such as 3D printing can also be properly analyzed and better understood using our methods.

Bibliography

[1]. T. C. Chang, Y. C. Tsao, P. H. Chen, M. C. Tai, S. P. Huang, W. C. Su, and G. F. Chen, "Flexible low-temperature polycrystalline silicon thin-film transistors," Materials Today Advances 5, 100040 (2020).

[2]. C. Y. Yap, C. Chua, Z. Dong, Z. Liu, D. Zhang, L. E. Loh, and S. L. Sing, "Review of selective laser melting: Materials and applications," Applied Physics Reviews 2, 041101 (2015).

[3]. T. D. Ngo, A. Kashani, G. Imbalzano, K. T. Q. Nguyen, and D. Hui, "Additive manufacturing (3D printing): A review of materials, methods, applications and challenges," Composites Part B: Engineering 143, 172-196 (2018).

[4]. P. C. Collins, D. A. Brice, P. Samimi, I. Ghamarian, and H. L. Fraser, "Microstructural Control of Additively Manufactured Metallic Materials," Annual Review of Materials Research 46, 63-91 (2016).

[5]. H. Xing, B. Zou, S. Li, and X. Fu, "Study on surface quality, precision and mechanical properties of 3D printed ZrO2 ceramic components by laser scanning stereolithography," Ceramics International 43, 16340-16347 (2017).

[6]. K. N. Amato, S. M. Gaytan, L. E. Murr, E. Martinez, P. W. Shindo, J. Hernandez, S. Collins, and F. Medina, "Microstructures and mechanical behavior of Inconel 718 fabricated by selective laser melting," Acta Materialia 60, 2229-2239 (2012).

[7]. T. C. Blair, and J. G. McPherson, "Grain-size and textural classification of coarse sedimentary particles," Journal of Sedimentary Research 69,

6-19 (1999).

[8]. Cremona, Mauricio, C. Scavarda Do, Prioli, Nunes, Zanette, Caride, and Albuquerque, "Grain size distribution analysis in polycrystalline LiF thin films by mathematical morphology techniques on AFM images and X-ray diffraction data," Journal of Microscopy 197, 260-267 (2000).

[9]. N. X. Sun, and K. Lu, "Grain-size limit of polycrystalline materials," Physical Review B 59, 5987-5989 (1999).

[10]. B. Raeisinia, C. Sinclair, W. Poole, and C. Tomé, "On the impact of grain size distribution on the plastic behaviour of polycrystalline metals," Modelling and Simulation in Materials Science and Engineering 16, 025001 (2008).

[11]. N. G. Basov, V. A. Danilychev, Y. M. Popov, and D. D. Khodkevich, "Laser Operating in the Vacuum Region of the Spectrum by Excitation of Liquid Xenon with an Electron Beam," Soviet Journal of Experimental and Theoretical Physics Letters 12, 329 (1970).

[12]. G. Fortunato, L. Mariucci, R. Carluccio, A. Pecora, and V. Foglietti, "Excimer laser crystallization techniques for polysilicon TFTs," Applied Surface Science 154-155, 95-104 (2000).

[13]. L. Mariucci, A. Pecora, R. Carluccio, and G. Fortunato, "Advanced excimer laser crystallization techniques," Thin Solid Films 383, 39-44 (2001).

[14]. R. S. Sposili, and J. S. Im, "Sequential lateral solidification of thin silicon films on SiO2," Applied Physics Letters 69, 2864-2866 (1996).

[15]. J. S. Im, R. Song, V. K. Wong, W. Pan, I. Choi, and M. Yu, "57-5: Invited Paper: Excimer Laser Annealing and Spot-Beam Crystallization of Si Films for Advanced Displays," SID Symposium Digest of Technical Papers 49, 762-763 (2018).

[16]. N. Matsuo, A. Heya, and H. Hamada, "Review—Technology Trends of Poly-Si TFTs from the Viewpoints of Crystallization and Device Performance," ECS Journal of Solid State Science and Technology 8, P239-P252 (2019).

[17]. M. Sobey, K. Schmidt, B. Turk, and R. Paetzel, "8.2: Invited Paper: Status and Future Promise of Excimer Laser Annealing for LTPS on Large Glass Substrates," SID Symposium Digest of Technical Papers 45, 79-82 (2014).

[18]. F. Okumura, K. Sera, H. Tanabe, K. Yuda, and H. Okumura, "Excimer Laser Annealed Poly-Si TFT Technologies," MRS Proceedings 377, 877 (1995).

[19]. M. Stehle, "Excimer laser treatment for large surface," Journal of Non-Crystalline Solids 218, 218-222 (1997).

[20]. J. Im, "A New Excimer-Laser-Annealing Method for Manufacturing Large OLED Displays," MRS Proceedings 1426 (2012).

[21]. P. C. van der Wilt, "13.1: Invited Paper: Excimer-Laser Annealing: Microstructure Evolution and a Novel Characterization Technique," SID Symposium Digest of Technical Papers 45, 149-152 (2014).

[22]. D. K. Fork, G. B. Anderson, J. B. Boyce, R. I. Johnson, and P. Mei, "Capillary waves in pulsed excimer laser crystallized amorphous silicon," Applied Physics Letters 68, 2138-2140 (1996).

[23]. J. Bonse, S. Höhm, S. V. Kirner, A. Rosenfeld, and J. Krüger, "Laser-Induced Periodic Surface Structures— A Scientific Evergreen," IEEE Journal of Selected Topics in Quantum Electronics 23, 1 (2017).

[24]. T. Sasaoka, M. Sekiya, A. Yumoto, J. Yamada, T. Hirano, Y. Iwase, T. Yamada, T. Ishibashi, T. Mori, M. Asano, S. Tamura, and T. Urabe, "24.4L: Late-News Paper: A 13.0-inch AM-OLED Display with Top

Emitting Structure and Adaptive Current Mode Programmed Pixel Circuit (TAC)," SID Symposium Digest of Technical Papers 32, 384-387 (2001).

[25]. R. L. Wisnieff, and J. J. Ritsko, "Electronic displays for information technology," IBM Journal of Research and Development 44, 409-422 (2000).

[26]. L. Faraone, "Surface Roughness and Electrical Conduction of Oxide/Polysilicon Interfaces," Journal of The Electrochemical Society 133, 1410 (1986).

[27]. V. K. Wong, "Pulsed-Laser-Induced Melting in Polycrystalline Si Films on SiO2," in Department of Applied Physics and Mathematics(Columbia University, New York, 2017).

[28]. T. Sameshima, S. Usui, and M. Sekiya, "XeCl Excimer laser annealing used in the fabrication of poly-Si TFT's," IEEE Electron Device Letters 7, 276-278 (1986).

[29]. T. Sameshima, M. Hara, and S. Usui, "XeCl Excimer Laser Annealing Used to Fabricate Poly-Si TFT's," Japanese Journal of Applied Physics 28, 1789-1793 (1989).

[30]. M. Miyasaka, and J. Stoemenos, "Excimer laser annealing of amorphous and solid-phase-crystallized silicon films," Journal of Applied Physics 86, 5556-5565 (1999).

[31]. T. Sameshima, and S. Usui, "Laser beam shaping system for semiconductor processing," Optics Communications 88, 59-62 (1992).

[32]. T. Sameshima, K. Saitoh, N. Aoyama, S. Higashi, M. Kondo, and A. Matsuda, "Electrical Properties of Pulsed Laser Crystallized Silicon Films," Japanese Journal of Applied Physics 38, 1892-1897 (1999).

[33]. G. Fortunato, A. Pecora, L. Maiolo, M. Cuscuna, D. Simeone, A.

Minotti, and L. Mariucci, "Excimer Laser Annealing for Low-Temperature Polysilicon Thin Film Transistor Fabrication on Plastic Substrates," in 2007 15th International Conference on Advanced Thermal Processing of Semiconductors(2007), pp. 301-305.

[34]. E. P. Donovan, F. Spaepen, D. Turnbull, J. M. Poate, and D. C. Jacobson, "Calorimetric studies of crystallization and relaxation of amorphous Si and Ge prepared by ion implantation," Journal of Applied Physics 57, 1795-1804 (1985).

[35]. G. Jaeger, "The Ehrenfest Classification of Phase Transitions: Introduction and Evolution," Archive for History of Exact Sciences 53, 51-81 (1998).

[36]. F. Spaepen, and D. Turnbull, "Chapter 2 - Crystallization Processes," in Laser Annealing of Semiconductors, J. M. Poate, and J. W. Mayer, eds. (Academic Press, 1982), pp. 15-42.

[37]. P. A. Stolk, A. Polman, and W. C. Sinke, "Experimental test of kinetic theories for heterogeneous freezing in silicon," Physical Review B 47, 5-13 (1993).

[38]. P. Buffat, and J. P. Borel, "Size effect on the melting temperature of gold particles," Physical Review A 13, 2287-2298 (1976).

[39]. C. G. K, "The Scientific Papers of J. Willard Gibbs," Nature 75, 361-362 (1907).

[40]. M. Allmen, and A. Blatter, Laser-Beam Interactions with Materials: Physical Principles and Applications (Springer Berlin Heidelberg, 2013).

[41]. H. Kaki, and S. Horita, "Periodic grain-boundary formation in a poly-Si thin film crystallized by linearly polarized Nd:YAG pulse laser with an oblique incident angle," Journal of Applied Physics 97, 014904

(2004).

[42]. J. S. Im, H. J. Kim, and M. O. Thompson, "Phase transformation mechanisms involved in excimer laser crystallization of amorphous silicon films," Applied Physics Letters 63, 1969-1971 (1993).

[43]. H. Watanabe, H. Miki, S. Sugai, K. Kawasaki, and T. Kioka, "Crystallization Process of Polycrystalline Silicon by KrF Excimer Laser Annealing," Japanese Journal of Applied Physics 33, 4491-4498 (1994).

[44]. C. W. White, P. S. Peercy, and M. R. Society, Laser and electron beam processing of materials (Academic Press, 1980).

[45]. Q. Hu, "Dynamics of Melt-mediated Crystallization of Amorphous Silicon Films," in Department Of Chemistry(Columbia University, New Yor, 2011).

[46]. J. G. Fossum, A. Ortiz-Conde, H. Shichijo, and S. K. Banerjee, "Anomalous leakage current in LPCVD PolySilicon MOSFET's," IEEE Transactions on Electron Devices 32, 1878-1884 (1985).

[47]. M. R. Murti, and K. V. Reddy, "Grain Boundary Effects on the Carrier Mobility of Polysilicon," physica status solidi (a) 119, 237-240 (1990).

[48]. M. C. Jun, Y. S. Kim, M. K. Han, J. W. Kim, and K. B. Kim, "Polycrystalline silicon oxidation method improving surface roughness at the oxide/polycrystalline silicon interface," Applied Physics Letters 66, 2206-2208 (1995).

[49]. T. Sameshima, "Laser beam application to thin film transistors," Applied Surface Science 96-98, 352-358 (1996).

[50]. C. T. Angelis, C. A. Dimitriadis, M. Miyasaka, F. V. Farmakis, G. Kamarinos, J. Brini, and J. Stoemenos, "Effect of excimer laser annealing on the structural and electrical properties of polycrystalline

silicon thin-film transistors," Journal of Applied Physics 86, 4600-4606 (1999).

[51]. L. Chen, J. Miao, L. Guo, and R. Lin, "Control of stress in highly doped polysilicon multi-layer diaphragm structure," Surface and Coatings Technology 141, 96-102 (2001).

[52]. T. Sameshima, "Laser crystallization for large-area electronics," Applied Physics A 96, 137-144 (2009).

[53]. H. Kuriyama, S. Kiyama, S. Noguchi, T. Kuwahara, S. Ishida, T. Nohda, K. Sano, H. Iwata, H. Kawata, M. Osumi, S. Tsuda, S. Nakano, and Y. Kuwano, "Enlargement of Poly-Si Film Grain Size by Excimer Laser Annealing and Its Application to High-Performance Poly-Si Thin Film Transistor," Japanese Journal of Applied Physics 30, 3700-3703 (1991).

[54]. T. Sameshima, and S. Usui, "Pulsed laser-induced melting followed by quenching of silicon films," Journal of Applied Physics 74, 6592-6598 (1993).

[55]. K. Suga, M. Chida, A. Hara, Y. Mishima, and N. Sasaki, "The effects of laser annealing ambient and the number of laser shots on the morphology of poly-Si films," Electronics and Communications in Japan (Part II: Electronics) 86, 42-50 (2003).

[56]. A. M. Marmorstein, A. T. Voutsas, and R. Solanki, "Effect of multiple scans and granular defects on excimer laser annealed polysilicon TFTs," Solid-State Electronics 43, 305-313 (1999).

[57]. A. Marmorstein, A. T. Voutsas, and R. Solanki, "A systematic study and optimization of parameters affecting grain size and surface roughness in excimer laser annealed polysilicon thin films," Journal of Applied Physics 82, 4303-4309 (1997).

[58]. S. Kenkichi, S. Masakazu, T. Michiko, H. Nobuaki, and T. Takao, "Correlation between power density fluctuation and grain size distribution of laser-annealed polycrystalline silicon," in Proc.SPIE(1999).

[59]. E. Machida, M. Horita, Y. Ishikawa, Y. Uraoka, and H. Ikenoue, "Crystallization to polycrystalline silicon thin film and simultaneous inactivation of electrical defects by underwater laser annealing," Applied Physics Letters 101, 252106 (2012).

[60]. C.-W. Han, J.-S. Park, H.-S. Choi, T.-S. Kim, Y.-H. Shin, H.-J. Shin, M.-J. Lim, B.-C. Kim, H.-S. Kim, B.-S. Kim, Y.-H. Tak, C.-H. Oh, S.-Y. Cha, and B.-C. Ahn, "Advanced technologies for UHD curved OLED TV," Journal of the Society for Information Display 22, 552-563 (2014).

[61]. H.-J. Shin, S. Takasugi, K.-M. Park, S.-H. Choi, Y.-S. Jeong, B.-C. Song, H.-S. Kim, C.-H. Oh, and B.-C. Ahn, "7.1: Invited Paper: Novel OLED Display Technologies for Large-Size UHD OLED TVs," SID Symposium Digest of Technical Papers 46, 53-56 (2015).

[62]. P. M. Fauchet, D. Hulin, R. Vanderhaghen, A. Mourchid, and W. L. Nighan, "The properties of free carriers in amorphous silicon," Journal of Non-Crystalline Solids 141, 76-87 (1992).

[63]. S. Brotherton, Introduction to thin film transistors: Physics and technology of TFTs (2013).

[64]. "Display Market by Product (Smartphone, Wearables, Television, Automotive, Signage), Technology (LCD, OLED (Flexible, Foldable, Rigid), Direct-View LED, Micro-LED), Panel Size (Micro, Small & Medium, Large), Industry, and Geography - Global Forecast to 2024," (2019).

[65]. "Ultra High Definition (UHD) Panel (4K) Market by Product (Television Sets, Projectors, Personal Computers, Smart-Phones) Technology (LCD, LED, OLED), Application (Home use, Industrial, Digital signage) - Opportunity Analysis and Industry Forecast, 2020-2027," (2020).

[66]. C. T. Angelis, C. A. Dimitriadis, I. Samaras, J. Brini, G. Kamarinos, V. K. Gueorguiev, and T. E. Ivanov, "Study of leakage current in n-channel and p-channel polycrystalline silicon thin-film transistors by conduction and low frequency noise measurements," Journal of Applied Physics 82, 4095-4101 (1997).

[67]. H. F. Mataré, "Carrier transport at grain boundaries in semiconductors," Journal of Applied Physics 56, 2605-2631 (1984).

[68]. V. Privitera, A. L. Magna, C. Spinella, G. Fortunato, L. Mariucci, M. Cuscuna, C. M. Camalleri, A. Magri, G. L. Rosa, B. G. Svensson, E. V. Monakhov, and F. Simon, "Integration of Melting Excimer Laser Annealing in Power MOS Technology," IEEE Transactions on Electron Devices 54, 852-860 (2007).

[69]. B. Geffroy, P. le Roy, and C. Prat, "Organic light-emitting diode (OLED) technology: materials, devices and display technologies," Polymer International 55, 572-582 (2006).

[70]. T. Tsujimura, OLED Display Fundamentals and Applications (Wiley Series in Display Technology) 2nd Edition (2017).

[71]. S. Beucher, and C. Lantuéjoul, "Use of watersheds in contour detection," International Workshop on Image Processing, Real-Time Edge and Motion Detection/Estimation, 2.1-2.12 (1979).

[72]. A. Kornilov, and I. Safonov, "An Overview of Watershed Algorithm Implementations in Open Source Libraries," Journal of Imaging 4, 123

(2018).

[73]. S. De, S. Bhattacharyya, S. Chakraborty, and P. Dutta, "Hybrid Soft Computing for Multilevel Image and Data Segmentation," (2016).

[74]. S. N, and V. S, "Image Segmentation By Using Thresholding Techniques For Medical Images," Computer Science & Engineering: An International Journal 6, 1-13 (2016).

[75]. M. Wei-Ying, and B. S. Manjunath, "EdgeFlow: a technique for boundary detection and image segmentation," IEEE Transactions on Image Processing 9, 1375-1388 (2000).

[76]. P. S. Umesh Adiga, and B. B. Chaudhuri, "Region based techniques for segmentation of volumetric histo-pathological images," Computer Methods and Programs in Biomedicine 61, 23-47 (2000).

[77]. L. Vincent, and P. Soille, "Watersheds in digital spaces: an efficient algorithm based on immersion simulations," IEEE Transactions on Pattern Analysis and Machine Intelligence 13, 583-598 (1991).

[78]. N. Al Hakkak, Data Structures and Algorithms (DSA) (2019).

[79]. E. Limpert, W. A. Stahel, and M. Abbt, "Log-normal Distributions across the Sciences: Keys and Clues: On the charms of statistics, and how mechanical models resembling gambling machines offer a link to a handy way to characterize log-normal distributions, which can provide deeper insight into variability and probability—normal or log-normal: That is the question," BioScience 51, 341-352 (2001).

[80]. R. B. Bergmann, and A. Bill, "On the origin of logarithmic-normal distributions: An analytical derivation, and its application to nucleation and growth processes," Journal of Crystal Growth 310, 3135-3138 (2008).

[81]. S. K. Kurtz, and F. M. A. Carpay, "Microstructure and normal grain

growth in metals and ceramics. Part I. Theory," Journal of Applied Physics 51, 5725-5744 (1980).

[82]. A. Bosseboeuf, J. Boulmer, and D. Débarre, "Planarization of rough silicon surfaces by laser annealing," Applied Surface Science 109-110, 473-476 (1997).

[83]. Q. S. Mei, and K. Lu, "Melting and superheating of crystalline solids: From bulk to nanocrystals," Progress in Materials Science 52, 1175-1262 (2007).

[84]. M. L. Kronberg, and F. H. Wilson, "Secondary Recrystallization in Copper," JOM 1, 501-514 (1949).

[85]. J. J. Wang, A. Limanov, Y. Wang, and J. Im, "Observation of Superheating of Si at the Si/SiO2 Interface in Pulsed-laser irradiated Si Thin Films," MRS Proceedings 1770 (2015).

[86]. J. Im, M. Chahal, P. van der Wilt, U. J. Chung, G. S. Ganot, A. M. Chitu, N. Kobayashi, K. Ohmori, and A. Limanov, "Mixed-phase solidification of thin Si films on SiO 2," Journal of Crystal Growth - J CRYST GROWTH 312, 2775-2778 (2010).

[87]. J.S. Im, R. Song, V.K. Wong, W. Pan, I. Choi, and M. Yu, "57-5: Excimer Laser Annealing and Spot-Beam Crystallization of Si Films for Advanced Displays, " SID Symposium Digest of Technical Papers **49**, 762-763 (2018).

[88]. R. Song, I. Choi, W. Pan, M. Yu, and J. S. Im, "57-4: Experimental Demonstration of Quasi-CW SBC of Si Films Using Ultra-High-Frequency UV Fiber Lasers," SID Symposium Digest of Technical Papers **49**, 759-761 (2018).

Appendix A

Spot Beam Crystallization Generated Si Thin Films

The currently used ELA technology suffers from a number of persistent difficulties which considerably affects the quality and the yield rate of the display backplane. Those include pulse-to-pulse energy variation and nonuniform spatial energy distribution across the long (1500mm) and narrow (0.4mm) excimer laser beam, which result in the so-called shot mura and line mura. Pulse-to-pulse energy variation is primarily caused by the not perfectly stable excitement and lasing of the mixed gases. Nonuniform spatial energy distribution of the shaped laser beam is mainly attributed to the intrinsic imperfection of the optical elements used to configure the laser. The line-mura and shot-mura, as shown in Figure A.1, constitute large thickness variations in macroscopic scale (tens of micrometers)[21]. Such problems eventually lead to the unstable performance of the electronic components fabricated onto the ELA films, yielding defective products.

A promising newly conceptualized LTPS method, which we call spot beam crystallization (SBC), is undergoing intensive investigation in our group [15]. Such method is motivated by the persistent issues and concerns existing in the current ELA manufacturing and the opportunity of leveraging an

emerging high-power UV fiber-laser technology. In SBC, solid-state laser and a narrow, relatively round (spot) beam are used, in contrast to the gas laser and the line-shaped beam used in the ELA. The solid-state lasers tend to be more stable and easier to control, so the pulse-to-pulse energy variation is minimized. Besides, elaborate beam shaping optics are not required, which avoids the issue of spatially nonuniform energy distribution persistent in the ELA beam. In addition, SBC has several other advantages over the ELA, such as the low cost and the smaller system dimensions. In this appendix, the SBC method and the microstructure of the generated p-Si thin film are presented, followed by the discussion of the technology and the generated microstructure.

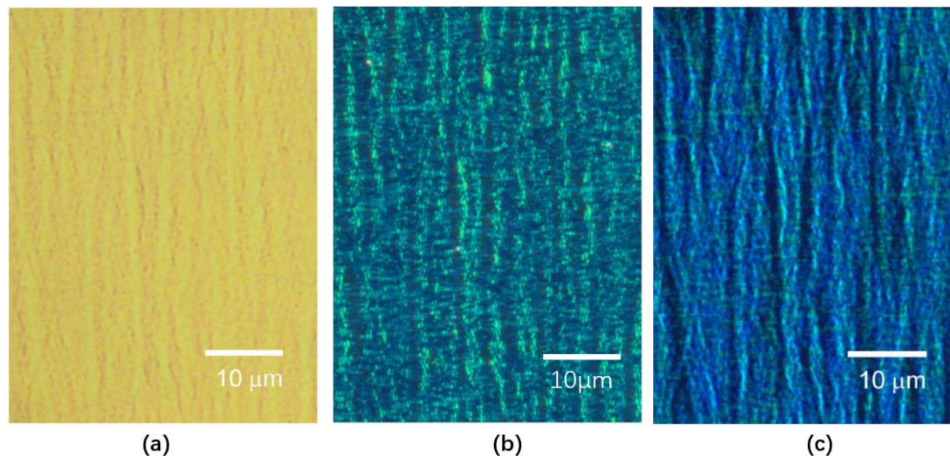

Figure A.1: (a) The bright-field optical microscope image, (b) the corresponding dark-field optical microscope image and (c) the polarized-light-microscopy optical microscope image of the surface of ELA-generated p-Si thin film. The longitudinal direction of the laser beam is in the vertical direction and the scanning direction is in the horizontal direction. The river-like patterns, where thickness normal to the page is larger than in the other areas, are the so-called mura.

A.1 Spot-Beam Crystallization Method

The SBC method accomplishes the nontrivial task of creating a crystallization-optimal thermal environment out of ultra-short (~1 ns), ultra-low energy (~1 μJ), and ultra-high-frequency (~100s of MHz) pulses in by executing sequentially overlapped irradiation via rapid scanning of a small spot beam [87]. By substantially overlapping the beam for sequential pulses during the scan, it becomes possible to use the multiple pulses to incrementally heat up and induce essentially a single "melting-and-solidification" cycle of the "small-and-confined" region over tens to hundreds of nanoseconds (the very temporal range within which optimal crystallization of Si films on glass or plastic substrates can be attained) in a continuous manner throughout the scan [87].

This method is schematically shown in Figure A.2. The laser spot raster scans over the processed area using a polygon optical system, where a fast-rotating polygon reflects the laser beam. The laser is with 355nm wavelength, 1ns pulse duration, 150MHz lasing frequency and several tens of micrometers of FWHM diameter. The scanning velocity ranges from 50m/s to 100m/s. By combining the spot diameter and the scanning velocity, the overlapped area of two sequential spots can be tuned.

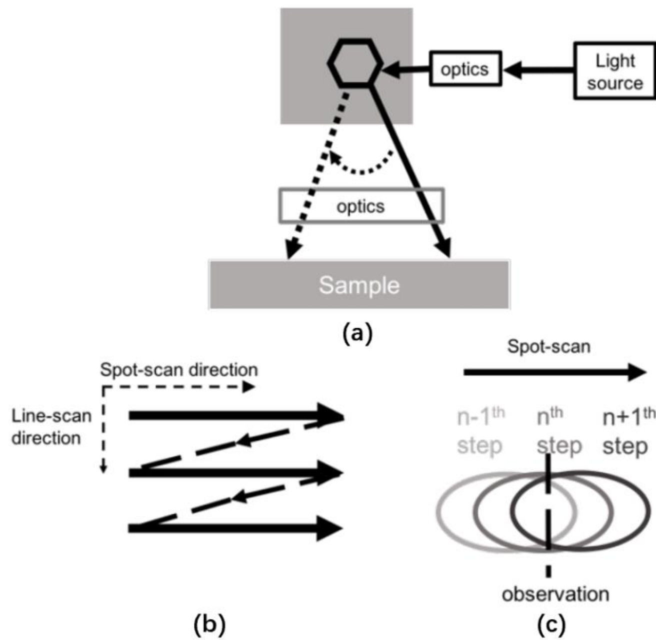

Figure A.2: Schematic diagrams respectively of (a) main SBC system components, (b) raster-scan process over a large processing area, and (c) overlap scanning of spot beam [87].

A.2 Microstructure of the SBC Si Thin Film

The precursor material is dehydrogenated PECVD a-Si thin film with the thickness of 50nm. Relatively high laser energy and lower laser energy are respectively used in the SBC process while the other parameters are kept the same. The TEM images of the microstructure generated under the two energy conditions are presented in Figure A3. Figure A3(a) is the microstructure generated using relatively lower laser energy, where the grains are ELA-like and relatively uniform. Meanwhile irregular grains which are caused by substantial melting and subsequent solidification can be identified in the microstructure generated by relatively higher laser energy, as shown in Figure A3(b). It should be noted that the ELA-like grains shown in Figure A3(a) are

much smaller than the typical ELA grains.

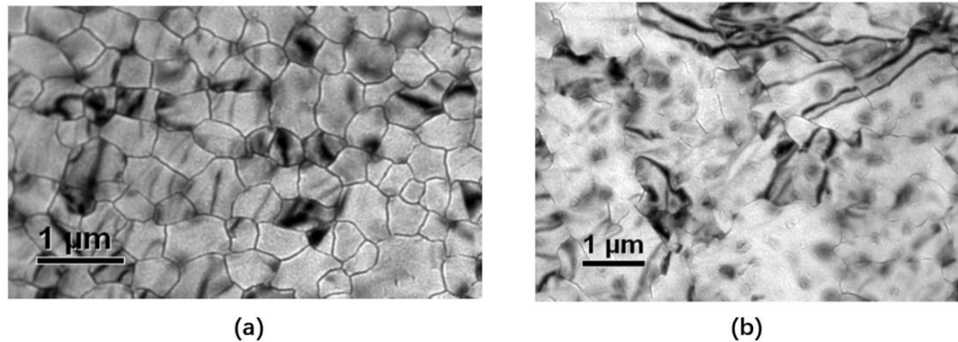

Figure A.3: Bright-field plane-view TEM images of multiple-scan SBC crystalized regions; the films were processed with the energy density (lower in (a) than (b)) below the CMT. The microstructure in (a) is alike ELA microstructure, but does not show periodicity. The local microstructure analysis of such microstructure would give different results compared to those of the ELA [87].

A.3 Discussion and Summary

The preliminary investigations, of the SBC Si thin film conducted in our group have demonstrated great potential of this method in the manufacturing of LTPS material, which would have valuable application in display industry. Even though the microstructure generated by SBC is quite alike that generated by ELA, the equipment, technological details and the mechanisms are not the same. In order to understand this technology and the generated material, we propose to utilize our developed program and the schemes adopted to analyze the microstructure of ELA films to perform systematic and comprehensive analyses of the microstructure of the SBC films. We believe that such analyses could accelerate the understanding of the SBC technique and the generated material, which would help bring this technique closer to its commercialization and provide related research fields with valuable implications.